Access to Electronic Thesis

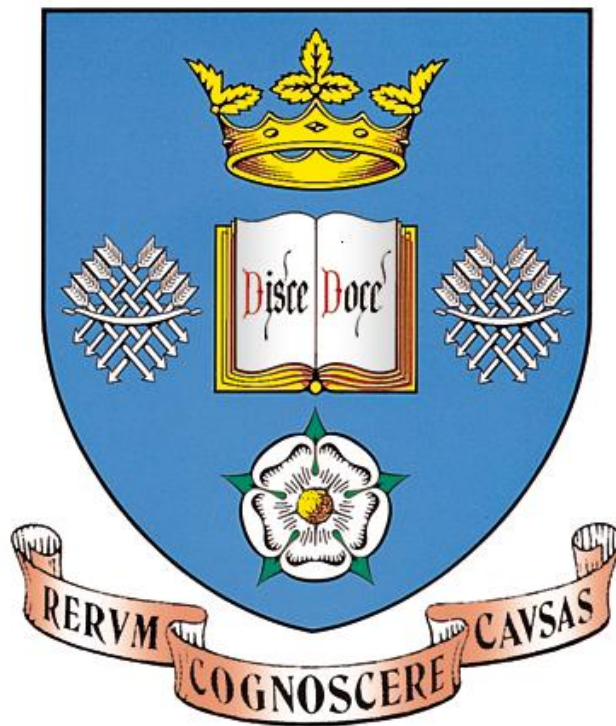|	
Author:	Mohammed Abdul Majid
Thesis title:	GaAs-Based Quantum Dot Emitters for Telecomms and Broadband Applications
Qualification:	PhD

GaAs-Based Quantum Dot Emitters for Telecomms and Broadband Applications

By

Mohammed Abdul Majid

Department of Electrical and Electronic Engineering

Thesis submitted to the University of Sheffield for the degree of Doctor of Philosophy

August 2011

Intentionally Blank

Abstract

This thesis details InAs/GaAs quantum dots (QD) as light emitting media for gallium arsenide (GaAs) based bilayer laser devices for optical communication and dot-in-well (DWELL) superluminescent devices for broadband applications.

The first three experimental chapters detail particular properties of QD bilayers, where the strain interactions between two closely stacked QD layers are engineered for the sole aim of extending the emission wavelength of QDs towards the 1550 nm of the telecom window. In view of this, the first experimental chapter compares laser devices utilising single QD layers with 5x InGaAs cap layers, 5x bilayer QDs with GaAs cap layers, in order to highlight the significantly better performance of bilayer laser devices in achieving long wavelength emission.

In the second experimental chapter, further optimization of the growth parameters of InGaAs capped sample is explored. Room-temperature ground-state lasing at 1420 nm and electroluminescence at 1515 nm are observed and discussed. Under high-bias conditions, asymmetric broadening of peaks in the laser gain spectra are observed, extending positive net modal gain from the devices to beyond 1500 nm. The origin of this broadening is discussed.

In the third experimental chapter, bilayer QD lasers operating in the excited state at wavelengths that span the O-band are demonstrated. An increase in K-factor limited modulation bandwidth from QD lasers operating in the excited state is predicted. This is due to a reduction in carrier transport and scattering times whilst maintaining high peak modal gain.

In the last experimental chapter, a comparison of growth conditions, photoluminescence measurements, atomic force microscopy measurements and device characteristics affecting 1200-1300 nm DWELL structures with a view to their optimization for broadband applications are explained.

Dedicated

To my beloved mother

&

To the memory of my late father and grand father

Acknowledgements

List of Publications

Journal

J1. **M. A. Majid**, D.T.D Childs, H. Shahid, S.Chen, K. Kennedy, R. J. Airey, R. A. Hogg, E. Clarke, P. Howe, P. Spencer and R. Murray
"Towards 1550 nm GaAs-based Lasers Using InAs/GaAs Quantum Dot Bilayers"
IEEE J. Sel. Topics Quantum Electron., vol. 17, no.5, pp. 1134-1342
(2011).

J2. **M. A. Majid**, D.T.D Childs, K. Kennedy, R. J. Airey, R. A. Hogg, E. Clarke, P. Spencer and R. Murray,
"O-band Excited State Quantum Dot Bilayer Lasers"
App. Phys. Lett., vol. 99, no. 5, pp. 051101-051101-3 (2011).

J3. **M.A. Majid**, D.T.D. Childs, H. Shahid, R. Airey, K. Kennedy, R.A. Hogg, E. Clarke, P. Spencer and R. Murray,
"1.52 μm electroluminescence from GaAs-based quantum dot bilayers"
Electron. Lett., vol. 47, no.1, pp. 44-46 (2011).

J4. **M. A. Majid**, D.T.D Childs, H. Shahid, S.Chen, K. Kennedy, R. J. Airey, R. A. Hogg, E. Clarke, P. Spencer and R. Murray
"Excited State Bilayer Quantum Dot Lasers at 1.3 μm"
Jpn. J. of Appl. Phys., vol. 50, no. 1, pp. 04DG10-04DG10-3 (2011).

J5. **M. A. Majid**, M. Hugues, D. T. D. Childs, R. A. Hogg,
"Effect of Deposition Temperature on the Opto-Electronic Properties of MBE Grown InAs QD Devices for Broadband Applications"
Accepted with revision, Jpn. J. of Appl. Phys., (2011)**.**

Conference

J6. **M. A. Majid**, D. T. D. Childs, R. Airey, K. Kennedy, R. A. Hogg, E. Clarke, P. Spencer and R. Murray,
"Strain Engineered Bilayers for Extending the Operating Wavelength of QD Lasers",
IET Optoelectron., vol. 5, no.3, pp. 100-104 (2011).

J7. **M. A. Majid**, H. Shahid, S.Chen, D. T. D. Childs, R. J. Airey, K. Kennedy, R. A. Hogg, E. Clarke, P. Spencer and R. Murray,
"Gain and absorption characteristics of bilayer quantum dot lasers beyond 1.3 μm"
Novel In-Plane Semiconductor Lasers X, Proc. SPIE, vol. 7953, pp.
795303-795303-7 (2011).

J8. **M. A. Majid**, D. T. D. Childs, R. Airey, K. Kennedy, R. A. Hogg, E. Clarke, P. Spencer and R. Murray,
"Bilayer for extending the wavelength of QD lasers"
J. Phys.: Conf. Ser., vol. 245, no. 1, p. 012083 (2010).

J9. **M. A. Majid**, D.T.D. Childs, S. Chen, H. Shahid, K. M. Groom, K. Kennedy, R. A. Hogg, E. Clarke, P. Spencer, and R. Murray,
"Gain Spectra Analysis of Bilayer Quantum Dot Lasers beyond 1.3μm"
PGC 2010, Proc. IEEE, pp.1-4 (2010).

J10. P. Spencer, J. Shi, E. Clarke, R. Murray, **M. A. Majid**, D. T.D. Childs, R. Alexander, K. Groom and R. A. Hogg,
"Dual-state lasing and the case against the phonon bottleneck",
Proc. SPIE, vol. 7616, pp. 761606-761606-11 (2010).

Poster and Conference Presentations

C1. **M. A. Majid**, D.T.D. Childs, R.J. Airey, R. A. Hogg, P. Spencer, E. Clarke and R. Murray,
 "Direct Comparison of Bilayer and Single Layer QD Lasers"
UK Semiconductors Conference, University of Sheffield July (2009).

C2. **M. A. Majid**, D.T.D. Childs, K. Kennedy, R. A. Hogg, E. Clarke, P. Spencer, and R. Murray, "Bilayers for Extending the Operating Wavelength of QD Lasers"
Semiconductor and Integrated Optoelectronics (SIOE) conference,

Cardiff University April (2010).

C3. **M. A. Majid**, D. T. D. Childs, R. Airey, K. Kennedy, R. A. Hogg, E. Clarke, P. Spencer and R. Murray,
"Bilayer for extending the wavelength of QD lasers"
QD 2010, East Midlands Conference Centre, Nottingham, UK, April

(2010)*.*

C4. **M. A. Majid**, D. T. D. Childs, R. Airey, K. Kennedy, R. A. Hogg, E. Clarke, P. Spencer, and R. Murray
"Excited State Bi-Layer Quantum Dot Lasers at 1.3 μm"
UK Semiconductors conference, University of Sheffield, July (2010).

C5. **M. A. Majid**, M. Hugues, D. T. D. Childs, K. Kennedy, R. A. Hogg
 "Optimisation of quantum dot deposition by molecular beam epitaxy for high spectral bandwidth sources for optical coherence tomography applications"
Photon 2010, University of Southampton, UK, Aug. (2010).

C6. **M. A. Majid**, D.T.D Childs, H. Shahid, S.Chen, K. Kennedy, R. J. Airey, R. A. Hogg, E. Clarke, P. Spencer and R. Murray,
"Excited State Bilayer Quantum Dot Lasers at 1.3 μm"

SSDM 2010, University of Tokyo, Japan, Sept. (2010).

C7. **M. A. Majid**, D.T.D. Childs, K. Kennedy, R. Airey, R. A. Hogg, E. Clarke, P. Spencer, and R. Murray,
"Towards 1.55 µm GaAs Based Lasers Using Quantum Dot Bilayers",
The 22nd IEEE International Semiconductor Laser Conference, Kyoto

Japan Sept. (2010).

C8. M. A. Majid, **D.T.D. Childs**, S. Chen, H. Shahid, K. M. Groom, K. Kennedy, R. A. Hogg, E. Clarke, P. Spencer, and R. Murray,
"Gain Spectra Analysis of Bilayer Quantum Dot Lasers beyond 1.3µm"
Photonics global conference, Singapore, Dec. (2010).

C9. M. A. Majid, H. Shahid, S.Chen, D. T. D. Childs, R. J. Airey, K. Kennedy, **R. A. Hogg**, E. Clarke, P. Spencer and R. Murray,
"Gain and absorption characteristics of bilayer quantum dot lasers beyond 1.3 µm"
Photonic west San Francisco, California United States, Jan. (2011).

C10. M. A. Majid, M. Hugues, D. T. D. Childs, K. Kennedy, **R. A. Hogg**,
"Molecular beam epitaxy for high spectral bandwidth quantum dot sources for optical coherence tomography applications"
Photonic west, San Francisco, California United States, Jan. (2011).

C11. **P. Spencer**, J. Shi, E. Clarke, R. Murray, M. A. Majid, D. T.D. Childs, R. Alexander, K. Groom and R. A. Hogg,
"Dual-state lasing and the case against the phonon bottleneck",
Photonic west, San Francisco, California United States, Jan. (2010).

C12. **P. Spencer**, E. Clarke, R. Murray, M.A Majid, D. Childs and R. Hogg,
"Thermal effects in QD lasers: carrier diffusion, dual-state lasing and the case against the phonon bottleneck"
UK Semiconductor conference, University of Sheffield, UK, July (2009).

C13. H. Shahid, D.T.D. Childs, **M.A. Majid**, K. Kennedy, R. Airey, R.A. Hogg, E. Clarke, P. Spencer, R. Murray
"Integrated amplifier for gain spectra measurement of bilayer quantum dot laser material"
UK Semiconductor conference, University of Sheffield, UK, July (2011).

C14. **M. A. Majid**, M. Hugues, D. T. D. Childs, R. A. Hogg
"Optimization of quantum dot molecular beam epitaxy diode for broadband applications" accepted for oral presentation in ***SSDM 2011***, Nagoya, Japan.

News Items: Featured article: "Joining the Dots, UK researchers have extended the emission wavelength of quantum dots on GaAs to 1.52 µm using a bilayer growth technique." *http://kn.theiet.org/magazine/eletters/4701/joining-the-dots.cfm*

Intentionally blank

Contents

Chapter 1

Introduction

1.1 Semiconductor Diode Laser-A Historical Review

A little over 45 years ago, Dr Robert N. Hall, was the first to demonstrate the semiconductor diode lasers [1.1], and within 30 days three other groups [1.2, 1. 3, 1.4] reported low-temperature lasing behaviour with *homojunction* semiconductor injection lasers. This was the first bulk GaAs semiconductor laser where carrier recombination in the depleted region provided the optical gain, a small refractive index change in the cladding region provided the mode guiding and cleaved facets provided the cavity with optical feedback. From this beginning the semiconductor was considered as a lasing media. The most important theoretical exploration of using the first *heterostructure* was carried by Krömer, who hypothesized that a heterojunction could possess extremely high injection efficiencies in comparison with a homojunction [1.5]. The next important step was in 1963, when Alferov *et al.* [1.6] formulated the idea of the double-heterostructure (DHS) lasers, and subsequently experimentally demonstrated room temperature lasing, with a significant reduction of threshold current [1.7]. However, it was in 1970, that the potential advantage of the DHS was recognised with the achievement of room-temperature continuous-wave (CW) operation [1.8]. The CW lasing was realized in stripe-geometry lasers formed by photolithography and mounted on copper plates covered by silver (Fig. 1.1).
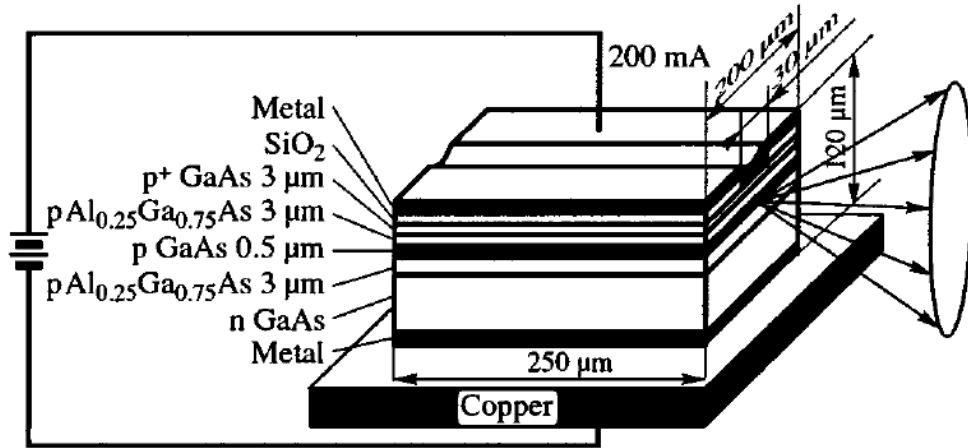
Fig. 1.1. Schematic view of the structure of the first injection DHS laser operating in the CW regime at room temperature [6].

The key element of the DHS concept is that the cladding layer surrounding the active region provides the confinement of carriers *and* optical light (mode). Based on the DHS, many advanced structures were developed such as the separate-confinement hetrostructure (SCH) [1.9] and the graded-index separate-confinement hetrostructure (GRINSCH) [1.10] where the carriers and photons are confined in separate confinement regions.

It was in 1974, that Dingle *et al.* [1.11], suggested the idea of using quantum effects in active region, which paved way to the first quantum well (QW) semiconductor laser in 1975 [1.12]. After that, QW lasers demonstrated superior performance compared to bulk semiconductor lasers [1.13, 1.14]. The lowest J_{th} of 40 A/cm^2 [1.7] was reported in 1990, which remains the lowest reported J_{th} of any QW laser. Based on the superior performance of QW lasers, it was assumed that introducing quantum dots (QDs) into the active region of a laser would result in further improvement. However, the intrinsic problem was the defect formation and

_____

inadequate carrier confinement provided by techniques such as etching [1.15] and

lithography [1.16]. The etch damage made it difficult to attain room temperature

operation resulting in quantum box lasers threshold current density reaching a

record low of 7.6 KA/cm^2 at 77 K in pulsed mode [1.17], which was very high

compared to QW lasers.

Figure 1.2 shows the evolution of semiconductor lasers in terms of threshold

current density as a function of time [1.18]. The first demonstration of QD laser

was by Kirstädter et $al.$ in 1994 [1.19] based on molecular beam epitaxy (MBE)

grown self assembled quantum dots. This work utilised, for the first time ever,

zero-dimensional quantum dots grown by lattice mismatched layers of In$_x$Ga$_y$As

based on the idea of Stranski and Krastanow (S-K) dating back to 1937. They had

observed dot islands on hetroepitaxial surfaces, although not in relation to QD

lasers. For this device excited state lasing was demonstrated at room temperature

with a J$_{th}$ of 950 A/cm^2. After this considerable progress was made, with successive

reduction of J$_{th}$ in QD lasers by several groups (Fig. 1.2). Despite the excellent J$_{th}$

values (lowest 6 A/cm^2), the predicted improvement in temperature performance

proposed by Arakawa & Sakaki, (Fig. 1.3) was not achieved. Characteristic

temperatures (T$_o$), of 50-60 K [1.20] are typical of QD lasers due to thermal carrier

escape, out of the lasing states into the excited state or completely out of the dots.

The demonstration of photoluminescence in the 1.3 μm wavelength range by

Mukai et $al.$ [1.21] showed the possibility to exploit GaAs based quantum dot

structure in optical fibre communication systems. The breakthrough towards the

_____

use of GaAs based lasers in the telecoms window was the realization of 1.3 μm QD

lasers by Huffaker *et al.* [1.22] with low threshold current density of 50 A/cm^2.

The next major step was to increase the confinement of carrier by inserting the

QDs in a QW structure known as dot-in-well. With this method a T_o of 84 K was

achieved [1.23]. Subsequently, by introducing additional QD layers (reducing the

occupation of higher dot states and decreasing the probability of carrier escape)

into the active region, a T_o of 150 K has been demonstrated [1.24]. Recently it was

suggested that the thermal excitation of holes out of the lasing state is the limiting

factor for high temperature performance and in 2002 Shchekin *et al.* [1.25] p-

doped the active layer of their QDs laser and increased the T_o to 161 K, but at the

cost of higher J_{th}.

Though QD lasers have been shown theoretically to be much better than QW lasers

in terms of; threshold current, characteristic temperature, zero wavelength

chirping, long wavelength emission, higher modulation bandwidth, narrow lasing

linewidth, this has not been easy in practice. The full promise of the QD lasers must

await advances in the understanding of material growth and optimization of laser

structure, especially in a number of critical areas such as QD growth and formation,

greater uniformity of size, high dot density (with low density of coalesced islands)

and closer dot to dot interaction range. Also, better understanding of the carrier

confinement dynamics, transport and capture times, and better evaluation of loss

mechanisms, will further improve device characteristics. Some of these aspects are

the subject of this thesis.
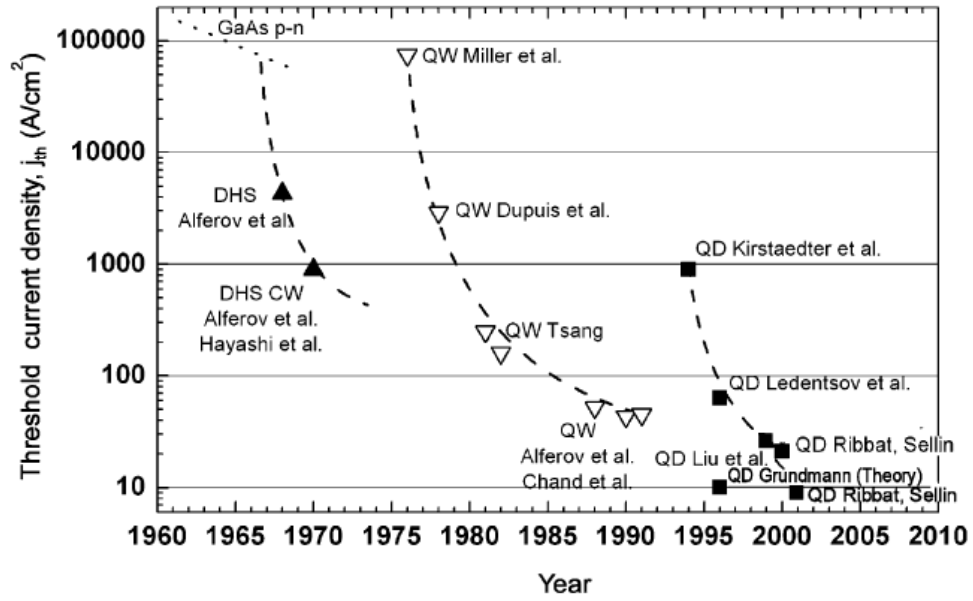
Fig. 1.2. Development of semiconductor lasers in terms of threshold current density as a function of time [18].
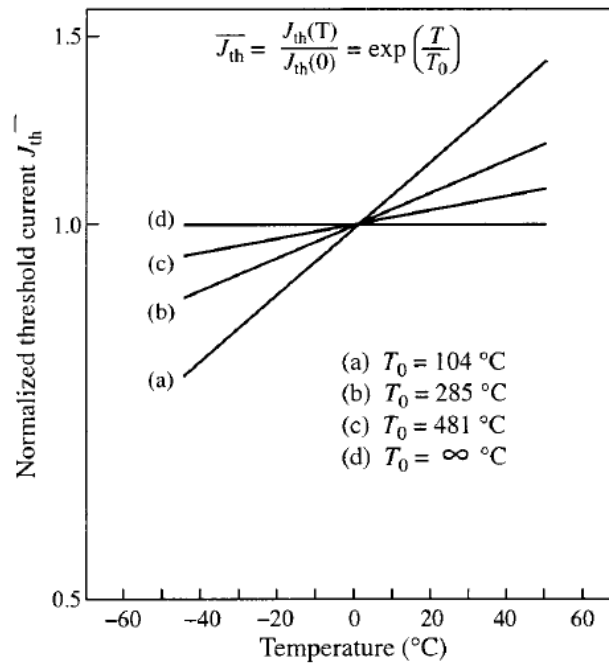
Fig. 1.3. Theoretical prediction of the threshold current versus temperature [6]. (a) Bulk, (b) with QWs (c) with QWR, (d) with QDs.

_____

1.2   Basic Laser Principles

Lasers are devices that produce monochromatic, coherent and a highly collimated beam of light. The basic operating principle of lasers were demonstrated by Charles Townes and Arthur Schawlow from Bell telephone laboratories in 1958 and the first actual laser based on a pink ruby crystal was demonstrated in 1960 by Theodor Maiman at Hughes Research Laboratories.

The three types of transition (radiation and absorption) that can occur in the semiconductor laser cavity are illustrated in Fig. 1.4. In the radiation of light there is both spontaneous emission and stimulated emission. As shown in Fig. 1.4(a), spontaneous emission is radiative process in which the electron recombines with hole at random and generates a photon (of random direction and phase). In contrast, stimulated emission (Fig. 1.4(b)) occurs when an electron-hole pair is perturbed by an incoming photon, which stimulates the electron-hole recombination and produces a new photon. The emitted light (Photon) has the same wavelength, phase and direction as the incident light (photon). In the stimulated emission one incident photon generates two photons; as a result the incident light is amplified.

The absorption is depicted in Fig. 1.4(c) is a process in which an incoming photon is absorbed by the transition of an electron in the conduction band and creation of hole in the valence band. The energy of the absorbed photon must be equal to or greater than the band gap.

_____
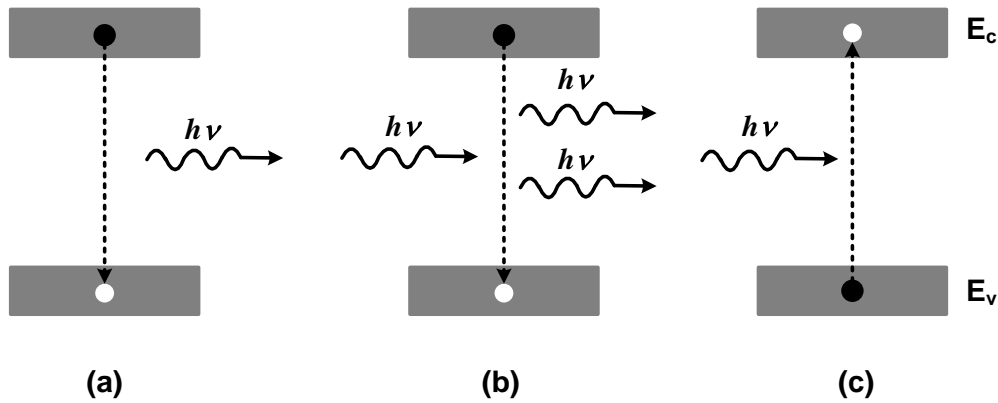
Fig. 1.4. Radiation and Absorption (a) spontaneous emission, (b) stimulated emission, and (c) absorption.

In thermal equilibrium, the population of electrons in the semiconductor laser is much greater in the lower energy state than in upper state. The probability of an incident photon contributing to the stimulated emission will be negligible and absorption is highly probable. For laser action (net optical gain) to take place a population inversion is required, to make the number of electrons in high energy states larger than the lower one and so that stimulated emission is the dominant mechanism. The population inversion necessary for laser action occurs more efficiently as the active layer material is scaled down from bulk (3-dimensional) to quantum dots (0-dimensional) as shown in Fig. 1.5. This is because the bulk semiconductor density of state (DOS), which is a measure of the maximum number of carriers that can occupy an energy range, is dependent on the square root of energy which requires large current to be injected to have a reasonable population inversion. Moving to a quantum well, quantum wire (QWR) and quantum dot, the DOS changes from stepwise to delta like state with energy leading in part to reduce

_____

the operating current. Also the zero-dimensional structure results in specific

energy released during electron-hole recombination, i.e. fixed photon energies and

fixed photon wavelengths and hence reduced emission linewidth as compared to

QW and QWR where the continuous energy bands exists. Because of the discrete

atomic like structure of QDs, the emission wavelength can be engineered which is

the major subject of this thesis.

3D
Bulk Semiconductor
$\rho(E)=E^{1/2}$

2D
Quantum Well
$\rho(E)=const(E)$

1D
Quantum wire
$\rho(E)=E^{-1/2}$

0D
Quantum dot
$\rho(E)=\delta(E)$
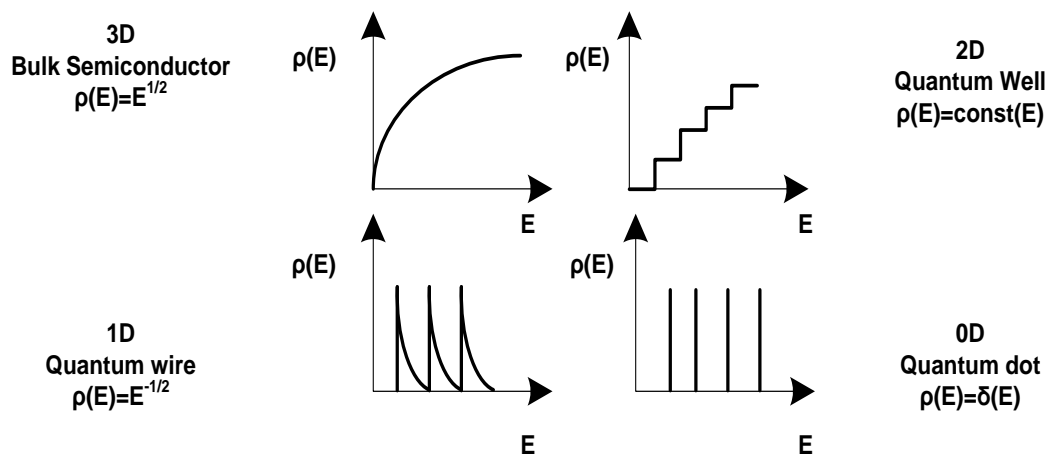
Fig. 1.5. Density of electronic states as a function of the structure size.

Figure 1.6 illustrates schematically some of the key concept in the laser operation.

Stimulated recombination of electron-hole pairs takes place within the undoped

GaAs active region. Here heterostructure provides the confinement of carriers, and

at the same time, steps in the refractive index on both sides of the active region

provides an optical waveguide to confine optical modes. Optical confinement and

feedback are required to produce regenerative feedback (reduce the loss of

stimulated photons). The stimulated photons can either stimulate other photons or

_____
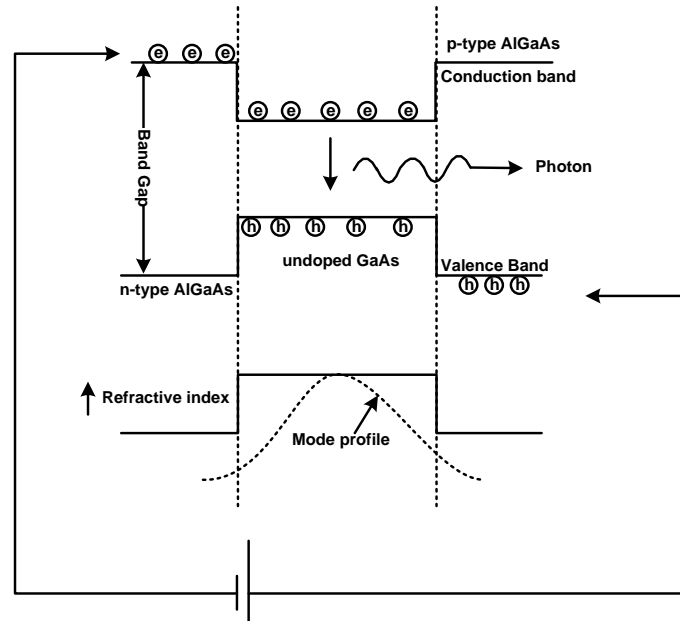
Fig. 1.6. Schematic illustration of the confinement for both the carriers and optical light in a double-heterostructure semiconductor laser.

may be lost to absorption. Figure 1.7 shows the normal optical feedback design: the fabry-perot cavity is formed by producing two parallel mirrors with reflectivities, R_1 and R_2. In a semiconductor laser this is usually formed by cleaving along the crystallographic axes. To confine the light laterally, dielectric wave guiding is used in which the optical mode is confined by total internal reflection, in which the high refractive index gain material is surrounded by slightly lower refractive index cladding layers.

For laser operation the round trip gain must be equal to the sum of the internal loss (α_i) and the mirror loss (α_m). The internal loss is the losses due to parasitic effects (absorption, scattering etc.) in the cavity and the mirror loss is the emitted light from the facets due to the non-100% reflectivity of the mirrors.

On each round trip the beam passes through the medium twice. Hence the fractional loss incurred by a light beam is

_____

$$loss = R_1 R_2 e^{-2\alpha_i L} \tag{1}$$

If the gain coefficient per unit length produced by stimulated emission is g_{th} cm^{-1}, the fractional round trip gain is given by

$$gain = e^{2 g_{th} L} \tag{2}$$

Hence

$$R_1 R_2 e^{-2\alpha_i L}.e^{2 g_{th} L} = 1 \tag{3}$$

The threshold gain per unit length may be obtained by rearranging equation 3 to get:

$$g_{th} = \alpha_i + \frac{1}{2L} \ln \left[\frac{1}{R_1 R_2} \right] \tag{4}$$

Where

$$\alpha_m = \frac{1}{2L} \ln \left[\frac{1}{R_1 R_2} \right] \tag{5}$$
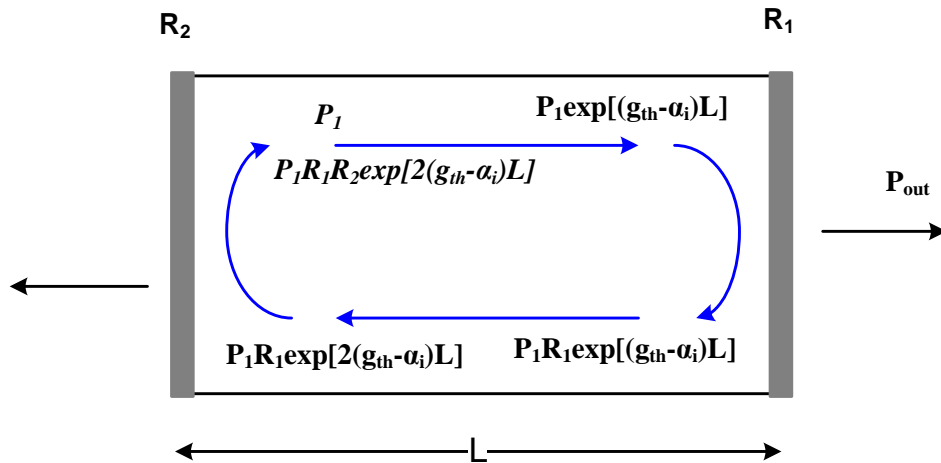
Fig. 1.7. The propagation of light in the Fabry-Perot cavity of semiconductor laser.

_____

1.3   Molecular Beam Epitaxy

There are two well established epitaxial growth techniques to produce high-purity quantum dots: molecular beam epitaxy (MBE) and metal organic vapour phase epitaxy (MOVPE). MBE growth is preferred over MOVPE for the epitaxial growth of the quantum dot (QD) structures because of the *in situ* monitoring of the growth of the QDs by reflection high energy electron diffraction (RHEED). RHEED can be used to calibrate growth rates, observe the removal of native oxide from the surface, calibrate the substrate temperature and give feedback on surface morphology. All samples studied in this thesis were grown using MBE system. The following schematic shows the main components of an MBE reactor.
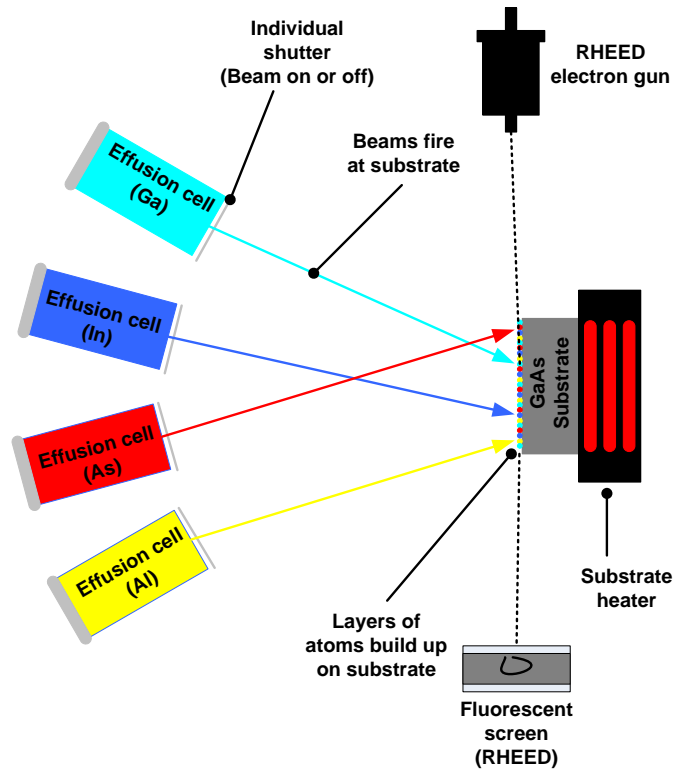
Fig. 1.8. Schematic view of MBE system for the growth of multi-element (AlGaAs, GaAs, InAs) compound films.

_____

The MBE reactor consists of an ultra high vacuum chamber with a number of effusion cells, each containing a different element (As, Al, In etc). Each cell has a computer controlled mechanical shutter in front of its opening. To grow a sample using MBE system, the cells (with individual elements) are independently heated to a temperature until the desired material starts to evaporate (gas form), producing a beam of atoms. These beams, which can be controlled on or off by mechanical shutters, are aimed at a heated, high quality substrate which could be a suitable bulk semiconductor such as gallium arsenide (GaAs), silicon (Si), germanium (Ge), or indium phosphide (InP). The incident beams that strike the substrate surface, attach to it, and as result of the high temperature of the substrate, these atoms move across the surface and build up very slowly and systematically in ultra-thin layers, atomic-layer by atomic-layer (monolayer). The substrate is rotated to ensure uniform growth of the epitaxial layers. By opening the shutter it is possible to control which semiconductor can be deposited. For example opening the shutters in front of indium (In), and arsenic (As) cells results in the growth of InAs. Shutting the indium cell and opening the gallium (Ga) cell switches to the growth of GaAs. As the shutters can be operated very rapidly in comparison to the growth rate of the material, it is possible to grow atomically flat surfaces (sharp interfaces between layers). Optimal crystal growth depends on the beam flux ratio (III/V), the substrate temperature, growth rate, and the absence of contamination (e.g. vacuum condistions).

Quantum dots (QDs) form when InAs is grown on top of the GaAs. Due to 7% lattice mismatch between InAs and GaAs, the strain energy increases with epilayer thickness and after a certain critical thickness (the first one or two monolayers are

_____

termed the "wetting layer"), induces the formation of energetically favourable

island structures called quantum dots. The precise thickness of the wetting layer

and formation of quantum dots can be monitored in real time by RHEED. The

RHEED gun emits electrons which strike the semiconductor surface at an angle of

~1-2 ^{o}C, diffracting from the surface and strike a fluorescent (phosphor) screen

forming a pattern consisting of a specular reflection and diffraction pattern, which

is indicative of the surface crystallography.

1.4   Growth technologies for long wavelength emission

Light sources for infrared telecommunications were developed using III-V

compound semiconductors based on alloys of In, Ga, As and P with modest strain

or lattice matched compositions. The need to avoid excessive build-up of strain due

to layers with different crystal lattice dimensions dictates the choice of alloy, while

retaining the emission wavelength. Edge emitting lasers based on InGaAsP/InP

cover the zero-dispersion point and absorption minimum of silica fibres in the

spectral range of 1300-1550 nm. InP based photonic integrated circuits (PICs)

achieved the highest level of integration for PICs utilizing active devices including

gain, phase, wavelength and power control. It is the unassailable commercial

technology covering the O to L (1260-1625 nm) bands of the telecom window. Next

generation devices that are capable of 500 Gb/s per chip have been undergoing

commercial trials and the research community is exploring ideas beyond 500 Gb/s

and 1 Tb/s coherent multi-channel transmitter and receiver InP PICs [1.26].

However, InP based systems have inherent problems related to small conduction

band offsets and refractive index contrast. So, the technology is expensive

_____

considering the thermoelectric cooling needed due to poor characteristic temperatures. The crystallographic quality of GaAs is better than InP and the GaAs/AlGaAs system allows distributed Bragg mirrors to be monolithically integrated into devices structures, thus allowing the development of VCSELs in GaAs/AlGaAs (not easily achievable in InP). This lack of refractive index contrast and temperature instabilities in InP has given an edge to the GaAs based technology to prosper in the area of temperature insensitive lasers, VCSELS, distributive Bragg reflectors (DBRs), semiconductor saturable absorber mirrors (SESAMs) and non-linear optical signal processing (including periodic mirrors or photonic crystal structures).

It is well known that extending the emission wavelength of InAs/GaAs QDs to the telecom wavelength of 1300 nm at room temperature is achieved by a variety of growth techniques, and the first commercial devices have recently appeared on the market (Innolume GmbH and QD Lasers Inc.). However accessing the telecom window at 1550 nm has been more difficult using InAs/GaAs self assembled QDs, yet this is highly desirable and attractive for the novel GaAs based devices described above. This difficulty is in part due to the random distribution of size, composition and the strain state of the dots, which result in inhomogeneous broadening. Therefore there has been world-wide effort to develop lasers at 1550 nm grown on GaAs.

The main aim of the research described in this thesis was to investigate materials for optical communication at wavelength around 1300 nm and towards 1550 nm based on GaAs. Several growth technologies exist for extending the emission wavelength of InAs/GaAs quantum dots and quantum wells on GaAs substrates and

_____

these are described here. A comprehensive discussion on the growth technique

that is relevant to this work, i.e to extend the emission towards 1300-1550 nm, will

be described in the experimental chapters. Currently the techniques that show

prospects for long wavelength emission include:

GaInNAs quantum well: Adding small amount of nitrogen to InGaAs is found to

decrease the band gap of the resultant alloy (GaInNAs), pushing the emission

wavelength to 1300 nm [1.27, 1.28]. Room-temperature CW lasing was first

demonstrated in a $Ga_{0.7}In_{0.3}N_{0.01}As_{0.99}$ strained QW lasers [1.29]. Current densities

are typically higher than GaAs based lasers and reports suggest that half of the

current density is lost via non-radiative recombination [1.30]. This material system

initially appeared to be a promising candidate for temperature insensitive lasers.

However, nitrogen has a low solubility in InGaAs and the material has to be

subjected to post growth annealing procedures to improve the optical quality

[1.31]. Extending the wavelength to 1550 nm is difficult and requires the

incorporation of much larger amounts of N (~3 - 5%) [1.30].

GaInNAsSb quantum well: The addition of antimony to GaInNAs material is found

to increase the quality of the interfaces and improve the photoluminescence

emission. Lasers have been demonstrated with low threshold current density (579

A/cm^2) at 1550 nm [1.30, 1.32], which show this technique to be promising and

commercially viable. In principle dilute nitride (Sb) QWs could satisfy the demand

at 1550 nm. QD devices offer some advantages over QWs: low threshold current

densities, low linewidth enhancement factors (chirp) and high characteristic

temperatures, all of which have been demonstrated. If some or all of these

_____

properties can be extended to 1550 nm then many future telecoms devices (both lasers and optical amplifiers) will be based on QDs grown on GaAs substrates.

Metamorphic buffer layers: Room temperature electroluminescence and lasing at 1515 nm has been demonstrated by growing InAs QDs on an InGaAs metamorphic buffer [1.33]. The lasers grown by this method initially shown high threshold current density on the order of KA/cm^2 [8], although recent results show low thresholds (63 A/cm^2) are possible [1.34]. However repeatability and reliability are issues for commercialisation of such structures.

Low growth rate QDs: Reducing the growth rate is found to increase the indium surface diffusion length, producing large, indium rich QDs with 1300 nm emission at room temperature [1.35-1.37]. Lasers can be fabricated with these QDs but suffer from gain saturation due to their low dot density. These types of QDs are further discussed in chapter 4 for telecom applications.

Dots-in-well (DWELL): In this method QDs are grown in a complete InGaAs QW. The benefit of this method are that in addition of an InGaAs strain reducing layer, the InGaAs layer beneath the QDs improves the QD density and reduces the diffusion of indium into the surrounding crystal during growth [1.38]. This is the only commercially viable method (Innolume GmbH and QD Lasers Inc.) at present for producing high quality 1300 nm lasers with ground state gain exceeding 45 cm^{-1} [1.39] and capable of operating in high-temperature environments that exceed 200 °C [1.40]. A systematic study of DWELL growth parameters are discussed in chapter 6, for broadband emission.

QD bilayers: QD bilayers utilize the strain between two QD layers. Rather than using individual layers, we can instead exploit the strain interactions between two

_____

closely stacked QD layers to provide additional control over the QD growth conditions. For a separation between QD layers of up to 20 nm, strain fields due to the underlying QD layer (the seed layer) will provide preferential nucleation sites for QDs in upper layers [1.41, 1.42], such that the seed layer acts as a template for growth of the second layer. Growth conditions can then be chosen to optimize the emission wavelength of the QDs in the upper layer while the QD density is determined solely by the density of the seed layer [1.35, 1.42, 1.43].

Room temperature electroluminescence at 1515 nm (Application: SESAMs, detuned laser at 1550 nm) and lasing at up to 1420 nm is observed from this technique. Under high bias conditions, asymmetric broadening of the gain peaks towards longer wavelengths is observed, which results in positive net modal gain beyond 1500 nm for a laser incorporating InGaAs capped QD bilayers. This technique is discussed in detail in chapter 3, 4 and 5. I will show that such structures are a promising approach for the realisation of GaAs based QD devices (SESAMS, Amplifiers, optical switch) in the 1550 nm region and o-band (1260-1360 nm) excited state lasers for high modulation speed.

1.5   Outline of this Thesis

Chapter 2: Device Fabrication and Experimental Methods

In this chapter experimental methods and fabrication process (broad area lasers, narrow stripe lasers and multi-section devices) which are not specifically described in individual chapters are described.

Chapter 3: Comparison of Bilayer and Single Layer QD lasers

_____

In this chapter I compare experimentally the gain characteristics of laser devices utilising a fivefold repeat of single quantum dots (QDs) layers with $In_{0.26}Ga_{0.74}As$ cap layers and a fivefold repeat of bilayer QDs with GaAs cap layers which are designed to operate at the same wavelength (~1.35 µm) and have similar QD densities (~2.4 to 2.7 $x10^{10}$ cm^{-2}). A transition of lasing from the ground state to lasing via the first excited state, and subsequently the second excited state is observed with increasing threshold gain for both the laser structures. A 50% increase in saturated modal gain is observed for the bilayer laser as compared to single layer samples. The significant result of this chapter is the extension of emission wavelength of bilayer QDs to similar wavelength as the high indium composition single layer QDs and it is the longest ever reported wavelength of single and bilayer of QDs.

Chapter 4: Towards 1550 nm GaAs-based Lasers Using InAs/GaAs Quantum Dot Bilayers

In this chapter I briefly examine the structural and optical properties that give rise to the long-wavelength emission of these closely-stacked QD systems (hereafter referred to as QD bilayers), and demonstrate edge-emitting laser structures incorporating GaAs-capped and InGaAs-capped QD bilayers. Room temperature electroluminescence at 1515 nm and lasing at up to 1420 nm is observed from these devices, and I present gain and absorption spectra obtained by characterization of multi-section devices. Under high bias conditions, asymmetric broadening of the gain peaks towards longer wavelengths is observed, which results in positive net modal gain beyond 1500 nm for a laser incorporating InGaAs-capped QD bilayers. The origin of the gain broadening is discussed.

_____

Chapter 5: O-band Excited State Quantum Dot Bilayer Lasers

In this chapter I report on the fabrication of QD bilayer (repeated briefly for the sake of completeness and convenience of understanding) materials where excited state lasing is demonstrated between 1260-1330 nm, spanning the ITU O-band. The wavelength coverage is made possible by utilizing both GaAs and InGaAs capping of the emission layer. Measurement of multi-section lasers containing these QD bilayers allows the peak modal gain of the excited state as a function of current density to be deduced as described in the chapter 4, and this is comparable to commercially available 1.3 μm QD laser samples operating in the GS. Lastly, I discuss the effect of carrier transport time on modulation bandwidth and the advantage of an excited state QD laser, using a two state model.

Chapter 6: Optimisation of Quantum Dot deposition by Molecular Beam Epitaxy for High Spectral Bandwidth Sources for Optical Coherence Tomography Applications

Here I present a comparison of the growth conditions, photoluminescence (PL) measurements, atomic force microscopy (AFM) measurements and device characteristics affecting 1200-1300 nm quantum dot-in-well structures with a view to their optimization for broadband applications. In particular the deposition temperature, amount of InAs deposited to form QDs, InAs growth rate and low-temperature (LT) GaAs spacer layer thickness is varied. A systematic PL study is carried out on these samples which allow the spontaneous efficiency to be compared. Further AFM analysis on the dots allows the measurement of the dot

_____

density and uniformity which in turn suggests conditions which will produce an

optimum gain spectrum shape.

Chapter 7: Conclusion and future work

This chapter summarises the whole of my work.

_____

References

[1.1]   R. N. Hall, G. E. Fenner, J. D. Kingsley, T. J. Soltys, and R. O. Carlson ''Coherent light emission from GaAs junctions,'' *Phy. Rev. Lett.*, vol. 9, no. 9, pp. 366–368, 1962.

[1.2]   M. I. Nathan, W. P. Dumke, G. Burns, F. H. Dill, Jr., and G. Lasher, "Stimulated emission of radiation from GaAs p-n junctions," *Appl. Phys. Lett.,* vol.1, no. 3, pp. 62–64, 1962.

[1.3]   N. Holonyak, Jr., and S. F. Bevacqua, "Coherent (visible) light emission from Ga(As$_{1-x}$P$_x$) junctions," *Appl. Phys. Lett*., vol. 1, no. 4, pp. 82–83, 1962.

[1.4]   T. M. Quist, R. H. Rediker, R. J. Keyes, W. E. Krag, B. Lax, A. L. McWhorter, and H. J. Zeiger, "Semiconductor maser of GaAs," *Appl. Phys. Lett*., vol. 1, no. 4, pp. 91–92, 1962.

[1.5]   H. Kroemer, "Theory of a wide-gap emitter for transistors," *Proc. IRE*, vol. 45, no. 11, p. 1535-1537, 1957.

[1.6]   Z. I. Alferov, "Double heterostructure lasers: early days and future perspectives," *IEEE J. Sel Topic Quantum Elect.*, vol. 6, no. 6, pp. 832-840, 2000.

[1.7]   Z. I. Alferov, V. M. Andreev, E. L. Portnoy, and M. K. Trukan, "AlAs–GaAs heterojunction injection lasers with a low room-temperature threshold," *Fiz. Tekh. Poluprovodn*., vol. 3, pp. 1328–1332, 1969. [*Sov. Phys. Semicond*., vol. 3, pp. 1107–1110, 1970].

[1.8]   Z. I. Alferov, V. M. Andreev, D. Z. Garbuzov, Y. V. Zhilyaev, E. P. Morozov, E. L. Portnoi, and V. G. Trofim, "Investigation of the influence of the AlAs–GaAs

_____

heterostructure parameters on the laser threshold current and the realization of continuous emission at the room temperature," *Fiz. Tekh. Poluprovodn.*, vol. 4, pp. 1826–1829, 1970. [*Sov. Phys. Semicond.*, vol. 4, pp. 1573–1575, 1971].

[1.9]   M. B. Panish, H. C. Casey Jr., S. Sumski, and P. W. Foy, "Reduction of threshold current density In GaAs/$Al_xGa_{1-x}As$ heterostructure lasers by separate optical and carrier confinement," *Appl. Phys. Lett.*, vol. 22, pp. 590-591, 1973.

[1.10] W. T. Tang, "A graded-index waveguide separate-confinement laser with very low threshold and a narrow Gaussian beam," *Appl. Phys. Lett.*, vol. 39, no. 2, pp. 134-137, 1981.

[1.11] R. Dingle, W. Wiegmann, and C. H. Henry, "Quantum states of confined carriers in very thin $Al_xGa_{1-x}As$-GaAs-$Al_xGa_{1-x}As$ heterostructures." *Phys. Rev. Lett.,* vol. 33, no. 14, pp. 827-830, 1974.

[1.12] J. P. van der Ziel, R. Dingle, R. C. Miller, W. Wiegmann, and W. A. Nordland Jr, "Laser oscillation from quantum states in very thin $Al_{0.2}Ga_{0.8}As$ multilayer structures," *Appl. Phys. Lett.,* vol. 26, no. 8, pp. 463-465, 1975.

[1.13] R. D. Dupuis, P. D. Dapkus, N. Holonyak Jr., E. A. Rezek, and R. Chin, "Room-temperature laser operation of quantum-well $Ga_{1-x}Al_xAs$-GaAs laser diodes grown by metalorganic chemical vapor deposition," *Appl. Phys. Lett.*, vol. 32, no.5, pp. 295-297, 1978.

[1.14] W. T. Tsang, "Extremely low threshold (AlGa)As graded-index waveguide separate-confinement heterostructure lasers grown by molecular beam epitaxy," *Appl. Phys. Lett.*, vol. 40, no.3, pp. 217-219, 1982.

_____

[1.15] P. M. Petroff, A. C. Gossard, R. A. Logan, and W. Wiegmann, "Toward quantum well wires: Fabrication and optical properties," *Appl. Phys. Lett*. vol. 41, no. 7, pp. 635-639, 1982.

[1.16] M. A. Reed, R. T. Bate, K. Bradshaw, W. M. Duncan, W. R. Frensley, J. W. Lee, and H. D. Shih, "Spatial quantization in GaAs–AlGaAs multiple quantum dots," *J. Vac. Sci. Technol. B*, vol. 4, no. 1, pp. 358-360 ,1986.

[1.17] H. Hirayama, K. Matsunaga, M. Asada, and Y. Suematsu, "Lasing action of $Ga_{0.67}In_{0.33}As$/GaInAsP/InP tensile-strained quantum-box laser," *Electron. Lett.*, vol. 30, no.2, pp. 142–143, 1994.

[1.18] M. Henini, M. Bugajski, "Advances in self-assembled semiconductor quantum dot lasers", *Microelectronics Journal*, vol. 36, no. 11, pp. 950–956, 2005.

[1.19] N. Kirstaedter, N. N. Ledentsov, M. Grundmann, D. Bimberg, V. M. Ustinov, S. S.Ruvimov, M. V. Maximov, P. S. Kop'ev, Zh. I. Alferov, U. Richter, P. Werner, U. Gosele and J. Heydenreich, "Low threshold, large To injection laser emission from (InGa)As quantum dots," *Electron. Lett.*, vol. 30, no. 17, pp. 1416-1418, 1994.

[1.20] V. M. Ustinov and A. E. Zhukov, "GaAs-based long-wavelength lasers," *Semicond. Sci. Technol*., vol. 15, no. 8, R41, 2000.

[1.21] K. Mukai , N. Ohsutka , M. Sugawara and S. Yamazaki, "Self-formed InGaAs Quantum Dots on GaAs substrates emitting at 1.3 µm ," *Jpn. J. Appl. Phys*., vol. 33, part 2, p. L1710 , 1994.

_____

[1.22] D. L. Huffaker , G. Park , Z. Zou , O. B. Shchekin and D. G. Deppe "1.3 µm

room-temperature GaAs-based quantum-dot laser," *Appl. Phys. Lett*., vol.

73, no. 18, pp. 2564-2566 ,1998.

[1.23] G. Liu, H. Li, K. Malloy, and L. F. Lester, "Extremely low room temperature

threshold current density diode lasers using InAs dots in $In_{0.15}Ga_{0.85}As$

quantum well," *Electron. Lett*., vol. 35, no. 14, pp. 1163–1164, 1999.

[1.24] A. R. Kovsh, N. A. Maleev, A. E. Zhukov et al., "InAs/InGaAs/GaAs quantum

dot lasers of 1.3 µm range with enhanced optical gain," *J. Cryst. Growth*, vol.

251, no. 1-4, pp. 729–736, 2003.

[1.25] O. B. Shchekin and D. G. Deppe, "1.3 µm InAs quantum dot laser with T_o =

161 K from 0 to 80 °C," *Appl. Phys. Lett*., vol. 80, no. 18, pp. 3277-3279, 2002.

[1.26] F. A Kish *et al.*, "Current Status of Large-Scale InP Photonic Integrated

Circuits" *IEEE J. Sel Topic Quantum Elect.*, Published online, vol. 19, p.1-20,

2011.

[1.27] N. Tansu, J. Y. Yeh, and L. J. Mawst, "High-performance 1200-nm InGaAs

and 1300-nm InGaAsN quantum-well lasers by metalorganic chemical vapor

deposition," *IEEE J. Sel Topic Quantum Elect.*, vol. 9, no. 3, pp. 1220–1227,

2003.

[1.28] R.S. Williams, W.M. McGee, M.J. Ashwin, T. S. Jones, E. Clarke, P. Stavrinou,

J. Zhang, S. tomic, C.P.A. Mulcahy, "Wavelength control across the near IR-

spectrum with GaInNAs," *Appl. Phys. Lett.*, vol. 90, no. 3, p. 032109, 2007.

_____

[1.29]   K. Nakahara, M. Kondow, T Kitatani, M. C. Larson, and K. Uomi, "1.3µm continuous-wave lasing operation in GaInNAs quantum-well lasers," *IEEE Photon. Tech. Lett.*, vol. 10, no. 4, pp. 487-488, 1998.

[1.30] S. Tomic, E. P. O'Rielly, R. Fehse, S. J. Sweeney, A. R. Adams, A. D. Andreev, S. A. Choulis, T. J. CHosea, and H. Riechert, "Theoretical and experimental analysis of 1.3µm InGaAsN/GaAs lasers," *IEEE J. Sel Topic Quantum Elect.*, vol. 9, no. 5, p. 1228-1238, 2003.

[1.31] M. Henini, "Dilute Nitride Semiconductors", Elsevier, Amsterdam, 2005.

[1.32] S. Bank, H. Bae, H. Yuen, M. Wistey, L. Goddard, and J. Harris, "Room-temperature continuous-wave 1.55µm GaInNAsSb laser on GaAs," *Electron. Lett.*, vol. 42, no. 3, pp. 156-157, 2006.

[1.33] N. N. Ledentsov, A. R. Kovsh, A. E. Zhukov, N. A. Maleev, S. S. Mikhrin, A. P. Vasil'ev, E. S. Semenova, M. V. Maximov, Y. M. Shernyakov, N. V. Kryzhanovskaya, V. M. Ustinov, and D. Bimberg, "High performance quantum dot laser on GaAs substrates operating in 1.5 µm range," *Electron. Lett.*, vol. 39, no. 15, pp. 1126-1128, 2003.

[1.34] Z. Mi, P. Bhattacharya, and J. Yang, "Growth and characteristics of ultralow threshold 1.45 µm metamorphic InAs tunnel injection quantum dot lasers on GaAs," *Appl. Phys. Lett.*, vol. 89, no. 15, p. 15310, 2006.

[1.35] E. C. Le Ru, P. Howe, T.S. Jones, and Murray, R.: "Strain-engineered InAs/GaAs quantum dots for long-wavelength emission," *Phys. Rev. B*, vol. 67, no. 16, pp. 165303-165307, 2003.

_____

[1.36] P. B. Joyce, T. J. Krzyzewski, G. R. Bell, T. S. Jones, E. C. Le Ru, and R. Murray, "Optimizing the growth of 1.3 µm InAs/GaAs quantum dots," *Phys. Rev. B*, vol. 64, no. 23, pp. 235317-235327-6, 2001.

[1.37] B. Alloing, C. Zinoni, V. Zwiller, L. H. Li, C. Monat, M. Gobet, T. Buchs, A. Fiore, E. Pelucchi, E. Kapon, "Growth and characterization of single quantum dots emitting at 1300 nm," *Appl. Phys. Lett.,* vol. 86, no. 10, pp. 101908-101910, 2005.

[1.38] H. Y. Liu, M. Hopkinson, C. N. Harrison, M.J. Steer, R. Firth, I. R. Seller, D. J. Mowbray and M. S. Skolnick, "Optimizing the growth of 1.3 µm InAs/InGaAs dots-in-a-well structure," *J. Appl. Phys.*, vol. 93, no. 5, p. 2931-2936, 2003.

[1.39] M. Ishida, Y. Tanaka, K. Takada, T. Yamamoto, H. Song, Y. Nakata, M. Yamaguchi, K. Nishi, M. Sugawara, and Y. Arakawa, "Effect of Carrier Transport on Modulation Bandwidth of 1.3 µm InAs/GaAs Self-Assembled Quantum-Dot Lasers," *in 22nd IEEE, International semiconductor laser conference*, 2010.

[1.40] http://qdlaser.com/cms/wp-content/uploads/2011/10/PRQD-Laser_High-Temp_EN__20110525.pdf

[1.41] Q. Xie, A. Madhukar, P. Chen, and N. P. Kobayashi, "Vertically self-organized InAs quantum box islands on GaAs(100)," *Phys. Rev. Lett.,* vol. 75, no. 13, pp. 2542-2545, 1995.

[1.42] P. Howe, E. C. Le. Ru, E. Clarke, B. Abbey, R. Murray, and T. S. Jones, "Competition between strain-induced and temperature-controlled nucleation of InAs/GaAs quantum dots," *J. Appl. Phys.*, vol. 95, no. 6, pp. 2998-3004, 2004.

_____

[1.43] E. Clarke, P. Howe, M. Taylor, P. Spencer, E. Harbord, R. Murray, S. Kahkhodazadeh, D. W. McComb, B. J. Stevens, and R. A. Hogg, "Persistent template effect in InAs/GaAs quantum dot bilayers", *J. Appl. Phys.*, vol. 107, no. 11, p. 113502-113502-6, 2010.

Chapter 2

Device Fabrication and Experimental Methods

2.1   Introduction

This chapter describes device fabrication and experimental techniques used for the characterization of quantum dot light emitting devices.

2.2   Test and Characterization of Laser Diode

This section outlines the basic characterization techniques for quantum dot laser diodes. The characterization of laser diode is carried out in order to assess how well the laser diode is performing with respect to the desired specification. The following is a brief description of the experimental laser characterization technique and analysis of the raw data which will lead to more meaningful interpretation of the results. In the basic setup of the power-current (L-I) measurement, the laser sits on a thermoelectric cooler (TEC), which keeps the heat sink temperature constant during the testing. The TEC is mounted such that it allows easy access to the top of the device for electrical contacts and enables easy access to the power meter or the fibre alignment rigs at the facet. The laser is operated either in pulsed or continuous-wave (CW) mode dependent on the analysis. Lab-view software was used to communicate between the instruments and record the results. Unless stated otherwise, this is the standard setup used for all succeeding measurements. The data used for the analysis is from broad area lasers fabricated from GaAs capped bilayer.

2.2.1 Power Vs Current (L-I) Characteristics.

The most important and the most basic laser characterization is the measurement of the light output power from the facet of the laser diode as a function of the drive current. Figure 2.1 shows typical L-I curve of a quantum dot laser diode. The first parameter of interest, is the threshold current (I_{th}), point 'A' on the curve, at which the laser diode begins to lase (start of stimulated emission). It may be observed that the device gives little output in the region below the threshold current which corresponds to spontaneous emission within the structure, however after threshold is reached the output power increases substantially with small increase in drive current. Threshold current depends on the geometry of the device (i.e. size and area of the device) so in comparing two lasers, threshold current density (Threshold current/Area of the device) is a more appropriate term to refer to rather than threshold current. The point 'B' shown is the kink in the graph which suggests switching of state (ground (GS) to excited (ES) state) as shown in the inset of Fig. 2.1. This phenomenon was also confirmed by the electroluminescence spectra (EL) of the device, recorded before, during, and after the kink.

Another parameter of interest is the efficiency of the laser in converting the electrical power to output light. This is determined by the slope of the L-I curve ($\Delta P/\Delta I$) above the threshold current point. If L-I analysis is carried out for several lengths of laser bars, the following parameters can be estimated: external differential quantum efficiency (η_d), internal quantum efficiency (η_i), internal loss (α_i), transparency threshold current density (J_o), and saturated modal gain (G^{sat}).
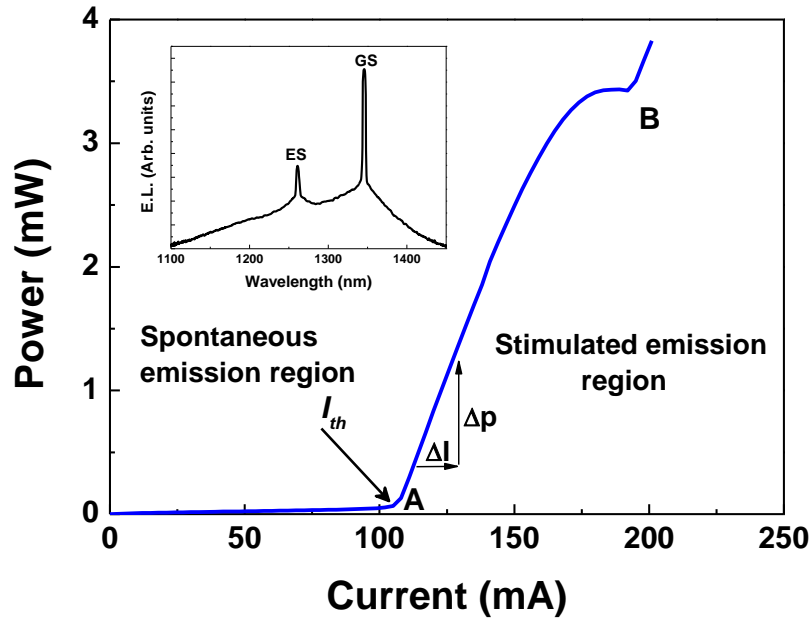
Fig. 2.1. A typical L-I characteristic (A-Lasing point, B-Switching of state). Inset spectral measurement to confirm switching of states.

2.2.2 External Differential Quantum Efficiency (η_d)

η_d is simply the ratio of the increase in output photon rate from the facet of the laser for a given increase in number of injected electrons hole pairs i.e. it gives the measure of the rate of change of optical output power with current and hence defines the slope of the L-I curve. In an ideal laser 'q' Coulombs per second of electrical current results in output power of hc/λ per second. Thus, the theoretical slope of an ideal perfect laser is (hc/λq), where h-Planck's constant, λ-photon wavelength, c-velocity of light.

To determine η_d we need to compare the slope of the L-I curve (ΔP/ΔI) to the slope (hc/λq) of the 100% efficient device. Thus the external differential quantum efficiency of the laser becomes [1]

_____

$$n_d = 2\frac{\Delta P}{\Delta I}\left[\frac{q\lambda}{hc}\right] \tag{1}$$

$\Delta P/\Delta I$ is multiplied by a factor of 2, in order to account for the output light at the

back facet that is not measured. Equivalent, perfect facets are assumed in the

above.

2.2.3 Internal Quantum Efficiency (η_i) and Internal Loss (α_i)

The efficiency of a laser in converting electron hole pairs into photons *within* the

laser diode structure, is calculated from the external differential efficiency and the

internal loss using the relationship

$$\eta_d = \eta_i \frac{\alpha_i}{\alpha_i + \alpha_m} \tag{2}$$

Where $\alpha_m=1/L$ $(ln(1/R))$ is mirror loss (R- reflectivity of the mirror)

Re-arranging equation (2), we get [2.1, 2.2]

$$\frac{1}{\eta_d} = \frac{1}{\eta_i}\left[1 + \frac{\alpha_i}{\ln(1/R)}L\right] \tag{3}$$

From equation (3) (comparing with equation of straight line *y=mx+c*), experimental

η_i is found by plotting the inverse differential quantum efficiency as a function of

cavity length with the intercept equal to 1/ η_i [1] as shown in Fig. 2.2. Internal loss

α_i is equal to the slope of the line multiplied by (η_i)*ln(1/R)*. R=0.32 for typical

GaAs/AlGaAs laser with as-cleaved facets.
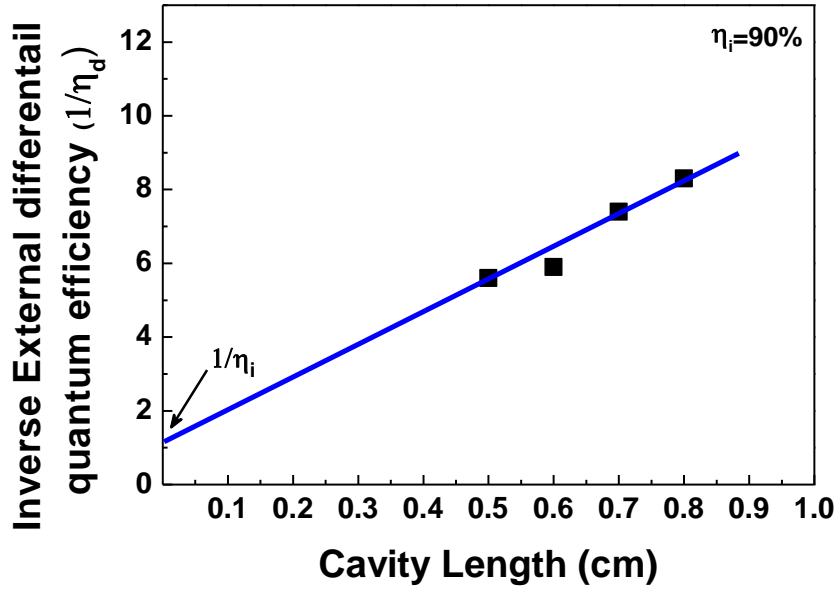
Fig. 2.2. Cavity length dependence of the inverse external differential efficiency.

2.2.4 Characteristic Temperature (T_o)

The characteristics temperature is a measure of how sensitive the threshold current is to changing temperature. If the L-I characteristics are measured as a function of temperature, (as shown in Fig. 2.3) T_o, can be extracted by plotting the natural log of the threshold current density at each temperature and is found by [2.1]

$$T_o = \frac{\Delta T}{\Delta \ln(J_{th})} \qquad (4)$$

This is the inverse of the slope of the linear fit line to the data points.

Figure 2.4 plots the natural logarithm of threshold current density as a function of temperature for a 4 mm long device. Three lines of best fit are plotted, highlighting the importance of carefully specifying the temperature over which the characteristic temperature is defined. Over the full range of 10-60 ^{o}C a moderate fit

_____

is obtained with T_o =33 ^{o}C, whilst better fits are obtained over shorter temperature

span e.g T_o =39 ^{o}C from 10-40 ^{o}C and T_o =23 ^{o}C from 45-60 ^{o}C.
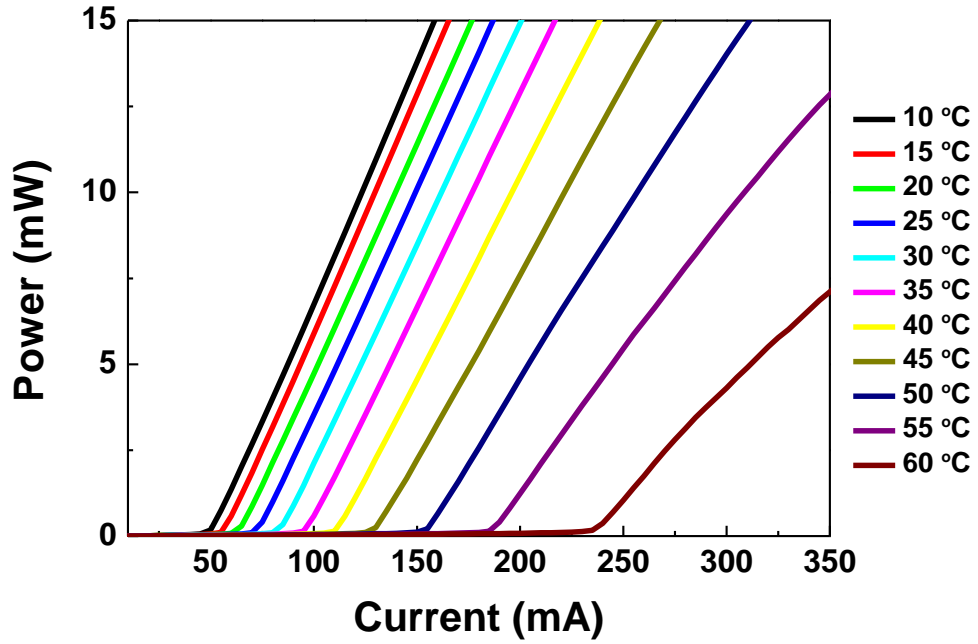
Fig. 2.3. Output light as a function of threshold current and temperature.

Figure 2.5 plots the natural logarithm of threshold current density as a function of

temperature for a 2 mm long device. Here state switching is observed at 25 ^{o}C and

two characteristics temperatures are observed one for the ground state and one

for the excited state lasing. Again care must be taken only in defining the

temperature band over which T_o is defined. But here one can see a smaller T_o for

ground state as compared to the 4 mm long sample of Fig. 2.4 indicating a strong

role of state saturation in the T_o value.

_____
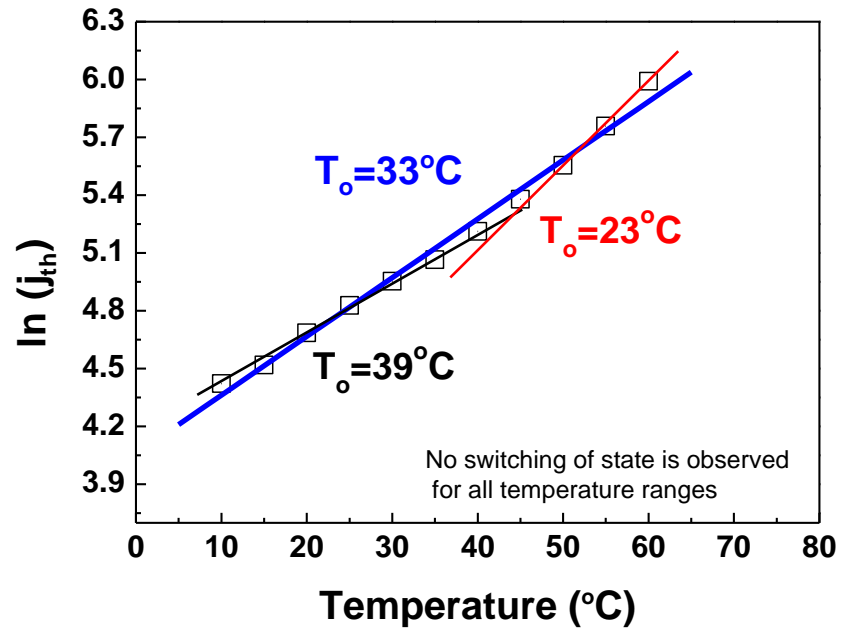
Fig. 2.4. Graph of logarithm of threshold current density as a function of temperature.
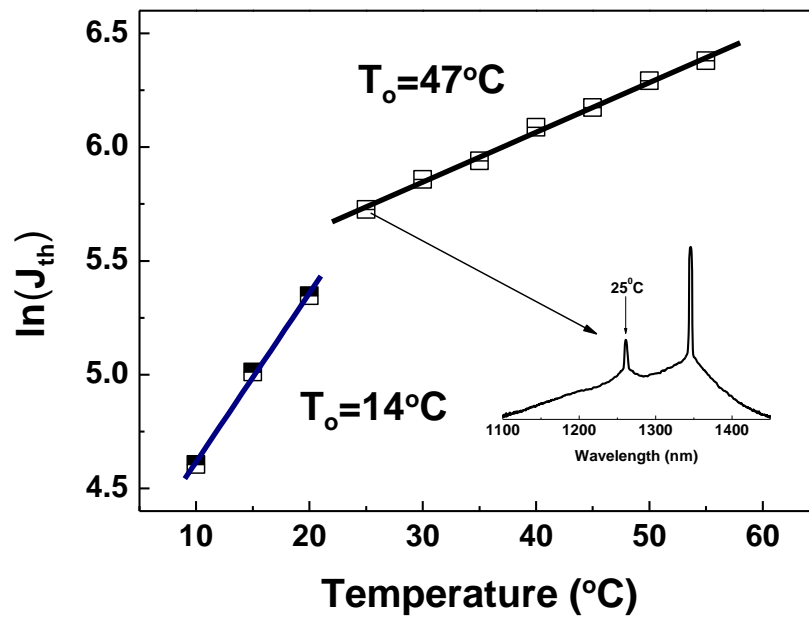
Fig. 2.5. Graph of logarithm of threshold current density as a function of temperature. The inset shows the lasing spectra at 25 ^{o}C .

_____

2.2.5 Transparency Current Density (J_o)

Another parameter that can be used to compare one set of wafers to another is the

transparency current density. The J_o is a measure of the threshold current density

of an infinitely long device, for which it can be considered that the mirror loss is

zero. This is extracted from the intercept of the linear fit to the threshold current

density versus the inverse cavity length, as shown in Fig. 2.6. J_o is influenced by the

carrier lifetime, density of states and internal loss.
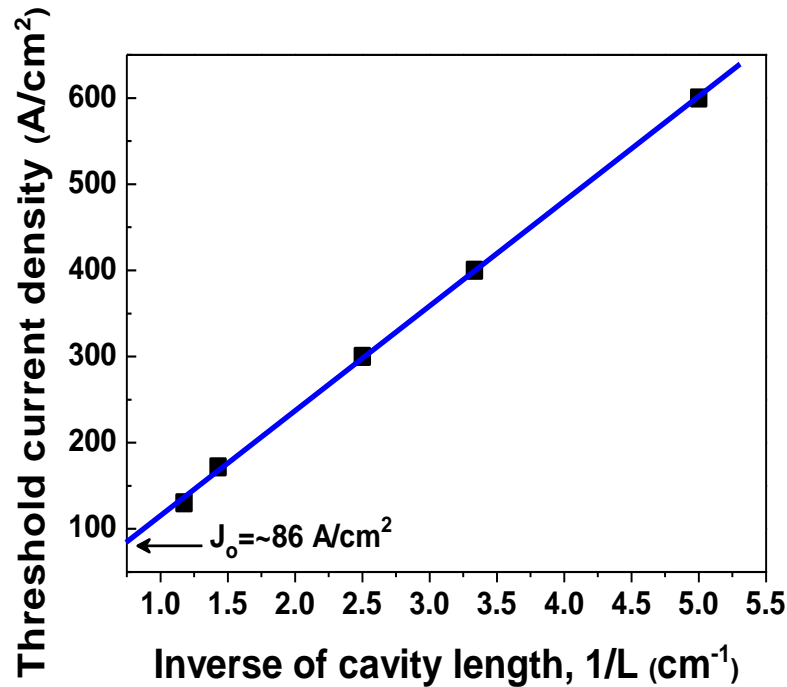
Fig. 2.6. Threshold current density, J_{th} versus the inverse cavity length, 1/L for lasers of different cavity lengths.

2.2.6 Saturated Modal Gain (G^{sat})

Saturated modal gain is the maximum gain of any state (ground, excited) of a laser

and is the sum of the internal loss and and mirror loss. G^{sat} for the ground state is

determined by taking a series of spectra of lasers of different length to determine

the shortest cavity length at which ground state lasing occurs and the longest cavity

_____

length at which excited state lasing occurs. Once each length is known, $G^{sat} = \alpha_m +$ α_i. The net modal gain-current density [2.3] curve is shown in Fig 2.7. The ground state saturated gain in this case is 6 cm^{-1} and excited state net modal gain of 15 cm^{-1}. Adding the internal loss to these gain values will give modal gain (G^{sat}) for the respective states. This will be discussed in detail in the subsequent chapters.
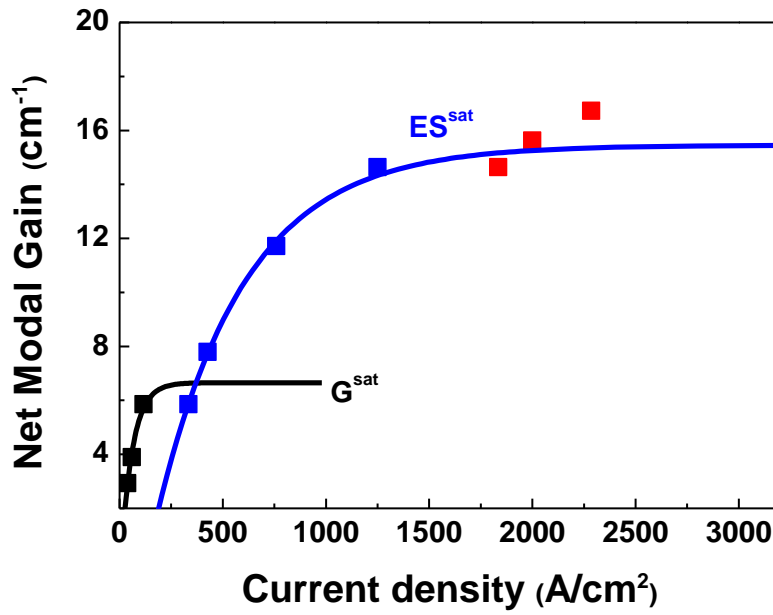
Fig. 2.7. Gain-current density curve of bilayer broad area laser.

2.2.7 Multi-section Gain and Absorption Measurements

This is a stripe length method, in which amplified spontaneous emission (ASE) is measured as a function of pumped length. This technique was first used by shanklee and Lehney using optical pumping [2.4] and it has been extended to electrical pumping by Oster *et al.*by fabrication of contact strip of different lengths [2.5]. It was Thomson *et al.* who suggested the structure in which the length variation is obtained by fabricating a single stripe segmented into multiple sections, where each section can be pumped individually [2.6].

_____

Figure 2.8 shows the schematic of the multi-section device adapted from Cardiff [2.6, 2.7] and first applied in Sheffield [2.8]. It consists of 9 mm long, 7 μm wide ridges with 1 mm long isolated contact sections. At the rear of the device is a ~1 mm long, 300 μm wide tapered absorber section with a tilted deep V-etched back facet, to suppress round trip amplification for single pass measurements. For some of the devices, the front (output) facets are either perpendicular to the cleavage plane or at 6° off to the axis of the waveguide in order to guarantee maximum power transfer [2.8]. Laser structures with and without isolated sections were fabricated to allow the characterization of both the material and fabrication process.

The segmented contact method can be employed to obtain gain and absorption spectra [2.7]. To obtain gain, the single pass amplified spontaneous emission (ASE) intensity was captured by a single mode optical fibre and measured using an optical spectrum analyzer.
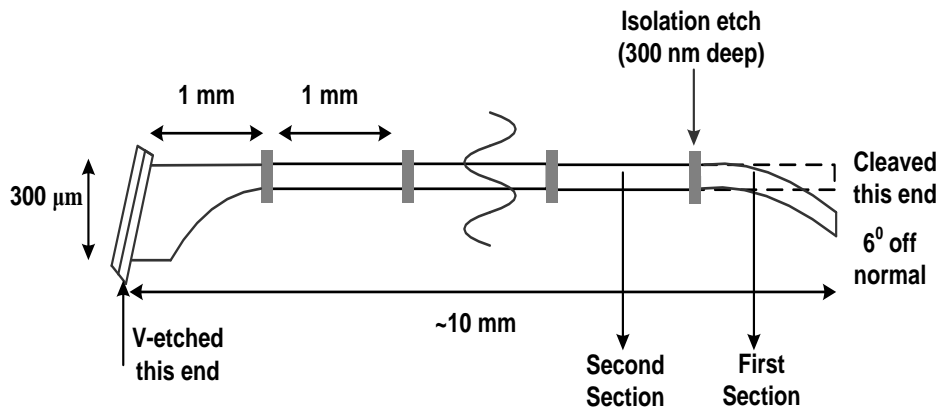
Fig. 2.8. Schematic of multi-section device design.

_____

The ASE intensity resulting from pumping the first section (see Fig. 2.8) of length L (I_L) and from pumping the first two sections of length 2L (I_{2L}) was recorded. The net modal gain, G, was obtained from:

$$G = \frac{1}{L}\left[\ln\left(\frac{I_{2L}}{I_L} - 1\right)\right]$$ (5)

Figure 2.9(a) and (b), shows the measured ASE at room-temperature for drive current ranging from 4-100 mA (per section) and Fig. 2.9(c) shows the net modal gain spectra derived from these (Fig. 2.9(a) & (b)) measurements using (5). From the gain measurement, the ground and excited state are clearly resolved, with ground state and excited state saturated gain of 4 cm^{-1} and 8 cm^{-1} at emission wavelengths of 1340 nm and 1270 nm respectively. The internal loss obtained from the long wavelength region of the gain spectra is 3±1 cm^{-1}.

The optical loss was found by measuring the ASE from pumping the first section (I_1) and then pumping only the second section (I_2) under the same current density while converting the first section ($V_{applied}$ = 0 V) into an absorber of length L. As long as the spontaneous emission from both section are equal the optical loss suffered in section 1 is given by:

$$\alpha = \frac{1}{L}\left[\ln\left(\frac{I_2}{I_1}\right)\right]$$ (6)

Figure 2.10(a) and (b) shows the ASE spectra for two sections pumped individually and Fig. 2.10(c) shows the absorption spectra obtained from these measurement using (6). The internal loss extracted from the long wavelength region is 3±1 cm^{-1}, and is in good agreement with that obtained from the gain measurement of Fig.

_____

2.9(c). It is to be noted that we have only measured gain and absorption from electrically similar sections as determind by similar current-voltage (I-V) measurements.
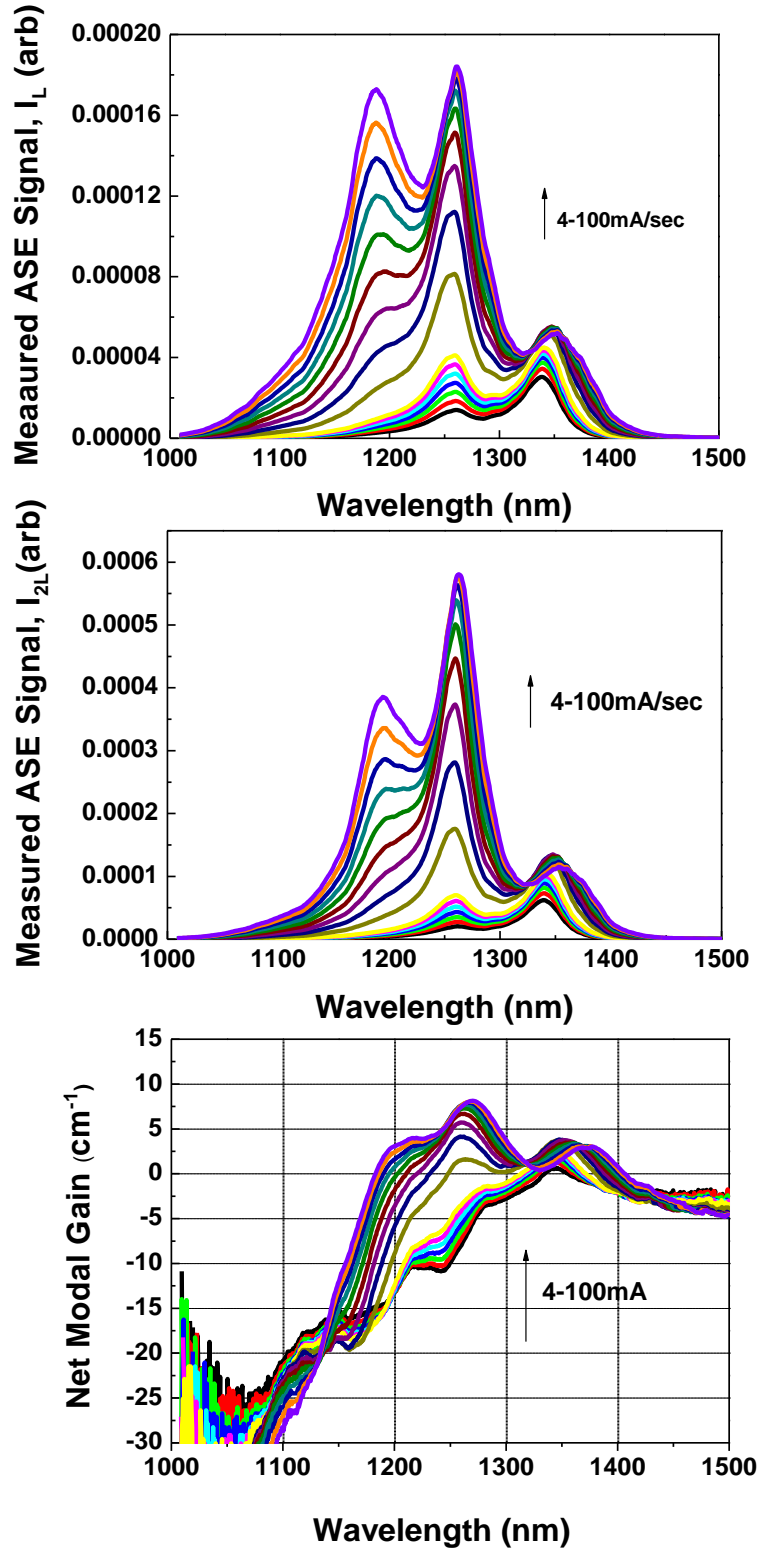
Fig. 2.9. Example of multi-section gain analysis (a) measured ASE spectra for Length L and (b) 2L, (c) net modal gain spectra derived from these measurements using (5).

_____
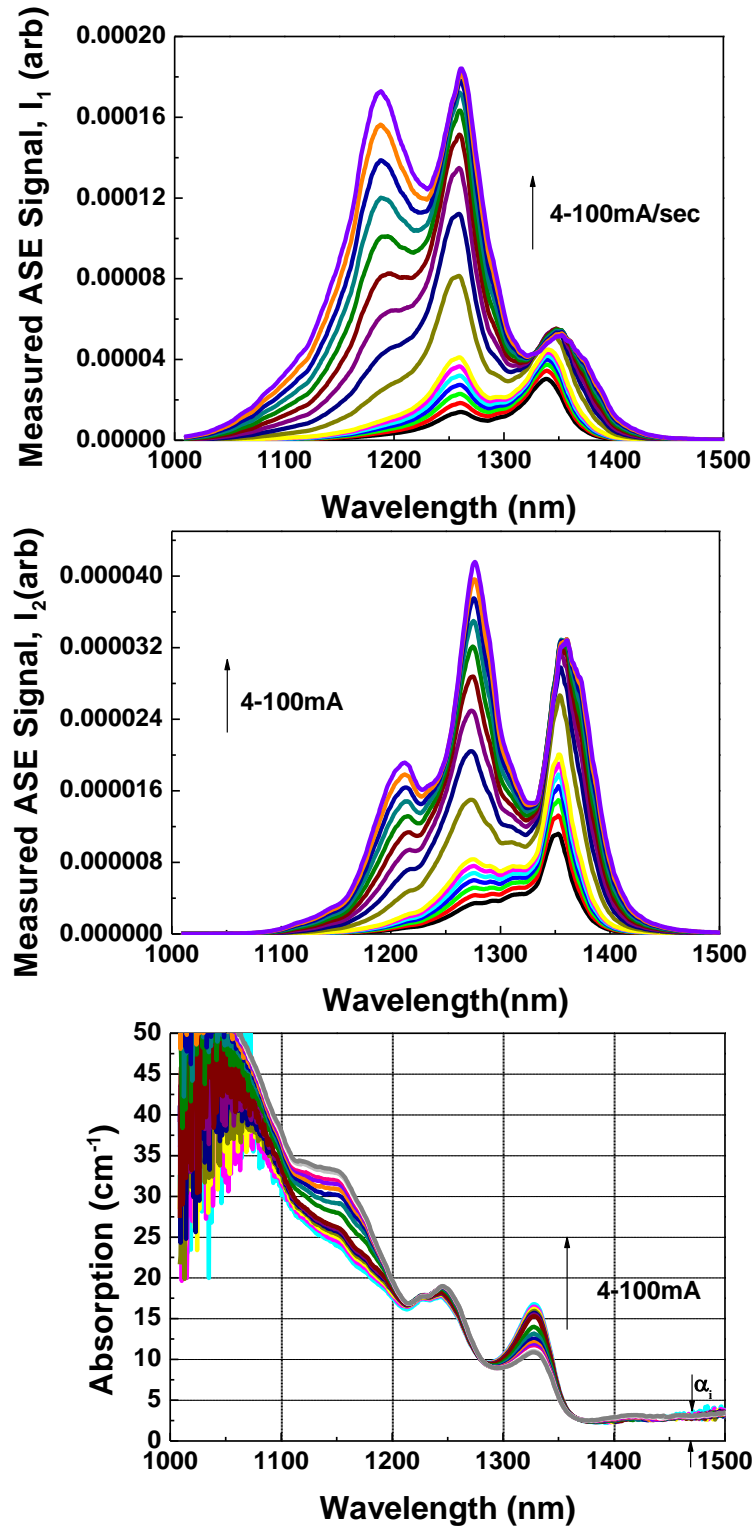
Fig. 2.10. Example multi-section absorption analysis (a) measured ASE spectra with section 1 (b) section 2 pumped independently (c) modal absorption spectra derived from these measurements using (6).

2.2.8 Dynamic Series Resistance

The series resistance usually tells a lot about the quality of the ohmic contact fabricated. High series resistance implies a low quality metal contact. Series resistance is determined by taking the derivative of the Voltage versus injection current characteristics curve of the laser diode.

2.3   Device Fabrication

This section describes the fabrication details of; broad area lasers, super luminescent diode, narrow stripe lasers, and multi-section devices used throughout this thesis.

2.3.1 Broad Area Laser Fabrication

To study the optical properties of the material broad area lasers are fabricated using an established process flow. These lasers are simpler to fabricate and the results of these devices accurately provide the device performance parameters such as threshold current, internal loss, internal quantum efficiency. After obtaining successful performance suitable set of samples may then be chosen to process as more complicated devices such as narrow ridge lasers, muti-section devices etc. The broad area superluminescent diode fabrication will not be dealt with separately as the fabrication is similar to broad area laser except the ridges are tilted by 7° to the normal of the facet.

_____

1. CLEAVE AND CLEAN

Sample cleaving:

After epitaxial growth process, the samples are very valuable and also multiple runs are required for each wafer for experimental purposes, hence the need to divide the substrate into smaller, more manageable pieces for the purpose of developing new fabrication techniques. This, together with the fact that epitaxial growth can be non-uniform towards the edges of a wafer necessitates the wafer to be cleaved into pieces of the order of 10 mm to 15 mm. Cleaving utilises the regular crystal lattice found in III / V semiconductors to produce clean straight edges. To this end, the back surface was scratched using a diamond scriber and the sample is turned and a rolling pressure is applied directly above the scribe mark on the front face surface, cleaving the sample along the line defined by the scribe marks.

Cleaning the samples:

After cleaving, the samples may have a considerable amount of particulate matter held onto the surface of the sample. This may be removed by boiling the sample for about 30 sec in isoclean grade n-butyl acetate and using a cotton bud soaked in the hot solvent, wiping the sample surface from the centre towards the edge applying firm pressure. At the end of each stroke, a new cotton bud was used and the process is repeated for the four directions around the sample. The process is repeated until a cleanliness of *< one particle per field of view on 50 X magnification* was observed. When the sample is cleaned it is boiled in acetone and in isopropyl alcohol (IPA) for about 30 sec and removed from the IPA keeping a complete film on the surface and dried thoroughly using the nitrogen gun.

_____

2.   CONTACT PHOTOLITHOGRAPHY

After cleaving and cleaning, the sample was mounted on a glass slide for ease of handling and was prepared for contact photolithography. The surface was hard baked or pre baked on 100 ^{o}C hot plate for 1 min to evaporate any water vapour or to remove solvents remaining from the preparatory cleaning steps, and a positive photoresist (BPRS-200) was then spun on the sample at a speed of 4000 rpm for 30 sec to ensure a uniform layer of photoresist. Photoresist was soft baked at 100 ^{o}C plate for 1 min to remove solvent from the resist. The sample was then placed on the stage of the mask aligner to remove the edge beads (thick photoresist beads at the edges), to do this the sample was covered with molybdenum sheets, keeping the edges open and exposed to the UV light for approximately 7 seconds (3 times of the standard exposure time). After the exposure the sample was developed in a 1:3 H_2O: developer for 1 min.

The mask set (LASTRIP 1) used for defining the stripe contact has 30, 50 and 100 µm wide stripes and some additional features for electrical measurements. Before use, the mask was thoroughly cleaned using acetone and IPA to ensure there is no photoresist on it, which may remain from the previous contact photolithography. When defining the first pattern, a cleaved edge of the sample is aligned with the mask so that the strips run along the crystal orientation. The resist is then exposed for 2.2 sec under UV light and developed for 1 min. The sample is then rinsed under deionised water (DIW) and dried using nitrogen gun. Prior to contact metallisation the sample is placed in an O_2 plasma ash for ~ 1min to remove any photoresist that may remain in the exposed/developed stripes.

_____

3.   CONTACTS METALISATION

This process is done by evaporating a thin film of metal under high vacuum conditions. After defining the pattern of the front contact on the surface of the sample, the next stage is to form an ohmic contact to the p-type GaAs using Au-Zn-Au (5 nm-10 nm-300 nm). The metals Au (30 mg) and Zn (20 mg) are first degreased by boiling in n-butyl acetate and placed in tungsten coils. The samples were ammonia washed (19:1 $H_2O:NH_3$) for 30 sec to remove any native surface oxides. The samples are then placed in to the thermal evaporator (BOC Edwards thermal evaporator) near to the crystal detector of a thickness monitoring system. The Zn and Au coil are placed at a distance of 6 cm and a vacuum of ~ 10^{-6} torr is applied. At first a thin film (5 nm) of Au is deposited before a 10 nm of Zn is deposited which improves the adhesion of Zn and finally ~300 nm of Au is deposited. This process is that when the desired vacuum is achieved, a current is passed through the filament which causes it to heat up and the metal to vaporise, which in turn is deposited all over the vacuum chamber, including the sample. The thickness is measured using the crystal monitor to within ±5 nm. After evaporation the samples are allowed to cool down for 10 minutes and placed in acetone for a process known as lift-off. The lift-off dissolves the photoresist underneath the metal lifting off the unwanted metal, leaving well defined metal contact on ridges. The samples are then cleaned using three-step cleaning process and annealed in rapid thermal annealer at 360 ^{o}C for 1 min. The annealing helps to drive Zn into upper layer and reduce the metal/semiconductor height (Schottky barrier), thus reducing the voltage drop across the contacts.

4.   RIDGEs PHOTOLITHOGRAPHY

Ridge photolithography is done to define the 'mesa' pattern, which, after etching, provides isolation of the contacts from one another. The mask named LASTRIP 2, is used for this photolithography. BPRS 100 is spun and baked. The edge beads are removed as before. Now, the second mask layer is aligned to alignment marks defined in the first stage lithography and exposed to UV light for 1.5 sec and developed for 1 min. The lithography is followed with 2 min O_2 plasma ash and 1 min hard bake prior to wet etching (ridge etch).

5   SEMICONDUCTOR ETCH

For our purposes, the etchant commonly termed 1:1:1 is used. In this etchant one part (~6 ml) hydrobromic acid, one part acetic acid and one part potassium dichromate (HBr: CH_3COOH:$K_2Cr_2O_7$) is used.   The etch rate of this solution is approximately 4 microns/min and etching is isotropic. The patterned sample is submerged into the solution, agitated gently and uniformly for 30 seconds and the etch depth is measured under the surface profiler (Dektak). The process of etch and measurement is repeated until the required etch depth is achieved. An etch depth of 1.9 μm is achieved with ±100 nm precision, removing just the top of the p-doped GaAs and AlGaAs cladding layer. In order to get good controllability of the etch depth 50% potassium dichromate and 50% deionised water was mixed with HBr and CH_3COOH solution.

6.   BACKSIDE THINNING

The samples are thinned so that it can be cleaved properly and also it aid in heat sinking. For this purpose, two layers of BPRS 200 (any thick photresist) are spun in

_____

order to prevent any damage to the samples while mounting and demounting. Then the samples are hard baked on 100 ^{o}C plate for 2 min and a glass block is placed on the hot plate (100 ^{o}C) for approximately 10 min. The samples are then mounted on the top of the glass block with uniform wax of thickness approximately (20-30 μm) on the surface. The thicknesses of the samples were measured taking account of the wax thickness. The glass block is mounted on the lapping jig (Logitech-LP50) and the samples were thinned in the range of 150-180 μm. After thinning the samples were cleaned with DIW and was demounted keeping the glass block in a beaker of n-butyl acetate. The samples are then cleaned properly using the three-step cleaning process and is ready for the evaporation of the back metal contact.

7.　　BACKCONTACT METAL

Before evaporation of an InGe-Au contact, the samples were rinsed with 19:1 ammonium solution for 30 seconds, in order to remove any oxide formed on the semiconductor surface as a result of the contact with the atmosphere oxygen. After that samples are placed in evaporator and 20 nm of InGe is deposited followed with 300 nm of gold. The samples were then annealed at 340 ^{o}C.

8.　　SCRIBE AND BREAK

The samples were then cleaved into various the lengths such as 5, 4, 3, 2, 1 and 0.5 mm, as the characterization of the lasers involves length dependent measurement.

9.　　MOUNTING AND BOUNDING

The samples were mounted on ceramic tiles with eutectic InPbAg. Usually the broad area lasers are probed directly as the ridges are broad , however CW

_____

characterization sometimes leaves localized heating around the probe tip as a consequence of the localized high carrier density there. To avoid this, devices was wire bonded so that the injected carriers are spread over the length of the device and equally pump the ridge along its length. For wire bonding the temperature of the work holder is set to 90 ^oC and the gold wire is used to connect the ridge to the gold lead of the ceramic tile. Approximately 1 wire is ball-bonded for every 0.5 mm length of the ridge.

2.3.2 Narrow Stripe Laser Fabrication

The fabrication process of narrow stripe lasers is described in the following paragraphs. The fabrication processes which are in addition of the broad area will be covered in detail.

1.   CLEAVE AND CLEAN

Refer section: 2.3.1

2.   DEFINING THE P-TYPE CONTACT

After cleaning, the sample is ready for contact photolithography. The sample is soft bake and BPRS-200 photoresist is spun, followed by 1 min hard bake at 100 ^oC. The mask with 5 and 15 µm wide features are used to define the stripe contact. The sample is exposed for 3.5 sec and developed for 1 min. The sample is ammonia washed for 30 sec before evaporating metals for ohmic contact to the p-type GaAs Au-Zn-Au (5nm-10nm-200nm). After evaporation, lift off is followed by 3 stage cleaning and thermal annealing at 360 ^oC.

_____

3. ETCHING THE RIDGE

In this step the sample is patterned again to define the etching region around the ridge. Inductively coupled plasma (ICP) technique is used to etch the ridges as wet chemical etching described earlier can not accurately transfer the mask pattern to semiconductor for small features and cannot also produce a uniform ridge profile if etched deep. The sample is loaded in the ICP etcher and is etched to the depth of 1.94 μm, just 100 nm through the active region.

4. DEPOSITION OF DIELECTRIC (SILICON NITRIDE) ISOLATION LAYER

The ridge width for standard mask set range from 5-20 μm, and direct bonding to the ridges is difficult. So, a dielectric layer is used to isolate the stripe from the other ridges, allowing for deposition of large bond pads without problem due to short circuits. 500 nm of silicon nitride (Si_3N_4) is deposited on the sample using the STDSIN recipe, via plasma enhanced chemical vapour deposition (PECVD). The total process takes about 1 hour and good step coverage is obtained. Photolithographic process is carried out for the third time to open a window in the dielectric layer on the top of the ridge with plasma assisted etching to allow bond pads to contact the ridge. The wafer is etched by reactive ion etching (RIE) system. The RIE system is basically cylindrical chamber; in which vacuum is created and the gas flow rates are set. The gases used are CHF_3 and O_2 and the flow rate is set to 35 Sccm and 5 Sccm. The RF power is the important parameter for etch rate in the RIE process, setting optimum value is crucial. The RF system is typically set at 60 W and then the sample is etched ~12 min until Si_3N_4. Monitoring the previous etching results of the system provides suitable calibration to allow an etch time to be selected. After

_____

etching the sample is checked under a microscope to ensure that the dielectric is completely removed from the ridges. The regions with dielectric remaining have a clear greenish colour. The etch is followed with 5 min O_2 plasma ash and 3 stage cleaning.

5. BOND PADS PHOTOLITHOGRAPHY AND METAL DEPSOITION

Ridge laser now isolated from other devices, photolithographic step is carried out for bond pad formation. The same BPRS-200 photo-resist is used. The exposure time used is 2.5 times the normal exposure time, to make sure the resist is exposed at the bottom of the ridges. The photolithography is followed with 1.5 min O_2 plasma ash and prepared for the deposition of the top bond pads. The bond pad consists of a Ti-Au layer. The thermal evaporation of Ti-Au (15nm-150nm) bond pads, is little tricky in the sense that half of each thickness evaporated from either side of the ridge to make the metal deposition up the side–wall of the ridge even.

6. PHOTOLITHOHRAPHY FOR ELECTROPLATING AND SELECTIVE ELECTROPLATING

The same photolithography steps are carried out for electroplating the gold bond-pads. For electroplating, a rough exposure area is calculated, to determine the drive current through the electrodes. A 2 μm gold layer is deposited on the semiconductor surface with good step coverage.

7. THINNING AND BACK METAL CONTACT

The samples are thinned and back contact was applied as explained in section 2.3.1.

_____

8.   SCRIBE AND BREAK

The samples are typically cleaved into lengths of 4, 3, 2, 1 and 0.5 mm. As the ridges are narrow they are mounted on the ceramic tiles and bonded to the bondpads.

2.3.3 Multi-section SLED Fabrication

The multi-section SLEDs fabrication process is similar to narrow ridge lasers.

The steps in the fabrication of the multi-section devices are similar to fabrication of the narrow ridge lasers described in details (sec: 2.3.2).The multi-section devices are fabricated using vacuum photolithography. After cleave and clean the sample is processed for trenches photolithography followed by ICP trenches etch, to the depth of 2 µm, (just through the active region) via double trench, using silicon tetrachloride ($Sicl_4$).   The 1mm isolation section (see Fig. 2.8) was electrically isolated by means of shallow etches of p+ contact layer providing a resistance of ~2 kΩ between adjacent contacts. The size of the gap between isolation sections is ~50 µm. Au-Zn-Au was evaporated for top contact followed by electroplated bonds. The samples are then thinned and back metal contact is applied as before. The devices are probed directly with multi-probe as shown in Fig. 2.8.

_____

References

[2.1]   K. S Mobrahan,: "Test and Characterization of Laser Diodes: Determination of Principal Parameters", *Application Note*, Newport, CVR2, 1999.

[2.2]   L. V. Asryan, "Limitations on standard procedure of determining internal loss and efficiency in quantum dot lasers," *J. Appl. Phys*. vol. 99, no.1, pp. 013102 - 013102-4, 2006.

[2.3]   A. E. Zhukov, A. R. Kovsh, V. M. Ustinov, A. Yu. Egorov, N. N. Ledentsov, A. F. Tsatsul'nikov, M. V. Maximov, Yu. M. Shernyakov, V. I. Kopchatov, A. V. Lunev, P. S. Kop'ev, D. Bimberg, and Zh. I. Alferov, "Gain characteristics of quantum dot injection lasers," *Semicond. Sci. Technol*., vol. 14, no. 1, pp. 118-123, 1999.

[2.4]   K. L. Shaklee and R. F. Leheney, "Direct Determination of Optical Gain in Semiconductor Crystals," *Appl. Phys. Lett.,* vol. 46, no. 11, pp. 475–477, 1971.

[2.5]   A. Oster, G. Erbert, H. Wenzel, "Gain spectra measurements by a variable stripe length method with current injection," *Electron. Lett.*, vol. 33, no. 10, pp. 864-866, 1997.

[2.6]   J. D. Thomson, H. D. Summers, P. J. Hulyer, P. M. Smowton, and P. Blood, "Determination of single-pass optical gain and internal loss using a multisection device," *App. Phy. Lett.,* vol. 75, no. 17, pp. 2527-2529, 1999.

[2.7]   P. Blood, G. M. Lewis, P. M. Smowton, H. Summers, J. Thomson, and J. Lutti, "Characterization of semiconductor laser gain media by the segmented contact method," *IEEE J. Sel. Topics Quantum Electron*., vol. 9, no. 5, pp. 1275–1282, 2003.

_____

[2.8]   P. D. L. Greenwood, D. T. D. Childs, K. M. Groom, B.J. Stevens, M. Hopkinson

and R. A. Hogg, "Tuning superluminescent diode characteristics for optical

coherence tomography systems by utilising a multi-contact device

Incorporating wavelength modulated quantum dots," *IEEE J. Sel. Topics

Quantum Electron.*, vol.15, no. 3, pp. 757-763, 2009.

Chapter 3

Comparison of Bilayer and Single Layer QD Lasers

3.1   Introduction

The InAs/GaAs QD system has received strong interest due to the evidence of zero dimensional behaviour at room temperature and above [3.1].   Whilst typical emission wavelengths are found in the 1000-1300 nm range, longer wavelength QD lasers on GaAs are of interest for datacoms and telecoms applications.   Many of the attributes of the quantum dot (such as zero and tunable chirp, broad-band emission, temperature insensitivity, saturable absorption, single photon emission) are particularly attractive at the fibre optic transmission wavelengths of ~1310 and ~1550 nm. However, emission beyond 1300 nm is difficult to achieve, when using independent single layers of InAs/GaAs QDs [3.2]. The use of bilayers of QDs has been demonstrated as a promising route to obtaining long wavelength emission and lasing [3.3, 3.4]. In the bilayer structure, each of the two QD layers is grown at a different temperature, with strain interaction from the smaller QDs in the seed layer (first layer) fixing the QD density in the larger QDs of the second layer [3.3, 3.4]. Details discussion on dot density decoupling and wavelength optimisation is explained in next chapter. In this chapter I compare experimentally the gain characteristics of laser devices utilising a fivefold repeat of single QD layers with $In_{0.26}Ga_{0.74}As$ cap layers and a fivefold repeat of bilayer QDs with GaAs cap layers

_____

which are designed to operate at the same wavelength (~ 1340-1360 nm) and have similar QD densities (~2.4 to 2.7 x10^{10} cm^{-2}).

3.2 Experiment

The laser structures described here are shown schematically in Fig. 3.1. Growth was carried out on n$^+$ GaAs (100) substrates by molecular-beam epitaxy (MBE) by Dr Edmund Clarke. The active region for both structures was located in a 500 nm undoped GaAs layer sandwiched between 1500 nm Al$_{0.33}$Ga$_{0.67}$As cladding layers. A 400 nm p-type GaAs:Be contact layer was grown to complete the laser structure. The active region of the standard structure consists of five independent QD layers which we refer to as a single layer structure. Before each QD layer was grown, the surface was annealed under an As$_2$ flux at 580 ^{o}C for 10 minutes to smooth the growth surface [3.5]. The QD layer was then subsequently grown at 485 ^{o}C by the deposition of 2.4 ML of InAs at a growth rate of 0.014 MLs^{-1}, giving a QD density of 2.4 x 10^{10} cm^{-2} as measured by AFM on test structures. The QDs were capped by 4 nm of In$_{0.26}$Ga$_{0.74}$As then 11 nm of GaAs, also grown at 485 ^{o}C to reduce indium segregation. After this the growth temperature was ramped during the next 45 nm of GaAs deposition to the optimum GaAs growth temperature of 580 ^{o}C [3.6]. The same sequence was repeated for the rest of the active region and the remainder of the structure (e.g. p-AlGaAs cladding and GaAs contact layer) was grown at 580 ^{o}C to reduce In-Ga inter-diffusion.

 The second sample had a nominally identical waveguide structure, differing only by the replacement of the five single QD layers with 5 QD bilayers. This sample is referred as the "bilayer QD" sample in the following. Each bilayer consists of a seed

layer of QDs and an emission layer. As before, the GaAs surface was annealed at 580 ^{o}C for 10 minutes thereafter the seed layer was grown at a temperature of 480 ^{o}C by the deposition of 2.4 ML of InAs at a growth rate of 0.014 MLs^{-1}, giving a QD density of 2.**7** x 10^{10} cm^{-2} (slightly higher than for the single layer structure due to the lower growth temperature).
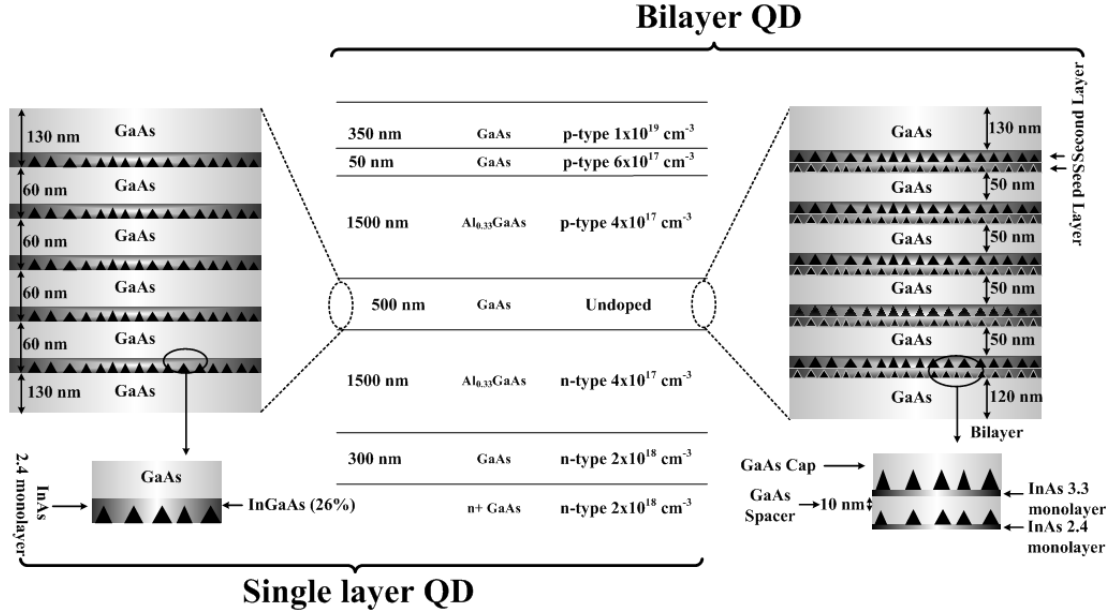
Fig. 3.1. Schematic diagram of single (left) and bilayer (right) QD laser structures.

These seed QDs were capped by 10 nm of GaAs spacer layer, also grown at 480 ^{o}C, before the temperature was raised again to 580 ^{o}C for 10 minutes to smooth the growth surface and desorb excess segregated indium. The emission layer was then grown at a reduced temperature of 467 ^{o}C by the deposition of 3.3 ML InAs at the same growth rate as for the seed layer. These QDs were then capped with 15 nm of GaAs also at 467 ^{o}C, after which the temperature was ramped to 580 ^{o}C for subsequent GaAs growth. The same sequence was repeated for the rest of the active region with the rest of the structure grown at 580 ^{o}C.

_____

The wafers were processed into broad area lasers by etching through the p-side

AlGaAs cladding layers, stopping just above the active region. Au Zn Au and In Ge

Au provided the p- and n-side ohmic contacts, respectively.   Laser bars were

cleaved into several lengths before being bonded on ceramic tiles using eutectic

InAgPb. The device facets were as-cleaved and characteristics were measured in a

pulsed regime (5 μs pulsed duration, 1 % duty cycle) to avoid thermal effects. All

measurements were performed at a tile temperature of 300 K with quoted powers

being from one facet. Direct contact to the laser was made using a 500 μm pitch

multi-contact probe to eliminate problems in inhomogeneous pumping.

3.3   Results and Discussion

Figure 3.2 shows the light-current characteristics of the single layer QD sample for

cavity lengths of (a) 8.5 mm, (b) 3 mm, (c) 1.25 mm. The inset shows the emission

spectrum for each device at 1.2 J_{th}. For the device with an 8.5 mm long cavity, Fig.

3.2 (a), lasing is observed at 1360 nm with a threshold current density of ~205 Acm^{-2}, and slope efficiency (from one facet) of 0.03 WA^{-1}. The emission at 1360 nm

corresponds to the GS of the QD ensemble, as measured by photoluminescence of

the unprocessed wafer (see Fig. 3.2(d)) and the electro-luminescence from short

cavity devices.   For the device with 3 mm cavity length (Fig. 3.2(b)) lasing is

observed at 1275 nm with a threshold current density is ~615 Acm^{-2} and the slope

efficiency is 0.08 WA^{-1}. The emission at 1275 nm is attributed to the first excited

state (ES1) of the QD ensemble. For the device with 1.25 mm cavity length, (Fig.

3.2(c)) lasing at 1185 nm is observed with a threshold current density of ~3500

Acm^{-2}, and slope efficiency of 0.06 WA^{-1}. The emission at 1185 nm is attributed to
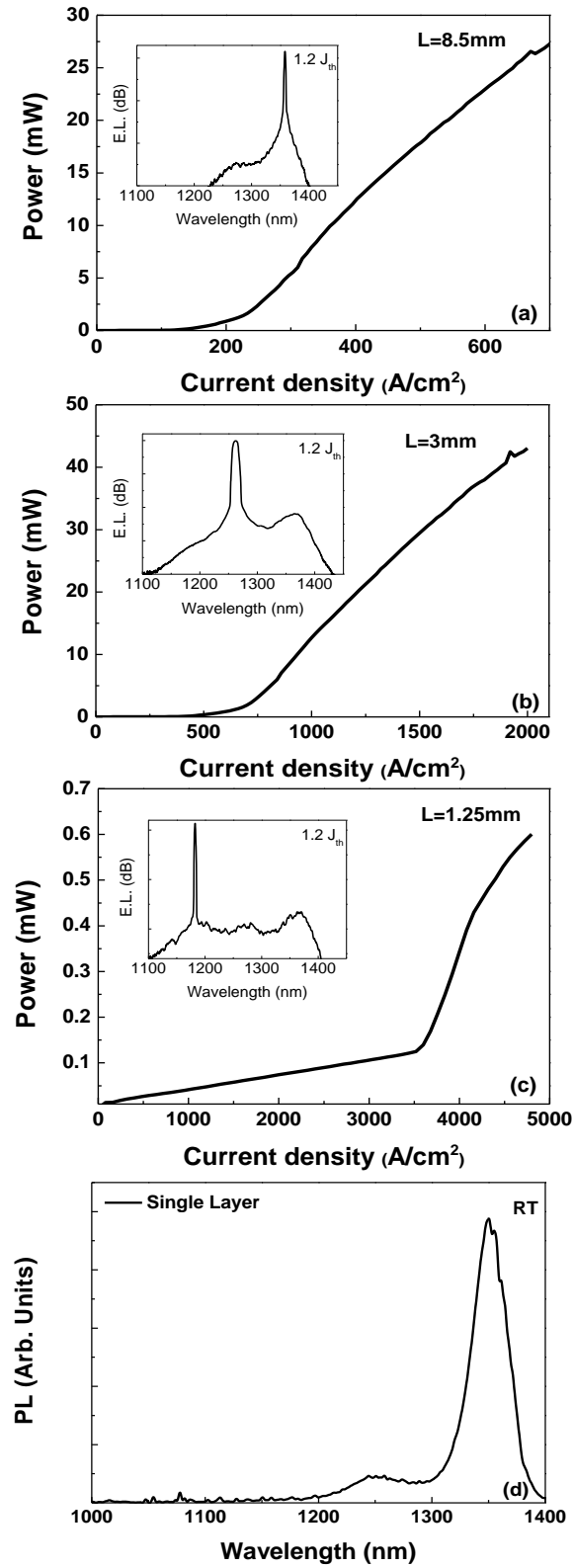
_____

Fig. 3.2. (a-c) Light-current characteristics of single layer InGaAs cap QD laser. Inset shows emission spectrum at 1.2J_{th}. (d) Room temperature PL emission of the test structure.

the second excited state (ES2) of the QD ensemble. At intermediate cavity lengths, dual state lasing is observed, e.g. GS and ES1, ES1 and ES2.

The length dependant characterization of lasers allows the determination of the current density: gain characteristics of the laser material [3.7]. Figure 3.3 shows the experimental dependence of net modal gain on the drive current density for the single layer QD laser described in Fig. 3.2. The curves are obtained by fitting the empirical gain-current relationship given by Zhukov *et al.* [3.8].

$$g = g^{sat}\left[1 - \exp\left(-\phi\frac{J_{th} - J_{tr}}{J_{tr}}\right)\right] \qquad (1)$$
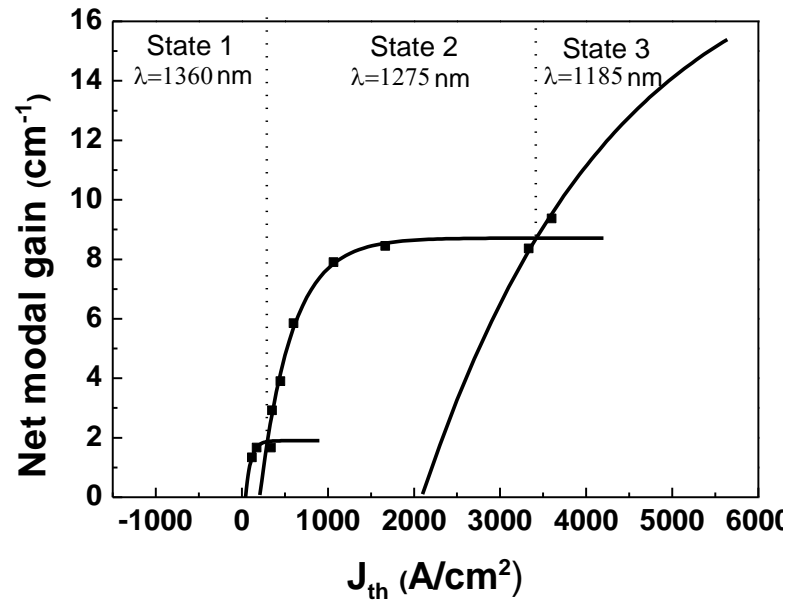
Fig. 3.3. Net modal gain for single layer laser as function of current density. Squares represent experimental data. Full curves show fitting using equation (1).

Where g is the net modal gain; g^{sat} is the saturated net modal gain; ϕ is the fitting parameter; J_{th} is the threshold current density and J_{tr} is the transparency current density. For QD lasers, strong gain saturation effects occur. As cavity length is decreased, there is an increase in the mirror loss (α_m) to a point where the total

_____

cavity loss exceeds the available ground state gain. At this point excited state lasing may occur, accompanied by increased threshold current. As length is decreased further, so the first excited state may be saturated, leading to lasing of the second excited state.

From Fig. 3.3, we observe ground state (1360 nm) saturation at a net modal gain of ~2 cm^{-1}. The first excited state (1275 nm) saturates at a net modal gain of ~8 cm^{-1}. The saturation of the second excited state is not explored. Due to the symmetry of a self-assembled QD, the excited state is expected to have twice the degeneracy of the ground state. Consequently, the saturated modal gain for the excited state is assumed to be twice that of the ground state [3.9]. Considering this an internal loss (α_i) of ~4 cm^{-1} may be deduced, resulting in a modal gain of ~6 cm^{-1} for the ground state and ~12 cm^{-1} for the first excited state.

The ground state modal gain of commercial (Innolume GmbH) 1310 nm material has been measured to be ~25 cm^{-1} [3.9]. These 1310 nm laser structures have areal QD densities of ~4x10^{10} cm^{-2}, with 10 QD layers in a waveguide of similar structure to the ones studied here. The areal QD density of the single layer QD sample is ~ a factor of two lower than in this commercial QD laser material. Furthermore the number of QD layers is a factor of 2 lower at 5 repeats. The ground state modal gain of 6 cm^{-1} from the ground state of these lasers is therefore comparable to commercial 1310 nm QD material considering the factor 4 reduction in the total number of QDs in the laser core.

Figure 3.4 shows the light-current characteristics of the bilayer QD sample for cavity lengths of (a) 4 mm, (b) 1 mm, (c) 0.7 mm. The inset shows the emission spectrum at 1.2 J$_{th}$ for these devices. For the device with 4 mm long cavity
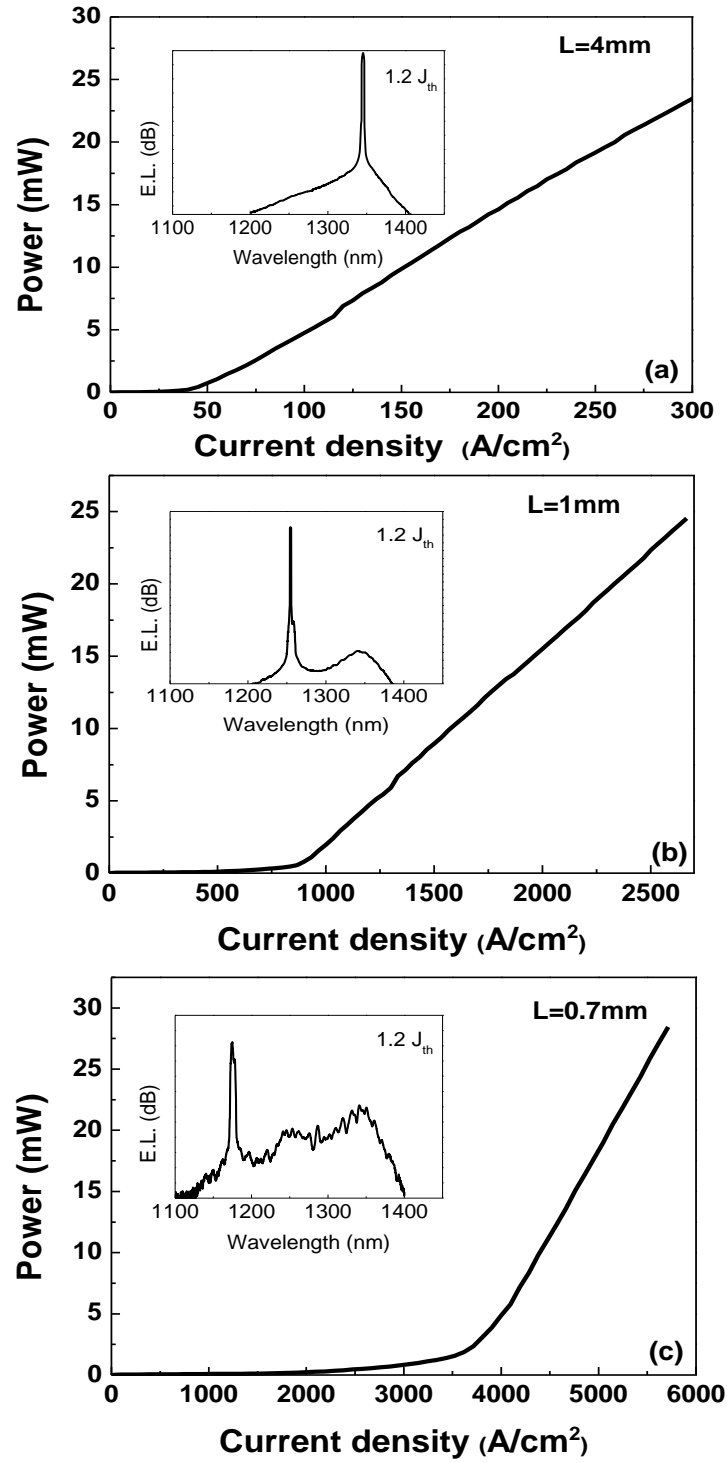
Fig. 3.4. Light-current characteristics of bilayer GaAs cap QD laser. Inset shows emission spectrum at $1.2J_{th}$.

_____

(Fig. 3.4(a)), lasing occurs at 1340 nm with a threshold current density of 38 Acm^{-2} and slope efficiency 0.31 WA^{-1}. In the following we term lasing at this wavelength "state1". For the device with 1 mm cavity length (Fig. 3.4(b)) lasing is observed at 1260 nm with a threshold current density of 815 Acm^{-2} and slope efficiency of 0.25 WA^{-1}. In the following I term lasing at this wavelength "state2". For the device with 0.7 mm cavity length (Fig. 3.4(c)) lasing is observed at 1180 nm with a threshold current density of ~3500 Acm^{-2}, and slope efficiency of 0.30 WA^{-1}. In the following I term lasing at this wavelength "state3". At intermediate cavity lengths, dual state lasing is observed, e.g. State 1 and State 2, State 2 and State 3, which is described in more detail later. Previous work on bilayer QD structures [3.3, 3.4, 3.5, 3.10] suggest that state 1 and state 2 correspond to the ground state and first excited state, respectively of the top QDs in the bilayer. It is likely that state 3 corresponds to an overlap of the ground state of the seed QD layer and the second excited state of the top QD layer.

Figure 3.5 shows the experimental dependence of net modal gain on the drive current density for the bilayer QD laser described in Fig. 3.4. State 1 (1340 nm) saturation is observed at a net modal gain of ~6 cm^{-1}. State 2 (1260 nm) saturates at a net modal gain of ~15 cm^{-1}. The saturation of state 3 is not explored. If I assume that state 1 and state 2 are the ground state and excited states of the top QD layer, respectively, and assume a two-fold increase in degeneracy and saturated modal gain, an internal loss of ~4 cm^{-1} is again deduced. This calculation of internal loss is in good agreement with the one measured from length dependent analysis shown in Fig. 3.6 and multi-section measurements described in the last chapter (see Fig. 2.8 & 2.9). A saturated gain of state 1 (ground state of
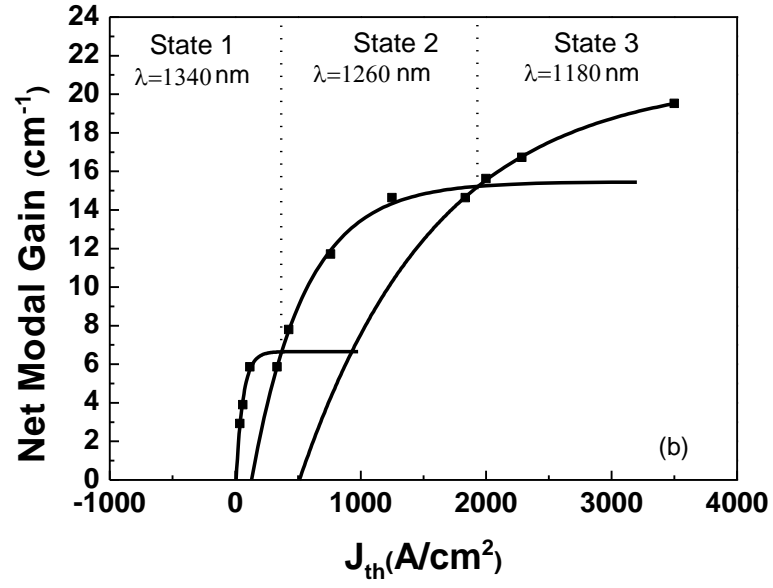
Fig. 3.5. Net modal gain for bilayer GaAs cap laser as function of current density. Squares represent experimental data. Full curves show fitting using equation (1).
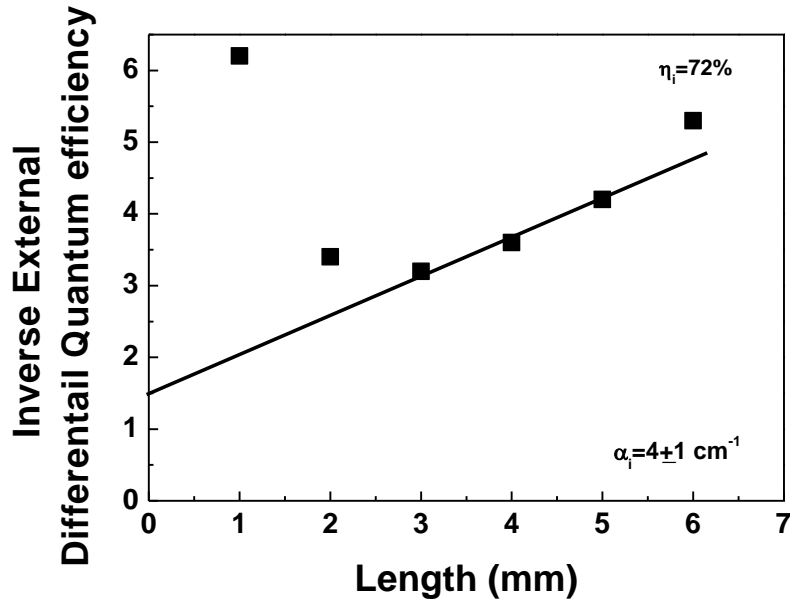

Fig. 3.6. Calculation of internal loss of bilayer QD laser.

_____

top QD layer) of 10 cm^{-1} is obtained, whilst this is ~20 cm^{-1} for state 2 (first excited state of top QD layer). Considering the lower QD areal density and reduced layer number, these figures for saturated gain compare quite favourably with commercial QD material (10 layers) at 1300 nm [3.9].

Defects (threading dislocation, point defects) within active media have previously been shown to result in a leakage current observed in the reverse bias I-V characteristics [3.11-3.17]. In order to compare the material quality of the single and bilayer laser, we have compared it with commercially available sample with 10 single QD layers. For all the samples, broad area lasers with 3mm length and 50 μm wide ridges were electrically characterized at room temperature using a Hewlett-Packard 4155 A semiconductor parameter analyzer. The semiconductor parameter analyzer was programmed to apply a voltage sweep from -20 to 5 V to the probes at a step of 0.01 V and the corresponding diode currents recorded using a long integration time.

Figure 3.7 shows the reverse leakage current plotted as a function of reverse bias for the single QD layer, bilayer, and a commercial 1310 nm QD laser. The electric field at breakdown for the single layer QD laser is ~340 kV/cm, where as for the bilayer and commercial laser it is ~390 kV/cm and ~435 kV/cm respectively. The lower breakdown electric field for single layer sample is expected as high In (26%) concentration introduces strain [3.13, 3.14], and the reverse bias leakage current is sensitive to the amount of strain in the layers. Nevertheless all ridge widths tested for the lasers have sharp breakdown voltage, lower leakage current which is

indicative of the presence of fewer dislocation defects and uniform material quality.
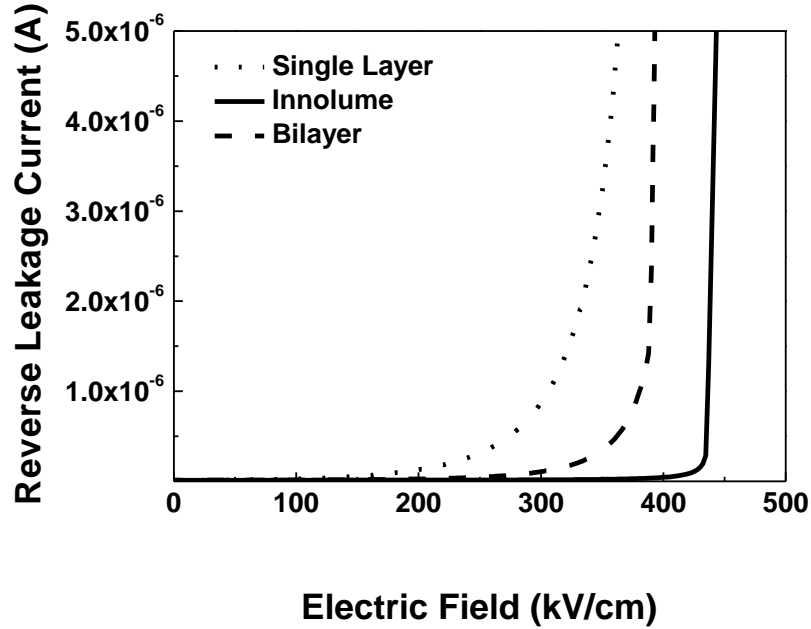
Fig. 3.7. Reverse leakage current as a function of the electric field for single layer, bilayer and Innolume sample.

To further judge the quality of the intrinsic region forward bias I-V characteristics are plotted in Fig. 3.8. The single layer InGaAs cap sample shows a slightly higher leakage, indicating more point defects, which is consistent with the high In (26%) composition. Nevertheless the leakage current of the single layer device is within one order of magnitude as compared to the commercial (Innolume) and bilayer laser at all bias voltages. The ideality factor is between 1.4 and 1.8 comparable to other measurements [3.12, 3.17]. There is no significant change in the slope (usually two slopes appear due to large defects) of these logarithmic plots which is indicative of low defects density [3.17] and similar material quality in the intrinsic region.

Figure 3.9 shows the cross-sectional TEM images of bilayer and single layer QD samples. The TEM images show no threading dislocations or tensile defects (but rough GaAs/AlGaAs interface) to confirm the slightly higher reverse leakage current. However, it has been suggested that a finite number of leakage paths still remain even when using this techniques (forward and reverse analysis).
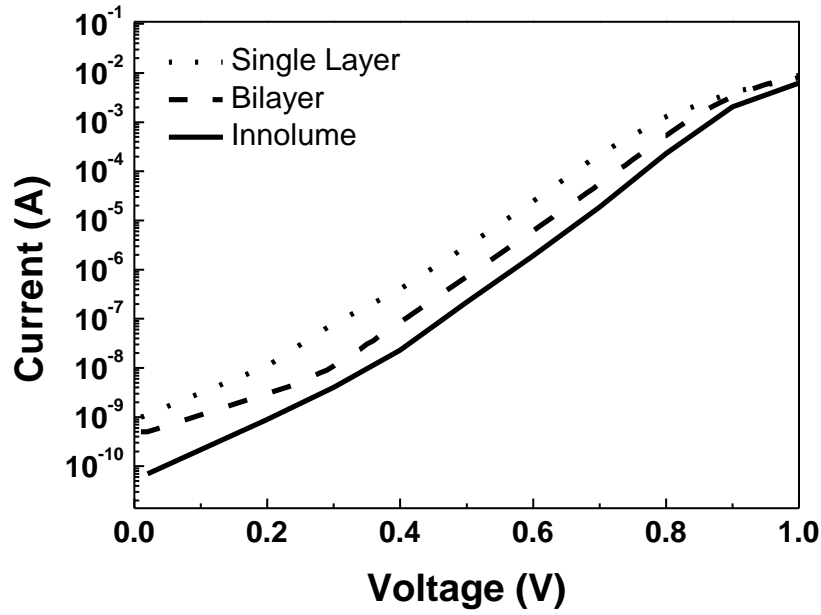
Fig. 3.8. Forward I-V characteristics for single layer, bilayer and Innolume sample.

GaAs capped bilayer QD lasers extends the wavelength to 1340 nm. Similar wavelength extension is obtained with InGaAs capping the single layer QDs with high Indium composition [26%]. However the GaAs capped bilayer laser demonstrated a ~50% increase in saturated modal gain for both the GS and ES1. This is attributed in part to the reduced inhomogeneous linewidth [3.3, 3.4] of the QD ensemble and efficient carrier capture in the upper layer QD [3.4, 3.5]. Extension of the operating wavelength towards 1550 nm is made possible with InGaAs capping the bilayer, with an exciting possibility of fabricating the devices

_____

emitting in the 1300 nm region using QD excited states, which may provide

increased gain, output power and modulation speed over GS operation.
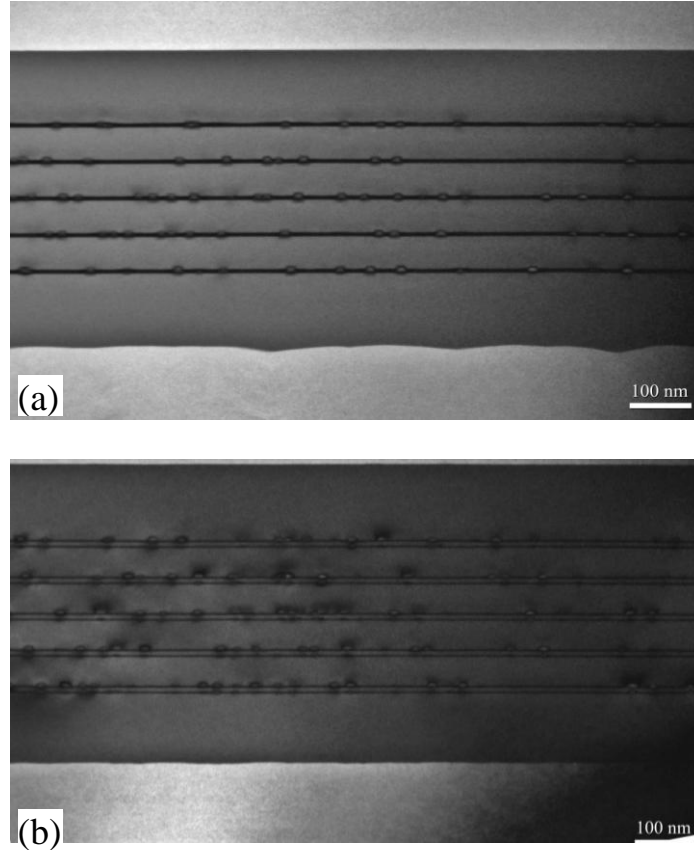
Fig. 3.9. Dark field (002) cross-sectional TEM images obtained from (a) a InGaAs capped single layer sample, (b) a GaAs capped QD bilayer.

Figure 10 shows the (a) light-current characteristics and electroluminescence

spectra (EL) at currents of (b) 30 mA, (c) 75 mA, (d) 1 A, (e) 1.3 A for a GaAs capped

bilayer device with 2 mm cavity length. For this cavity length, lasing occurs initially

from state 1 (ground state of top QD layer) at 1340 nm with a threshold current of

25 mA. Dual state lasing at 1340 nm and 1260 nm (state 1 and state 2, ground

state and excited state of top QD layer) occurring at currents between 75 mA and 1

A. At currents above ~1 A, state 3 begins to lase in addition to strong lasing from state 2 and a small lasing peak from state 1. As a consequence of the blue-shift in lasing wavelength as current is increased, the power is under-estimated at high drive currents (a wavelength of 1340 nm is assumed throughout) indicating an increase in external efficiency with increased current and increasing dominance of state 2 and state 3 in the lasing spectrum. The peak in the ground-state spontaneous emission and lasing wavelength of the ground state are observed to red-shift by no more than 3 nm up to 3 A of pulsed drive current, indicating a self-heating of no more than 5 $^{\circ}$C over this current range. Higher state lasing at high drive current was observed for all cavity lengths.
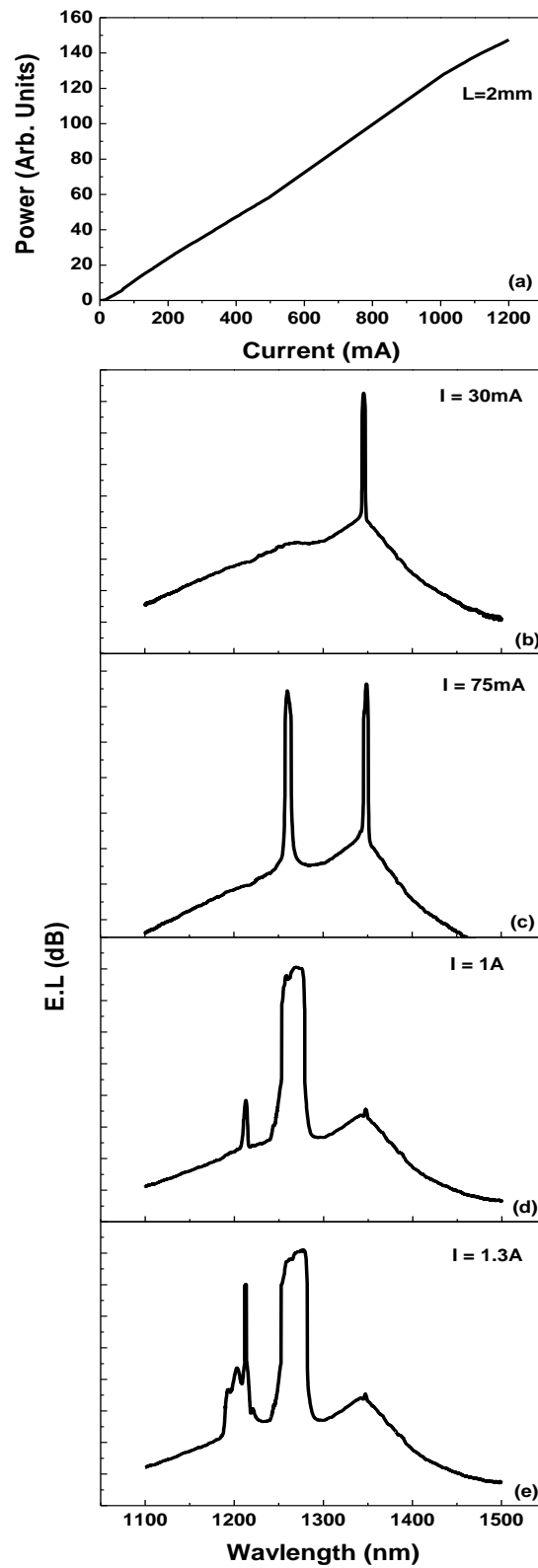
Fig. 3.10. (a) Light-current characteristics of 2mm bilayer GaAs cap QD and electroluminescence spectra at currents of (b) 30 mA, (c) 75 mA, (d) 1 A, (e) 1.3 A .

3.4   Conclusions

In summary, the method of extending the emission wavelength of QDs on GaAs by using a bilayer growth technique has been discussed. The GaAs capped bilayer laser demonstrates twice the modal gain for ground and excited states as compared to an InGaAs capped 'single' layer QD laser operating at similar wavelength (~1350 nm). A unique phenomenon of incomplete gain clamping with three states lasing at high bias was observed without significant heating.

3.5   Future Work

Conventional InAs QD lasers based on InAs dots in a GaAs matrix emitting in the wavelength range ~1000-1200 nm was demonstrated previously [3.18]. An approach to extend the emission wavelength is to cover the InAs QDs with an InGaAs strain reducing layer [3.19], which was also demonstrated using a single layer QD sample. It would be very interesting to fabricate InGaAs capped bilayer samples and compare them with GaAs capped bilayer device. This is discussed in chapter 4. Fabricating high gain excited state laser in the range of 1260-1330 nm covering the O-band of International Telecommunication Union is useful for data comms. This is discussed in chapter 5.

 As outlined earlier the bilayer seed layer acts as a template for growth of the second layer, such that growth conditions can then be chosen to optimize the emission wavelength of the QDs in the second layer (emission layer) while the QD density is determined solely by the density of the seed layer. It would be interesting to study the electrical and optical characteristics of bilayer lasers/multi-

_____

section devices by systematic study varying key growth conditions (growth temperature, deposition rate and InAs coverage) of the seed and emission layer.

Bilayers have shown multi-wavelength emission spanning 150-200nm in the wavelength range of 1100-1300 nm, by optimization of growth parameters one can reduce the spectral dip between GS and ES, which may be useful for optical coherence tomography of the skin tissue (see chapter 6 for details). Also this may provide a good spectral match for existing fiber optic components (telecoms splitters / isolators in 1250-1350 nm).

_____

References

[3.1]   K. Matsuda, K. Ikeda, T. Saiki, H. Tsuchiya, H. Saito, and , K. Nishi, "Homogeneous linewidth broadening in a InGaAs/GaAs single quantum dot at room temperature investigated using a highly sensitive near-field scanning optical microscope," *Phys. Rev. B*. vol. 63, no. 12, pp. 121304-1-121304-4, 2001.

[3.2]   A. E. Zhukov, A. R. Kovsh, N. A. Maleev, S. S. Mikhrin, V. M. Ustinov, A. F. Tsatsul'nikov, M. V. Maximov, B. V. Volovik, D. A. Bedarev, Y. M. Shernyakov, P. S. Kop'ev, and Zh. I. Alferov, "Long-wavelength lasing from multiply stacked InAs/InGaAs quantum dots on GaAs substrates," *Appl. Phys. Lett.*,vol. 75, no. 13, pp. 1926-1928, 1999.

[3.3]   E.C. Le Ru, P. Howe, T.S. Jones, and Murray, R.: "Strain-engineered InAs/GaAs quantum dots for long-wavelength emission," *Phys. Rev. B*, vol. 67, no. 16, pp. 165303-165307, 2003.

[3.4]   E. Clarke, P. Spencer, E. Harbord, P. Howe, and R. Murray, "Growth, optical properties and device characterisation of InAs/GaAs quantum dot bilayers," *J. Phys.: Conf. Series*, vol. 107, pp. 012003-012003-10, 2008.

[3.5]   E. C. Le Ru, A.J. Bennett, C. Robert, and R. Murry, "Strain and electronic interactions in InAs/GaAs quantum dots multilayers for 1300 nm emission," *J. Appl. Phys.*, vol. 91, no. 3, pp. 1365–1370, 2002.

[3.6]   H. Y. Liu, I.R. Sellers, M. Gutierrez, K.M. Groom, W.M. Soong, M. Hopkinson, J.P.R. David, R. Beanland, T.J. Badcock, D.J. Mowbray, and D.J. Skolnick,

_____

"Influence of the spacer layer growth temperature on multilayer InAs/GaAs quantum dot structures," *J. Appl. Phys.*, 2004, vol. 96, pp. 1988–1992.

[3.7]   G. H. B, Thompson "Physics of Semiconductor Laser Devices," New York: Wiley, 1980, ch. 2.

[3.8]   A. E. Zhukov, A. R. Kovsh, V. M. Ustinov, A. Yu. Egorov, N. N. Ledentsov, A. F. Tsatsul'nikov, M. V. Maximov, Yu. M. Shernyakov, V. I. Kopchatov, A. V. Lunev, P. S. Kop'ev, D. Bimberg, and Zh. I. Alferov, "Gain characteristics of quantum dot injection lasers," *Semicond. Sci. Technol.*, vol. 14, no. 1, pp. 118-123, 1999.

[3.9]   B. J. Stevens, D. T. D. Childs, H. Shahid, and R. A. Hogg, "Direct modulation of excited state quantum dot lasers," *Appl. Phys. Lett.*, vol. 95, no. 6, pp. 061101 - 061101-3, 2009.

[3.10] E. Clarke, P. Howe, M. Taylor, P. Spencer, E. Harbord, R. Murray, S. Kahkhodazadeh, D. W. McComb, B. J. Stevens, and R. A. Hogg, "Persistent template effect in InAs/GaAs quantum dot bilayers", *J. Appl. Phys.*, vol. 107, no. 11, pp. 113502-113502-6, 2010.

[3.11] H. Y., Liu, I. R. Sellers, T. J. Badcock, D. J. Mowbray, M. S. Skolnick, K. M. Groom, M. Gutierrez, M. Hopkinson, J. S. Ng, J. P. R. David, and R. Beanland, "Improved performance of 1.3μm multilayer InAs/GaAs quantum-dot lasers using a high-growth-temperature GaAs spacer layer," *Appl. Phys. Lett.*, vol. 85, no. 5, pp. 704–706, 2004.

[3.12] J. W. P. Hsu, "Inhomogeneous spatial distribution of reverse bias leakage in GaN Schottky diodes," *Appl. Phys. Lett.*, vol. 78, no. 12, pp. 1685-1687, 2001.

_____

[3.13]   D. Gershoni, H. Temkin and M. B. Panish, "Strained Layer $Ga_{1-x}In_xAs$/InP Avalanche Photodetectors," *Appl. Phys. Lett.*, vol. 53, no. 4 pp. 1294-1297, 1988.

[3.14] H. Temkin, D. Gershoni, S. N. G. Chu, J. Vandenberg, R. A. Hamm and M. B. Panish, "Critical Layer Thickness in Strained $Ga_{1-x}In_x$/InP Quantum Wells", *Appl. Phys. Lett.*, vol. 55, pp.1669-1672, 1989.

[3.15] E. J. Miller, X. Z. Dang, and E. T. Yu, "Gate leakage current mechanisms in AlGaN/GaN heterostructure field-effect transistors," *J. Appl. Phys.*, vol. 88, no. 10, pp. 5951- 5958, 2000.

[3.16] F. Zhang, D. C. Reynolds, and D. C. Look, "Changes in electrical characteristics associated with degradation of InGaN blue light-emitting diodes" *J. Electron. Mater.*, vol. 29, no. 4, pp. 448-451, 2000.

[3.17] A. R. Saha, S. Chattopadhyay, G. K. Dalapati, S. K. Nandi, C. K. Maiti, "An investigation of electrical and structural properties of Ni-germanosilicided Schottky diode," *Microelectronics Reliability*, vol. 45, no. 7-8, pp. 1154-1160, 2005.

[3.18] D. Bimberg, N. Kirstaedter, N. N. Ledentsov, Zh. I. Alferov, P. S. Kop'ev, and V. M. Ustinov, "InGaAs-GaAs quantum dot lasers," *IEEE J. Select Topics Quantum Electron.*, vol. 3, pp.196 - 205 , 1997.

[3.19] K. Nishi, H. saito, S. Sugou, J. Lee, "A narrow photoluminescence linewidth of 21 meV at 1.35 µm from strain-reduced InAs quantum dots covered by $In_{0.2}Ga_{0.8}As$ grown on GaAs substrates," *Appl. Phys. Lett.*, vol. 74, no.8, pp. 1111-1113, 1999.

Chapter 4

Towards 1550 nm GaAs-based Lasers Using InAs/GaAs Quantum Dot Bilayers

4.1 Introduction

Semiconductor diode lasers incorporating self-assembled quantum dots have received considerable attention because of the expected benefits to device performance arising from the reduced dimensionality of the QD active region, including low and temperature-insensitive threshold currents [4.1, 4.2], increased modulation speed [4.3] and low linewidth enhancement factors [4.4]. The deviation of real QD systems from the ideal model QD ensemble consisting of a homogeneous array of isolated, discrete energy states is a problem for QD laser device engineering, with the peak QD gain generally limited due to strong inhomogeneous broadening caused by fluctuations in QD size and composition. However, self-assembled QDs offer substantially greater wavelength tunability compared to QW-based lasers in the same material system.

Self-assembled QDs are formed via the Stranski-Krastanow growth mechanism, where growth of an epitaxial layer of a material with a different lattice constant than that of the substrate initially proceeds by the formation of a strained two-dimensional (2D) layer (known as the wetting layer), but at a certain critical thickness (usually a few monolayers (ML), depending on the lattice mismatch) the strain is relieved by the formation of three-dimensional (3D) islands. For a limited

range of additional material coverage, these islands remain coherent (dislocation-free) [4.5, 4.6] and once they are capped during subsequent overgrowth, they form nanoscale inclusions within the bulk matrix that may act as 3D potential wells for charge carriers. One of the most extensively studied material systems exhibiting the Stranski-Krastanow growth mode is In(Ga)As/GaAs, for application in near-infrared optoelectronics. There is a 7% lattice mismatch between InAs and GaAs, which limits the thickness and composition of dislocation-free 2D InGaAs layers such that InGaAs/GaAs QW-based devices are typically limited to room temperature emission wavelengths of around 1000 nm. The 2D-3D transition in InAs/GaAs QD growth allows for a greater range in height and, crucially, composition (in excess of that achievable by InGaAs/GaAs QWs), resulting in the extension of the emission wavelength of the QDs, despite the additional quantum confinement or strain effects. This enables the development of InAs/GaAs QD devices operating in the telecoms wavelength windows at 1300 nm [4.7, 4.8] and towards 1550 nm [4.9, 4.10], as an alternative to more traditional InP-based devices, and also for broadband near-infrared light sources for medical imaging [4.11, 4.12].

Mode-locked lasers, making use of the ultrafast absorption/gain recovery of QDs [4.13] are also of increasing interest, in addition to the use of QDs in semiconductor saturable absorber mirrors (SESAMs) [4.14, 4.15] and for non-linear effects in all-optical switching [4.16]. An InAs/GaAs QD laser operating at 1300 nm was first demonstrated in 1998 [4.17] and such devices have now reached commercialization.

Emission and lasing at 1550 nm have been achieved from InP-based QD and quantum dash lasers [4.18, 4.19], but development of GaAs-based 1550 nm emitters is attractive because of the deeper confining potential, that offers possible improvements in the temperature insensitivity of devices, the monolithic integration of GaAs/Al(Ga)As distributed Bragg reflectors with high refractive index contrast, suitable for vertical cavity surface-emitting structures, and advantages in device fabrication in GaAs such as the availability of larger substrates and advanced processing techniques for novel devices, for example for photonic crystals.

Progress towards 1550 nm emission from InAs/GaAs QDs has been less widely reported and requires careful control of the growth conditions and specialized growth techniques. To achieve the maximum extension of the QD emission wavelength, optimization of the QD size, composition and strain state is required, and all of the reported strategies for achieving long-wavelength emission from QDs address one or more of these parameters. Established growth techniques for achieving room temperature emission at 1300 nm from InAs/GaAs QDs include using low growth rates [4.20], alternate layer epitaxy (ALE) [4.21], capping the QDs with a thin layer of InGaAs rather than GaAs [4.22] or incorporating the QDs into an InGaAs QW (dots-in-a-well or DWELL technique) [4.23]. Reducing the growth rate (or modifying it by ALE) results in large, In-rich QDs at a lower density than for faster growth rates under the same conditions [4.24]. However, as the growth rate is further reduced, the QDs reach an optimum size with their room temperature emission wavelength saturating at around 1400 nm [4.25, 4.26], and the resulting QD density ($10^8 - 10^9$ cm^{-2}) is also too low to achieve sufficient gain in laser structures. InGaAs capping of QDs or the use of DWELLs provides local strain

reduction and also preserved the QD height and composition during capping, all of which contribute to extending the emission wavelength of the QDs, typically by 100-150 nm from ~1150 nm to ~1300nm [4.22, 4.23]. However, extension of the QD emission beyond 1400 nm by these techniques requires either very high In-content capping layers, that may introduce dislocations and be detrimental to device performance [4.27], or a rethink of the approach taken. There have been relatively few reports of room temperature emission from InAs/GaAs-based QDs beyond 1500 nm, using high In-content InGaAs caps grown by metalorganic chemical vapor deposition [4.28, 4.29], modified capping layer compositions using N or Sb [4.30, 4.31] or growth on metamorphic buffers so that the surrounding matrix is of InGaAs rather than GaAs [4.10].

Rather than using individual layers, we can instead exploit the strain interactions between two closely stacked QD layers to provide additional control over the QD growth conditions. For a separation between QD layers of up to 20 nm, strain fields due to the underlying QD layer (the seed layer) will provide preferential nucleation sites for QDs in upper layers [4.32, 4.33], such that the seed layer acts as a template for growth of the second layer. Growth conditions can then be chosen to optimize the emission wavelength of the QDs in the upper layer while the QD density is determined solely by the density of the seed layer [4.33-4.35].

In this chapter I briefly examine the structural and optical properties that give rise to the long-wavelength emission of these closely-stacked QD systems (hereafter referred to as QD bilayers), and demonstrate edge-emitting laser structures incorporating GaAs-capped and InGaAs-capped QD bilayers. Room temperature

electroluminescence (EL) at 1515 nm and lasing at up to 1420 nm is observed from these devices, and we present gain and absorption spectra obtained by characterization of multi-section lasers. Under high bias conditions, asymmetric broadening of the gain peaks towards longer wavelengths is observed, which results in positive net modal gain beyond 1500 nm for a laser incorporating InGaAs-capped QD bilayers. The origin of the gain broadening is discussed.

4.2   Growth of InAs/GaAs QD Bilayers

It is well established that close stacking of QD layers leads to the correlation of QDs in different layers, arising from strain-dependent preferential nucleation sites for QDs in the upper layers. Cross-section transmission electron microscopy (TEM) measurements show that for layer separations of <20 nm, QDs will be vertically correlated and will increase in size in upper layers because of the earlier onset of the 2D-3D transition at the preferential nucleation sites above buried QDs [4.32]. For two InAs QD layers separated by 10 nm GaAs, in situ reflection high-energy electron diffraction measurements during growth show that the 2D-3D transition is reached ~25% earlier for the second layer than for the first layer and the critical thickness for island formation in the second layer is temperature-insensitive over a wide temperature range, indicating that island formation is determined by the template effect of the seed layer rather than thermal effects [4.36]. Although QDs in the upper layer are larger, their emission wavelength is blueshifted with respect to the seed layer (when grown at the same growth rate and temperature) because of increased strain-driven compositional intermixing [4.37, 4.38]. However, this blueshift can be counteracted by modification of the growth conditions without

affecting the QD density (which is set by the seed layer), for example by increasing

the InAs coverage [4.39], increasing the growth rate [4.40], or most significantly by

reducing the growth temperature to inhibit the intermixing [4.34].

 The atomic force microscopy (AFM) images in Fig. 4.1 illustrate the template effect

of an underlying seed layer. Fig. 4.1(a) and 4.1(c) show 1 µm x 1 µm AFM images

obtained from the uncapped upper layers of QD bilayers, both grown under the

same conditions (by deposition of 3.3 ML InAs at a growth temperature of 467 ^{o}C),

but for which the seed layers have been grown at different temperatures: for (a) at

480 ^{o}C, resulting in a reasonably high QD density of 2.7 x 10^{10} cm^{-2}, and for (c) at

500 ^{o}C, resulting in a lower QD density of 1.2 x 10^{10} cm^{-2}. The change in density in

the seed layer is matched in the upper layer, despite the identical growth

conditions for the upper layers.
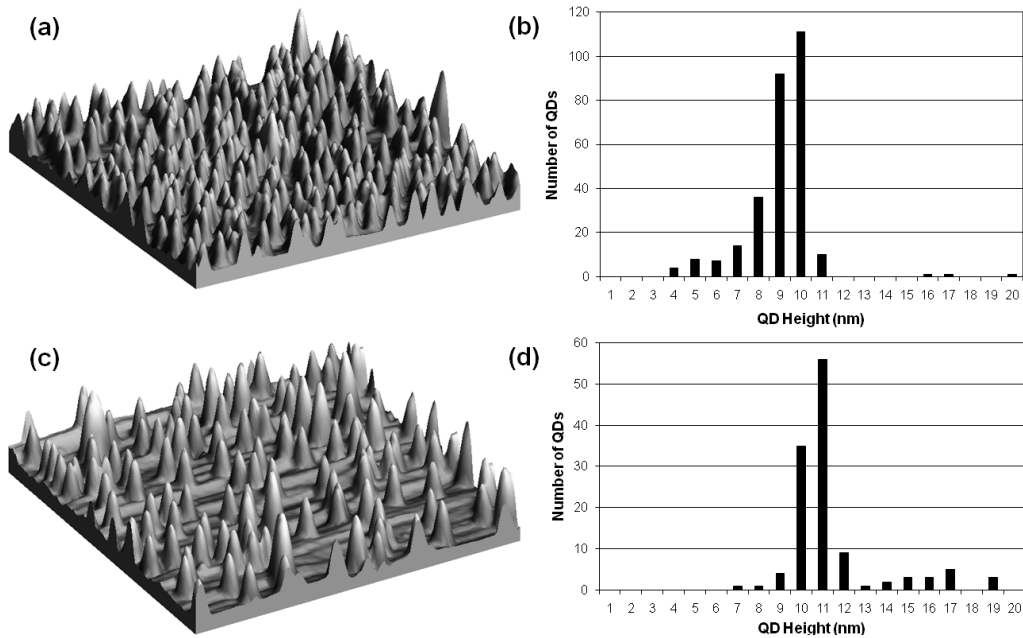
Courtesy Edmund clarke

Fig. 4.1. (a) 1 µm x 1 µm (z-range = 20 nm) AFM image of uncapped QDs in the second layer of a QD bilayer with a high density seed layer, with (b) the distribution of island heights. (c) 1 µm x 1 µm (z-range = 20 nm) AFM image of uncapped QDs in the second layer of a QD bilayer with a low density seed layer, with (d) the distribution of island heights.

The average height of QDs shown in Fig. 4.1(c) is 11.3 ± 2.2 nm, compared to an average height of 9.0 ± 1.6 nm for the QDs in Fig. 4.1(a). This increase is a consequence of the same amount of deposited material being distributed amongst fewer islands, resulting in a narrower distribution of larger islands. The upper layer of QDs in the bilayer are grown and capped at sufficiently low temperature to inhibit In/Ga intermixing. This results in the formation of large, In-rich QDs, as can be seen in the cross-section TEM image of a GaAs-capped bilayer shown in Fig. 4.2(a).
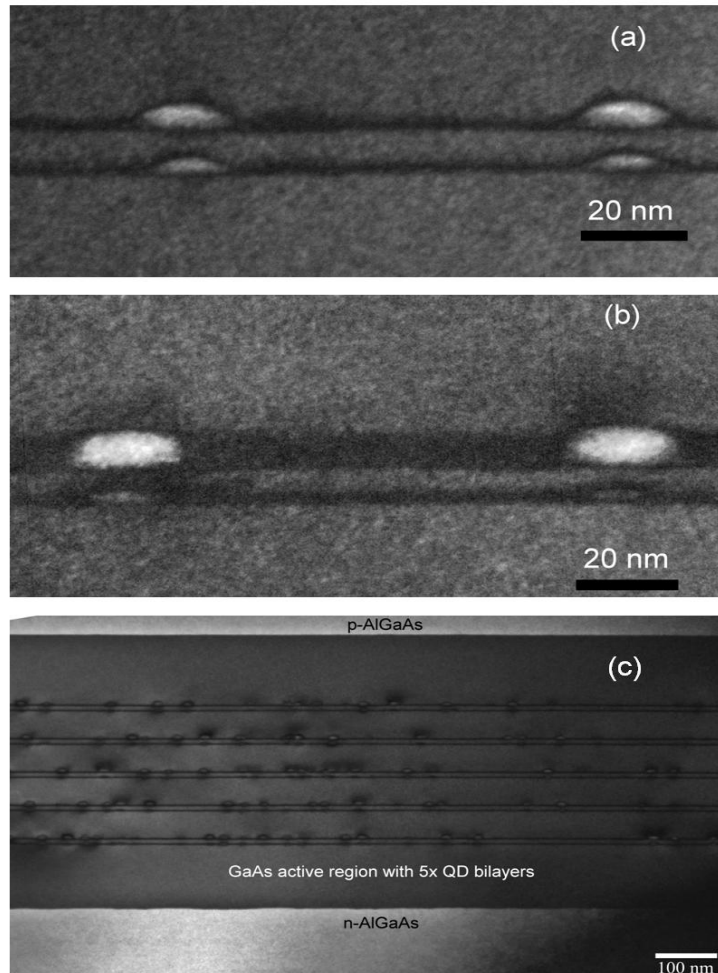

Fig. 4.2. Dark field (002) cross-sectional TEM images obtained from (a) a GaAs-capped QD bilayer, (b) an InGaAs-capped QD bilayer, and (c) the active region of a laser incorporating five GaAs-capped bilayers

_____

The QDs in the upper layer are around 5-6 nm in height, compared to 2-3 nm for

the seed layer. The increased size of the QD, the high In composition and the strain

relief from the underlying seed layer QD all contribute to an extension of the

emission wavelength of the QDs in the upper layer, up to 1400 nm at room

temperature [4.35]. However using the bilayer growth technique, this wavelength

can now be achieved at suitable QD densities for laser applications, and the

emission wavelength can be further extended using an InGaAs cap. An InGaAs-

capped bilayer is shown in the TEM image in Fig. 4.2(b). This bilayer was grown

under the same conditions as for the bilayer shown in Fig. 4.2(a), but was capped

by a 4 nm $In_{0.18}Ga_{0.78}As$ layer prior to subsequent GaAs growth. The size of the

seed layer QDs is similar in both samples, but in the InGaAs-capped sample, the

QDs in the upper layer remain larger and more In-rich because the out-diffusion of

In from the QDs during capping is suppressed [4.41]. In order to achieve sufficient

gain for lasing, multiple bilayers can be incorporated into the active region of a

device. Fig. 4.2(c) shows a cross-section TEM image of a 500 nm-thick GaAs active

region of an edge-emitting laser, containing five InAs QD bilayers each separated by

50 nm. There is a high degree of vertical correlation between QDs within each

bilayer, but the bilayers are sufficiently separated so that growth of each bilayer is

not significantly influenced by underlying layers, enabling coincident emission (and

gain) from each layer [4.42].

Figure 4.3 shows a low temperature (10 K) photoluminescence (PL) spectrum

obtained from a single InGaAs-capped bilayer under low power excitation

conditions (an excitation density of 0.5 Wcm^{-2} from a HeNe laser), demonstrating

the extended emission wavelength and the exceptionally narrow inhomogeneous

linewidth that can be obtained from these highly uniform QDs. A single PL peak is

observed at 0.95 eV (corresponding to an emission wavelength of 1310 nm),

originating from optical transitions in the upper layer QDs. Emission from the seed

layer (expected at ~1200 nm) is suppressed due to efficient carrier transfer from

the seed layer to the upper layer QDs. Previous studies have demonstrated

efficient electronic coupling between
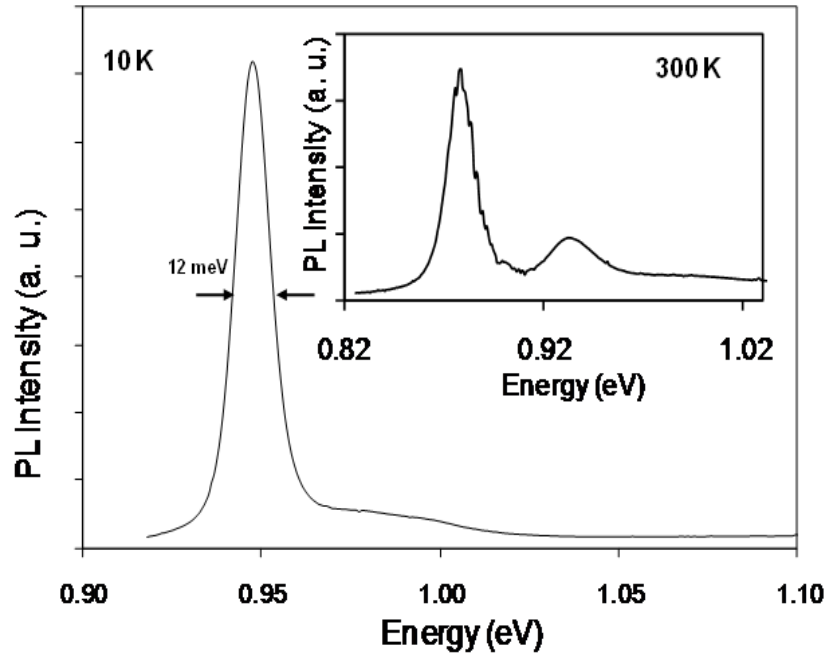
Fig. 4.3. Low temperature (10 K) PL spectrum obtained from an InGaAs-capped QD bilayer under low power HeNe laser excitation (0.5 W cm^{-2}). Inset: room temperature PL spectrum obtained from the same sample under similar excitation conditions. Noise on the high energy side of the main PL peak is due to water absorption

QDs with a similar separation (a GaAs spacer layer thickness of 10 nm between the

QD layers, although as can be seen in the TEM images in Figs. 4.2(a), (b), the actual

barrier thickness between a pair of QDs is around 5 nm) [4.33, 4.42], with an

estimated excitation transfer time of 20 ps [4.43], which is short compared to the

ground state radiative lifetime of the QDs of around 1 ns. The high degree of

uniformity of the bilayer QD ensemble is attributed to a reduction in QD height

fluctuations due to the reduced growth temperature and a more uniform composition due to the suppressed intermixing during capping [4.34]. The InGaAs cap further preserves the QD height and composition during capping, also contributing to the increased uniformity of the QDs [4.22, 4.41] and the resulting inhomogeneous broadening of 12 meV is comparable to the lowest PL linewidth reported for any QD ensemble (also from an InGaAs-capped QD bilayer) [4.44]. As the temperature is increased to 300 K (inset to Fig. 4.3), the emission wavelength reaches 1410 nm and there is a modest increase in the PL linewidth to 15 meV. To achieve the minimum inhomogeneous broadening requires optimization of both the spacer layer thickness [4.33], capping layer composition and also the growth conditions for both the seed layer and the second layer QDs (see for example the variation in QD height distributions in Fig. 4.1), but typical room temperature PL linewidths from QD bilayers will be in the range 15-25 meV at moderate excitation densities. This is attractive for device applications, with low inhomogeneous broadening expected to bring benefits for the peak gain, threshold current and modulation bandwidth of QD lasers [4.45, 4.46].

4.3 Device Description and Experimental Details

Three device structures were investigated, each containing five InAs/GaAs QD bilayers. Each of the samples were edge-emitting laser structures grown on n+ GaAs substrates, with a 500 nm GaAs active region containing the QD bilayers (each separated by 50 nm), surrounded by 1500 nm doped AlGaAs layers and a 400 nm p+ GaAs contact layer completing the structure. Samples A and B were used to investigate the effect of InGaAs-capping on the electroluminescence (EL) and lasing

performance of the QD bilayers. For these samples the seed layer was grown at a temperature of 480 ^{o}C by the deposition of 2.4 ML of InAs at a growth rate of 0.014 MLs^{-1}, giving a QD density of 2.7 x 10^{10} cm^{-2}. The seed QD layer was capped by 10 nm of GaAs spacer layer, also grown at 480 ^{o}C, before the temperature was raised to 580 ^{o}C for 10 minutes to smooth the growth surface and desorb segregated indium [4.47]. The emission layer was then grown at a reduced temperature of 467 ^{o}C by the deposition of 3.3 ML of InAs at the same growth rate as for the seed layer. For sample A, the QDs were then capped with 15 nm of GaAs, whereas the second QD layers in sample B were capped by 4 nm In$_{0.18}$Ga$_{0.82}$As followed by 11 nm GaAs, also at 467 ^{o}C, after which the temperature was ramped to 580 ^{o}C for subsequent GaAs growth. Fig.s 4.2(a) and 4.2(b) show TEM images of the bilayers in samples A and B respectively, and Fig. 4.2(c) shows the active region of sample A. The growth conditions for the QD bilayers in sample C were chosen to provide the greatest extension of the emission wavelength: for this sample, the seed layer was grown at a higher temperature of 505 ^{o}C, which yields a low density (7 x 10^9 cm^{-2}) of larger QDs, leading to a concomitant increase in the size of the QDs in the second layer and an extension in their emission wavelength, but the reduction in density means that there were insufficient QDs to achieve ground state lasing with as-cleaved facets in the range of device lengths (up to 8 mm) that we have investigated here [4.35]. The In composition of the InGaAs cap was also increased, so that the second layer QDs were now capped by 4 nm In$_{0.26}$Ga$_{0.74}$As. Wafers were processed into broad area lasers (5 to 100 μm width) to characterize the electroluminescence and lasing from the samples, and into multi-section lasers to obtain gain and absorption spectra. All measurements were performed at a heat

sink temperature of 300 K. The segmented contact method discussed in chapter 2 was employed to obtain gain and absorption spectra [4.48].

4.4 Device Characterization

Figure 4.4(a) shows edge-emission EL spectra with increasing current density (70-350 Acm^{-2}), obtained from a broad area laser fabricated from sample A, where lasing is inhibited (device length 1 mm). The EL spectra are made up of spontaneous emission which is then convoluted by the gain/absorption spectrum as the emission traverses the waveguide, and so does not provide a direct comparison of gain. Emission at 1340 nm and 1260 nm for the GaAs-capped samples is attributed to emission from the ground state and first excited state of the second layer QDs, respectively.

Figure 4(b) shows EL spectra obtained under similar conditions from sample B. There is an extension of the ground state and first excited state emission compared to sample A to 1420 nm and 1330 nm respectively, which is due to the InGaAs capping of the upper QD layers in this sample. Room temperature emission from the ground state of the seed layer QDs grown under these conditions is at ~1200 nm and a small peak at this wavelength is only observed at very high current densities for sample A, which may be due to a combination of emission from the seed layer and the second excited state of the upper layer QDs. The suppression of emission from these QDs in all samples indicates that the efficient electronic
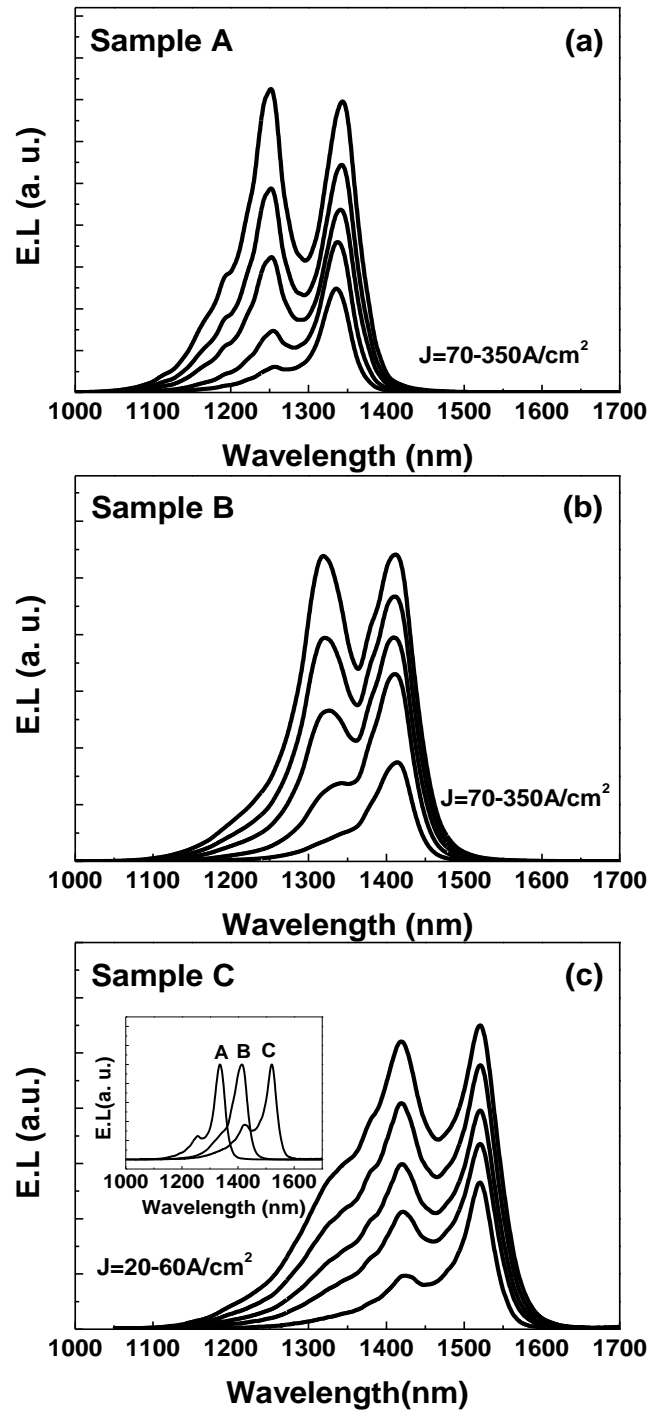
Fig. 4.4. Room temperature EL spectra obtained from broad area lasers fabricated from samples A, B and C over a range of current densities. Spectra are not corrected for water absorption. Inset to figure (c): comparison of normalized EL spectra obtained at lowest current densities from each sample.

coupling between the QD layers in each bilayer persists even at reasonably high carrier injection levels, and emission is only observed once lower-lying states in the upper layer QDs are occupied. The room temperature EL linewidth of the ground state of sample A is 25 meV, which is comparable to a room temperature PL linewidth of 21 meV from a single QD bilayer grown under the same conditions, indicating that emission from all five layers in sample A are coincident. Sample B has a slightly broader room temperature EL linewidth of 29 meV. The current density required to achieve equal emission intensity between the ground state and the first excited state is approximately the same for both samples A and B (350 Acm^{-2}); considering an essentially equal QD areal density and number of QD layers for each sample, this indicates similar carrier lifetimes in each device, despite the incorporation of an InGaAs cap in sample B.

Figure 4.4(c) shows EL spectra obtained from a broad area laser fabricated from sample C as a function of current density (20-60 Acm^{-2}). Sample C has a similar EL linewidth to sample A (23 meV), which is again comparable to the PL linewidth of an individual QD bilayer grown under the same conditions. The reduction in the current density required to achieve equal intensity of emission from both the ground state (at 1515 nm) and the first excited state (at 1430 nm) for sample C (60 Acm^{-2}) compared to samples A and B (350 Acm^{-2}), is unsurprising since sample C has ~1/4 the areal density of QDs compared to samples A or B. The spectral features around 1380 nm observed in Fig.s 4(b) and 4(c) are due to water absorption. The inset to Fig. 4(c) shows a comparison between the normalized EL spectra obtained from samples A, B and C at low-threshold current density, demonstrating the extension in the emission wavelength between samples A and B

due to the introduction of an InGaAs cap, and for sample C where both the QD

growth conditions and the InGaAs cap composition and thickness were optimized

to achieve the maximum extension in emission wavelength. Broad area lasers of

lengths up to 8 mm (with as-cleaved facets) from sample C were fabricated and
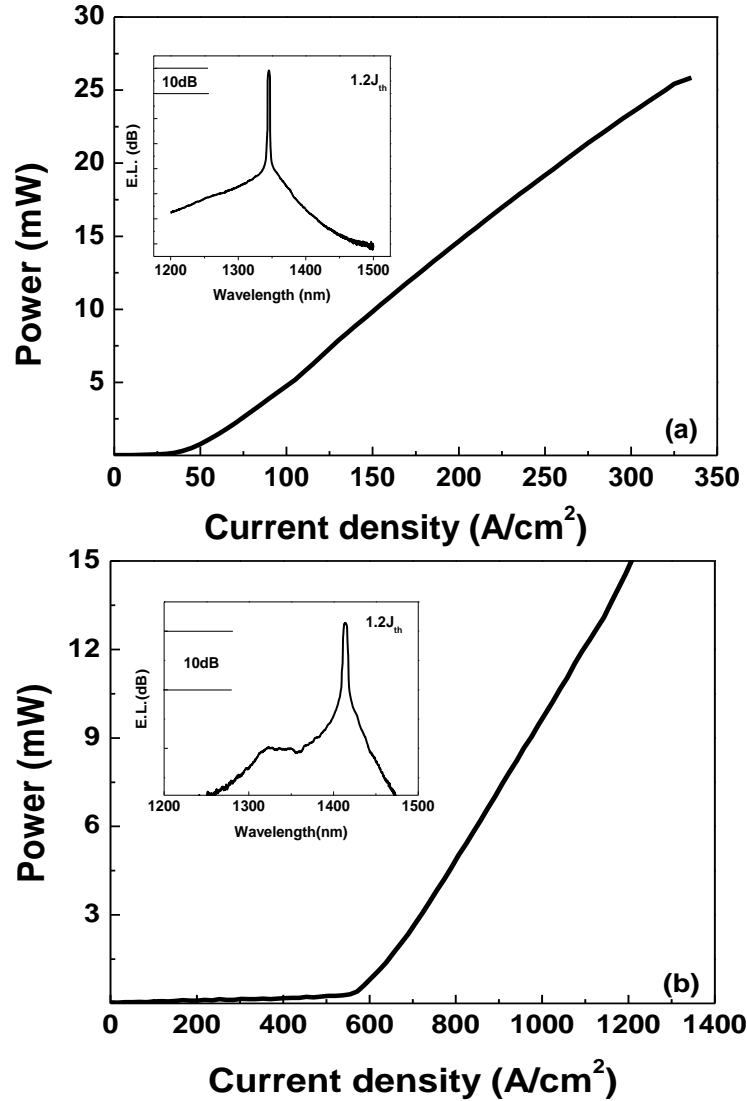
Fig. 4.5. (a) Total optical power (from both as-cleaved facets) as a function of current density from a 4 mm-long broad area laser fabricated from sample A. Inset: room temperature lasing spectrum obtained at a current injection of 1.2 x threshold current density (J_{th}). (b) Total optical power as a function of current density from an 8.7 mm-long broad area laser fabricated from sample B. Inset: room temperature lasing spectrum obtained at 1.2 x J_{th}.

tested but ground state lasing was not observed from this material, probably due to an insufficient QD density in this sample. This could be overcome by incorporation of more QD bilayers into the active region or application of high-reflection coatings to the laser facets, but the results presented here indicate that this growth technique is immediately applicable to saturable absorption devices such as SESAMs [4.14, 4.15] or non-linear devices [4.16].

Figure 4.5(a) shows typical power-current characteristics of a 4 mm long ridge laser device fabricated from sample A, measuring the total output power from both as-cleaved facets using pulsed excitation with a pulse duration of 5 µs and a 1% duty cycle to minimize heating. The laser exhibits ground state lasing at 1340 nm with a threshold current density (J_{th}) of 35 Acm^{-2} and a slope efficiency is 0.35 W/A. The inset shows the lasing spectra at 1.2 times J_{th}.

Figure 4.5(b) shows power-current characteristics of an 8.7 mm long ridge laser device fabricated from sample B, using the same measurement conditions as for sample A. The laser exhibits ground state lasing at 1420 nm, but with a higher J_{th} of 550 Acm^{-2} and a reduced slope efficiency of 0.08 W/A. The lasing wavelengths for both samples A and B match the ground state EL peaks observed in Fig. 4.4. The increased device length required to achieve ground state lasing (and corresponding increase in J_{th}) and the decrease in slope efficiency for sample B is attributed to increased optical losses due to roughness of one of the GaAs/AlGaAs interfaces in this sample, observed by TEM (see Fig. 4.6).

Figure 4.7 shows the modal absorption spectra obtained from the multi-section devices fabricated from sample A and B respectively. Figure 4.8 plots absorption
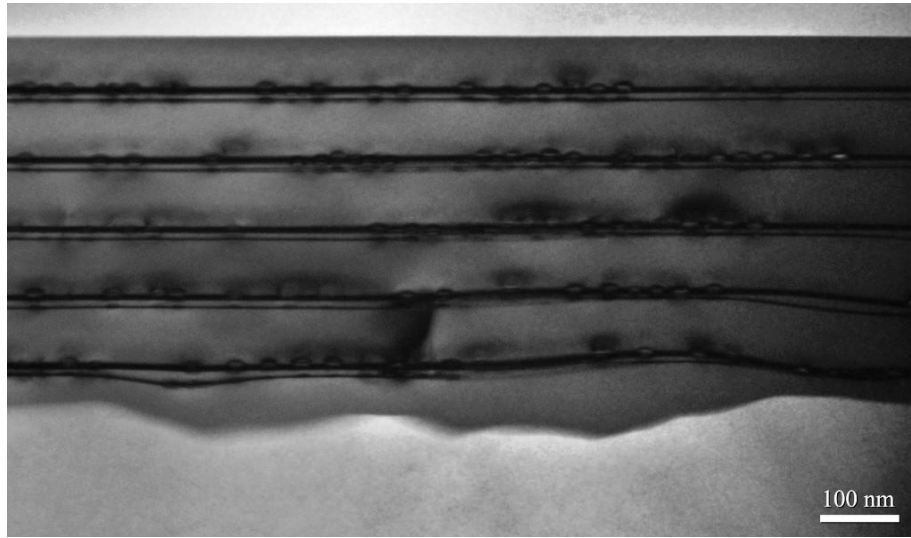
Fig. 4.6. Dark field (002) cross-sectional TEM images obtained from an InGaAs-capped QD bilayer, showing the roughness of one of the GaAs/AlGaAs interfaces.
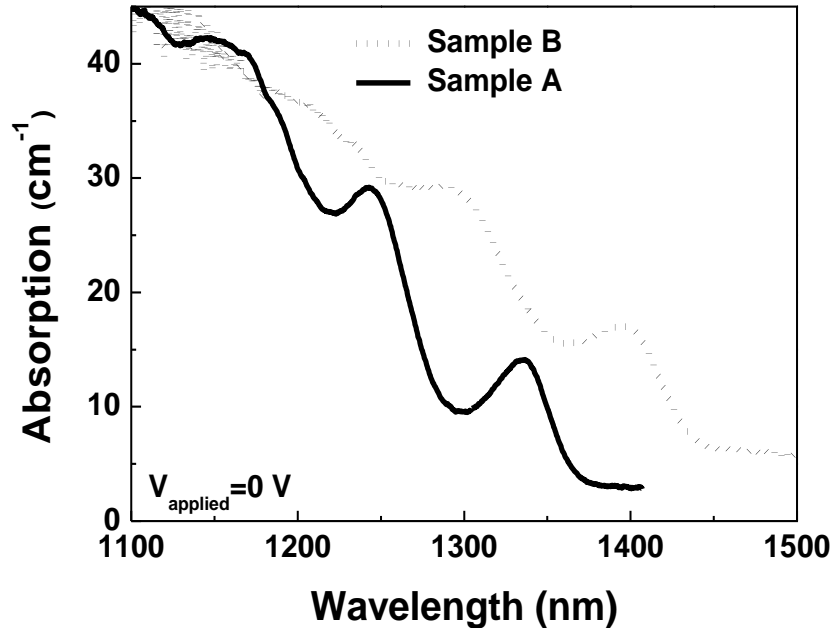
Fig. 4.7. Zero-bias absorption spectra obtained from multi-section devices fabricated from samples A and B.

_____

spectra as a function of current density (J) in the light emitting segment obtained

from multi-section devices fabricated from samples A. The data of sample A

(similarly sample B) in Fig. 4.7 is obtained at a current density of 3 kA/cm^2 where no

bleaching is observed. The absorption peaks arising from the ground state and the

first excited state of both samples are clearly observed, and the shift in the ground

state absorption peak between sample A and sample B indicates that these

transitions must be related to the upper QD layer.

The increased internal loss for sample B is in line with the increased roughness of

the lower AlGaAs/GaAs interface observed in TEM images, as mentioned

previously. Subtracting α_i for each sample gives a very similar ground state peak

absorption of 11 cm^{-1} for both samples; as the QD densities are nominally the same

Fig. 4.8. Zero-bias absorption spectra as a function of current density (J) in the light emitting segment obtained from multi-section devices fabricated from samples A.

in both samples this also indicates that there are a similar number of optically active QDs in each sample, and this is not affected by the introduction of the InGaAs cap in sample B.
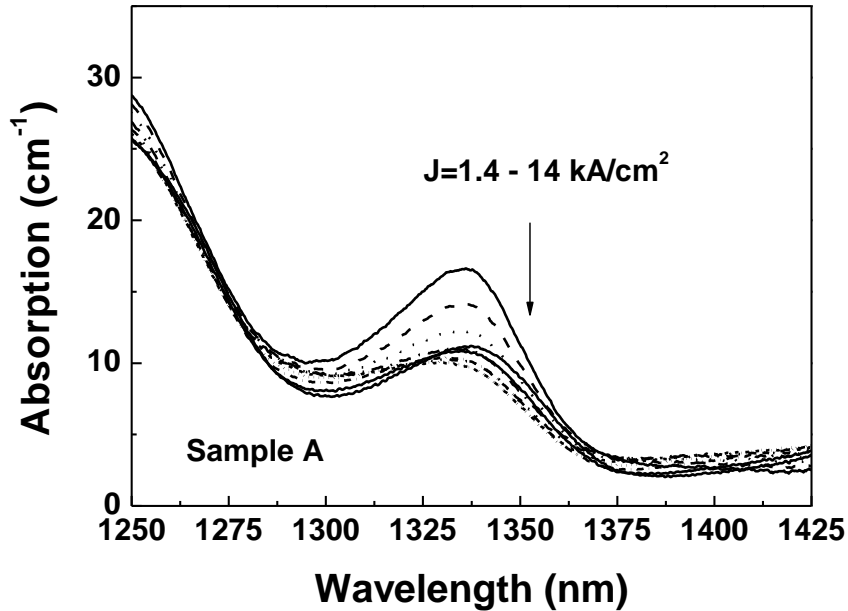
Figure 4.9(a) shows absorption spectra (0 V applied bias), and gain spectra (1 kAcm^{-1}) obtained using the segmented contact method described previously for sample A at room temperature. At long wavelengths both spectra converge at the same internal loss ($\alpha i = 3.0 \pm 0.5$ cm^{-1}). In the absorption spectrum the ground state and first excited state are observed at 1335 nm, and 1245 nm. The corresponding transitions in the gain spectrum are observed at 1370 nm and 1260 nm. This shift between the absorption and gain spectrum of quantum dots can be attributed to the Coulomb interaction between the QDs and neighboring charge [4.49]. Higher order transitions (1150 nm in absorption, 1180 nm and shoulder at 1135 nm in gain spectrum) are also observed. The assignment of these transitions is difficult in this coupled QD system at high dot carrier occupancies, and in the remainder, the peak observed at 1150 nm in absorption (1180 nm in the gain spectrum) is referred to as "state 3". We note that the values for absorption at the ground state and first excited state peaks are significantly larger than the corresponding gain [4.48, 4.50].

The effect of free carriers on the gain spectrum of QD lasers has recently been reported [4.51]. A redshift of the experimentally obtained gain peak of 6 meV from the modeled gain peak was observed at relatively low carrier occupancies, consistent with the operation of a ground-state QD laser (around 2-3 electron-hole pairs per QD). Shifts of around 20 meV have been predicted due to Coulomb interactions for the case of PL from a single QD [4.52], and in the gain spectrum of
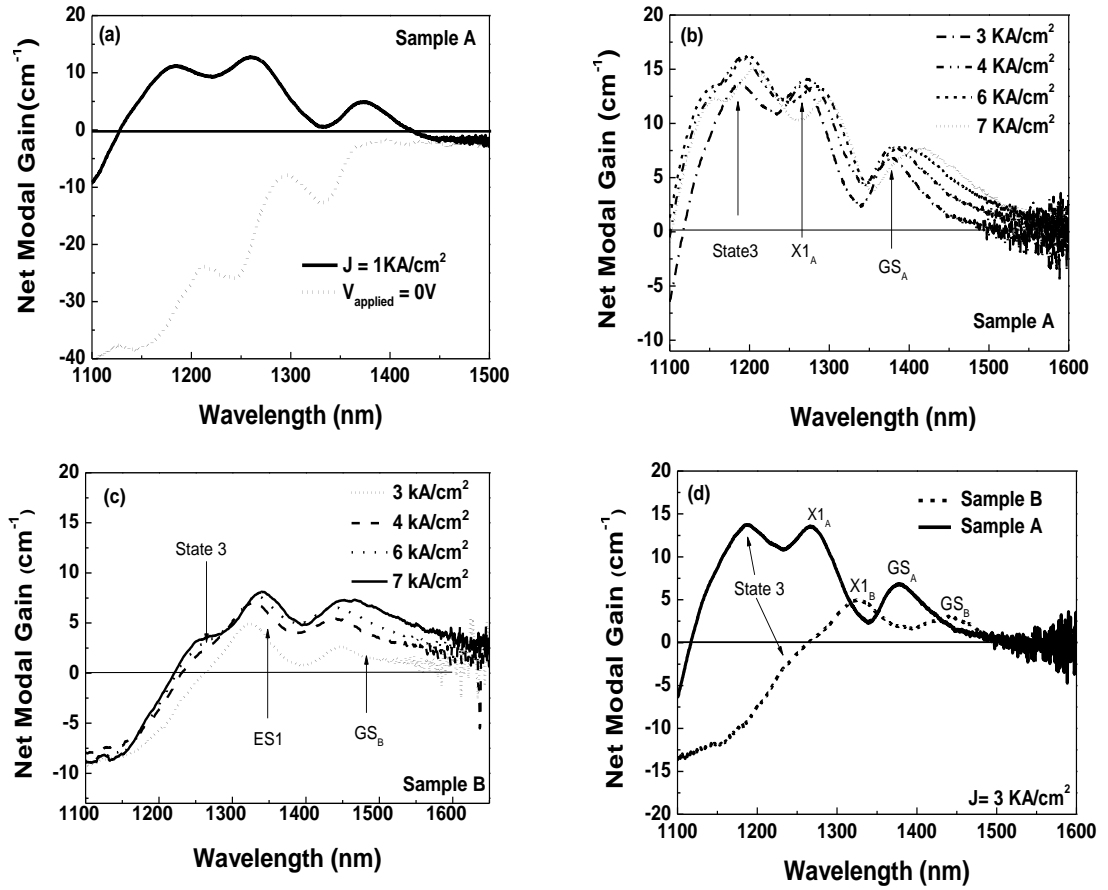
Fig. 4.9. (a) Room temperature gain spectra obtained from sample A and zero-bias and at GS transparency, (b) high current density gain spectra obtained from sample A, (c) high current density gain spectra obtained from sample A,(d) comparison of gain spectra obtained from samples A and B at an injection current density of 3 kAcm^{-2}.

QD lasers [4.49]. In both cases ~15 electron-hole pairs were required to produce a 20 meV shift in the emission/gain spectra, consistent with the level of occupancy of the QDs in Fig 4.9(b), where the first excited state is filled and strong gain is obtained from higher order states. In addition to the large shift in emission energy, we observe a strong asymmetric broadening of the ground state peak. Elastic electron-hole scattering has been predicted to produce significant broadening to the emission from a QD [4.52]. Another factor in the asymmetric broadening of the peak may be that each dot within the ensemble will instantaneously have different dot occupancies. As the shift of individual QDs is a function of carrier occupancy of

the QD we can expect an additional broadening mechanism which would asymmetrically modify the QD ground state gain and emission spectra. We are not aware of any theoretical treatment of many-body effects in QDs with multiple bound states.

Figure 4.9(c) shows the evolution of the gain spectra for sample B as a function of drive current density. A shift of the ground state, first excited state, and state 3 to longer wavelengths is also observed, consistent with sample A.

Figure 4.9(d) plots the gain spectra for sample A and sample B at room temperature at a current density of 3 kAcm^{-1} where the first excited state is saturated for both samples. Similarly to the absorption spectra shown in Fig. 4.7, InGaAs capping of the upper QD layer results in an extension in wavelength of the optical transitions. At this current density for sample A we observe the ground state (1370 nm) and first excited state (1280 nm) net modal gain of 6 cm^{-1} and 13 cm^{-1} respectively. Similarly, for the sample B ground state (1450 nm) and first excited state (1330 nm) net modal gain of 3 and 5 cm^{-1} are observed. State 3 is also observed at 1180 nm and 1250 nm for sample A and B. This peak may be a combination of both the ground state transition from the seed layer and the second excited state of the upper QD layer. Significantly, we observe a positive net modal gain above 1500 nm for the InGaAs capped (sample B) bilayer device.

4.5 Conclusions

By closely stacking two InAs/GaAs QD layers, the strain interactions between them can be exploited to provide an additional control over the growth conditions for the upper layer, allowing for a significant extension in the room temperature

emission wavelength of the QDs, up to 1400 nm for GaAs-capped QDs, at densities that are suitable for laser applications, and up to 1515 nm when an InGaAs cap is applied to the upper QD layer, with extremely low inhomogeneous broadening. When these QDs are incorporated into laser structures, ground state lasing at up to 1420 nm is achieved and ground state EL at 1515 nm with a narrow EL linewidth of 23 meV may be observed. Current dependent EL and absorption measurements indicate that the introduction of an InGaAs cap with moderate In-composition does not affect the number of optically active QDs in the devices. Under high bias conditions, the peaks in the gain spectra are asymmetrically broadened towards longer wavelengths, such that net positive modal gain beyond 1500 nm can be achieved.

4.6   Future work

As discussed the low gain and high threshold current density for InGaAs capped bilayer (longest wavelength laser) sample was attributed to a rough GaAs/AlGaAs interface. It would be interesting to repeat growth and see the limit to the QD epitaxy in terms of gain and long wavelength emission. Also it would also be interesting to compare the length dependent characteristics/gain/ modulation characteristics of undoped and p-doped GaAs capped and InGaAs capped bilayers samples.

The electroluminescence at 1515 nm (sample C) on GaAs substrate was a first ever reported; this can be readily applicable to 1550 nm mach-zehnder devices for optical switching. Also it will be interesting to apply high reflection (HR) coating to the longest possible device and see if it can lase at RT or atleast at cryostat

temperatures. There is a small gain at 1550 nm for sample C, it would be interesting to fabricate distributed feedback lasers with grating peaks around 1550 nm and observe detuned (lasing is not at the gain peak but at the longer side of gain curve) lasing at 1550 nm or another way is to do HR coating on one side (one side mirror), anti-reflection (AR) coating on the other facet, use a fiber grating with peak at 1550 nm as the other side mirror, and see if it lases at 1550nm when sufficient current is injected.

It would be interesting to look at the spin coherence mechanisms where electrons are transferred between two QDs in a bilayer. This has potential for quantum information processing applications where electrons stored in QDs are candidate systems for quantum bits (qubits).

Also it will be very interesting to look at lasing mode packet width of the lasers, which will enable the applicability of lasers for long distance optical communication.

Its has been previously shown [4.32] that stacking multiple layer increases the quantum dot size and volume of the upper layer QDs, it would be interesting to stack three layers QDs instead of bilayer which may increase the gain/modulation speed and decreases the transparency current density. Last but not the least it would also be very interesting to incorporate bilayer QDs in high carrier confining DWELL structure which may increase the gain, improve characteristics temperature, transparency current density and modulation bandwidth.

References

[4.1]   M. Asada, Y. Miyamoto, and Y. Suematsu, "Gain and the threshold of three-dimensional quantum-box lasers," *IEEE J. Quantum Electron*., vol. 22, no. 9, pp. 1915–1921, 1986.

[4.2]   Y. Arakawa and H. Sakaki, "Multidimensional quantum well laser and temperature dependence of its threshold current," *Appl. Phys. Lett*., vol. 40, no. 11, pp. 939–940, 1982.

[4.3]   S. Ghosh, S. Pradhan, and P. Bhattacharya, "Dynamic characteristics of high-speed $In_{0.4}Ga_{0.6}As$/GaAs self-organized quantum dot lasers at room temperature," *Appl. Phys. Lett*., vol. 81, pp. 3055–3057, 2002.

[4.4]   T. C. Newell, D. J. Bossert, A. Stintz, B. Fuchs, K. J. Malloy, and L. F. Lester, "Gain and linewidth enhancement factor in InAs quantum dot laser diodes," *IEEE Photon. Technol. Lett*., vol. 11, no. 12, pp. 1527 - 1529, 1999.

[4.5]   D. J. Eaglesham, and M. Cerullo, "Dislocation-free Stranski-Krastanow growth of Ge on Si(100)," *Phys. Rev. Lett.,* vol. 64, no. 16, pp. 1943-1946, 1990.

[4.6]   S. Guha, A. Madhukar, and K. C. Rajkumar, "Onset of incoherency and defect introduction in the initial stages of molecular beam epitaxial growth of highly strained $In_xGa_{1-x}As$ on GaAs(100)," *Appl. Phys. Lett*., vol. 57, no. 20, pp. 2110-2112, 1990.

[4.7]   D. L. Huffaker and D. G. Deppe, "Electroluminescence efficiency of 1.3 μm wavelength InGaAs/GaAs quantum dots," *Appl. Phys. Lett*., vol. 73, no. 4, pp. 520-522, 1998.

[4.8]   A. Salhi, L. Fortunato, L. Martiradonna, M. T. Todaro, R. Cingolani, A. Passaseo and M. De Vittorio, "High efficiency and high modal gain InAs/InGaAs/GaAs quantum dot lasers emitting at 1300 nm," *Semicond. Sci. Technol.*, vol. 22, pp. 396–398, 2007.

[4.9]   L. H. Li, M. Rossetti, A. Fiore and G. Patriarche, "1.43 µm InAs bilayer quantum dot lasers on GaAs substrate," *Electron. Lett.*, vol. 42, no. 11, pp. 638-639, 2006.

[4.10]   N. N. Ledentsov, A. R. Kovsh, A. E. Zhukov, N. A. Maleev, S. S. Mikhrin, A. P. Vasil'ev, E. S. Semenova, M. V. Maximov, Y. M. Shernyakov,N. V. Kryzhanovskaya, V. M. Ustinov, and D. Bimberg, "High performance quantum dot laser on GaAs substrates operating in 1.5 µm range," *Electron. Lett.*, vol. 39, no. 15, pp. 1126-1128, 2003.

[4.11]   Z. Y. Zhang , Z. G. Wang , B. Xu , P. Jin , Z. Z. Sun and F. Q. Liu   "High-performance quantum-dot superluminescent diodes," *IEEE Photon. Tech. Lett.*, vol. 16, no.1, pp. 27-29, 2004.

[4.12]   P. D. L. Greenwood, D. T. D. Childs, K. M. Groom, B.J. Stevens, M. Hopkinson and R. A. Hogg, "Tuning superluminescent diode characteristics for optical coherence tomography systems by utilising a multi-contact device Incorporating wavelength modulated quantum dots," *IEEE J. Sel. Topics Quantum Electron.*, vol. 15, no. 3, pp. 757-763, 2009.

[4.13]   E. U. Rafailov, M. A. Cataluna, and W. Sibbett, "Mode-locked quantum-dot lasers," *Nature Photonics*, vol. 1, pp. 395-401, 2007.

[4.14] E. U. Rafailov, S. J. White, A. A. Lagatsky, A. Miller, W. Sibbett, D. A. Livshits, A. E. Zhukov, and V. M. Ustinov, "Fast quantum-dot saturable absorber for passive mode-locking of solid-state lasers," *IEEE Photon. Technol. Lett.,* vol. 16, no. 11, pp. 2439-2441, 2004.

[4.15] M. P. Lumb, E. Clarke, E. Harbord, P. Spencer, R. Murray, F. Masia, P. Borri, W. Langbein, C. G. Leburn, C. Jappy, N. K. Metzger, C. T. A. Brown, and W. Sibbett, "Ultrafast absorption recovery dynamics of 1300 nm quantum dot saturable absorber mirrors," *Appl. Phys. Lett*., vol. 95, no. 4, pp. 041101-041101-3, 2009.

[4.16] K. Asakawa, Y. Sugimoto, Y. Watanabe, N. Ozaki, A. Mizutani, Y. Takata, Y. Kitagawa, H. Ishikawa, N. Ikeda, K. Awazu, X. Wang, A. Watanabe, S. Nakamura, S. Ohkouchi, K. Inoue, M. Kristensen, O. Sigmund, P. I. Borel, and R. Baetys, "Photonic crystal and quantum dot technologies for all-optical switch and logic device," *New J. Phys*., vol. 8, pp. 208-208-26, 2006.

[4.17] D. L. Huffaker, G. Park, Z. Zou, O. B. Shchekin, and D. G. Deppe, "1.3 μm room-temperature GaAs-based quantum-dot laser," *Appl. Phys. Lett*., vol. 73, no. 18, pp. 2564-2566, 1998.

[4.18] F. Lelarge, B. Dagens, J. Renaudier, R. Brenot, A. Accard, F. van Dijk, D. Make, O. Le Gouezigou, J. G. Provost, F. Poingt, J. Landreau, O. Drisse, E. Derouin, B. Rousseau, F. Pommereau, and G. H. Duan, "Recent advances on InAs/InP quantum dash based semiconductor lasers and optical amplifiers operating at 1.55 μm", *IEEE J. Sel. Topics Quantum Electron*., vol. 13, no. 1, pp. 111-124, 2007.

[4.19]   P. J. Poole, K. Kaminska, P. Barrios, Z. Lu, and J. Liu, "Growth of InAs/InP-based quantum dots for 1.55 µm laser applications", *J. Crystal Growth*, vol. 311, pp. 1482-1486, 2009.

[4.20]   R. Murray, D. Childs, S. Malik, P. Siverns, C. Roberts, J. M. Hartmann, and P. Stavrinou, "1.3µm Room Temperature Emission from InAs/GaAs Self-Assembled Quantum Dots," *Jpn. J. Appl. Phys.*, vol. 38, pp. 528-530, 1999.

[4.21]   R. P. Mirin, J. P. Ibbetson, K. Nishi, A. C. Gossard, and J. E. Bowers, "1.3 µm photoluminescence from InGaAs quantum dots on GaAs," *Appl. Phys. Lett.*, vol. 67, no. 25, pp. 3795-3797, 1995.

[4.22]   K. Nishi, H. Saito, S. Sugou, and J. S. Lee, "A narrow photoluminescence linewidth of 21 meV at 1.35 µm from strain-reduced InAs quantum dots covered by $In_{0.2}Ga_{0.8}As$ grown on GaAs substrates," *Appl. Phys. Lett.*, vol. 74, no. 8, pp. 1111-1113, 1999.

[4.23]   V. M. Ustinov, N. A. Maleev, A. E. Zhukov, A. R. Kovsh, A. Y. Egorov, A. V. Lunev, B. V. Volovik, I. L. Krestnikov, Y. O. Musikhin, N. A. Bert, P. S. Kop'ev, Z. I. Alferov, N. N. Ledentsov, and D. Bimberg, "InAs/InGaAs quantum dot structures on GaAs substrates emitting at 1.3 µm," *Appl. Phys. Lett.*, vol. 74, no. 19, pp. 2815-2817, 1999.

[4.24]   P. B. Joyce, T. J. Krzyzewski, G. R. Bell, T. S. Jones, S. Malik, D. Childs, and R. Murray, "Effect of growth rate on the size, composition, and optical properties of InAs/GaAs quantum dots grown by molecular-beam epitaxy," *Phys. Rev. B*, vol. 62, no. 6, pp. 10891-10895, 2000.

[4.25] P. B. Joyce, T. J. Krzyzewski, G. R. Bell, T. S. Jones, E. C. Le Ru, and R. Murray, "Optimizing the growth of 1.3 µm InAs/GaAs quantum dots," *Phys. Rev. B*, vol. 64, no. 23, pp. 235317-235327-6, 2001.

[4.26] B. Alloing, C. Zinoni, V. Zwiller, L. H. Li, C. Monat, M. Gobet, G. Buchs, A. Fiore, E. Pelucchi, and E. Kapon, "Growth and characterization of single quantum dots emitting at 1300 nm," *Appl. Phys. Lett*., vol. 86, no. 10, pp. 101908-101908-3, 2005.

[4.27] L. Seravalli, M. Minelli, P. Frigeri, S. Franchi, G. Guizzetti, M. Patrini, T. Ciabattoni, and M. Geddo, "Quantum dot strain engineering of InAs/InGaAs nanostructures," *J. Appl. Phys.*, vol. 101, no. 2, pp. 024313-024313-8, 2007.

[4.28] J. Tatebayashi, M. Nishioka, and Y. Arakawa, "Over 1.5 µm light emission from InAs quantum dots embedded in InGaAs strain-reducing layer grown by metal organic chemical vapor deposition," *Appl. Phys. Lett.*, vol. 78, no. 22, pp. 3469-3471, 2001.

[4.29] T. P. Hsieh, P. C. Chiu, J. I. Chyi, N. T. Yeh, W. J. Ho, W. H. Chang, and T. M. Hsu, "1.55 µm emission from InAs quantum dots grown on GaAs," *Appl. Phys. Lett*., vol. 87, no. 15, pp. 151903-151903-3, 2005.

[4.30] M. Richter, B. Damilano, J. Y. Duboz, J. Massies, and A. D. Wieck, "Long wavelength emitting InAs/Ga$_{0.85}$In$_{0.15}$N$_x$As$_{1-x}$ quantum dots on GaAs substrate," *Appl. Phys. Lett.*, vol. 88, pp. 231902-231902-3, 2006.

[4.31] D. Guimard, S. Tsukamoto, M. Nishioka, and Y. Arakawa, "1.55 µm emission from InAs/GaAs quantum dots grown by metal organic chemical vapor

deposition via antimony incorporation," *Appl. Phys. Lett.*, vol. 89, no. 8, pp. 083116-083116-3, 2006.

[4.32] Q. Xie, A. Madhukar, P. Chen, and N. P. Kobayashi, "Vertically self-organized InAs quantum box islands on GaAs(100)," *Phys. Rev. Lett.,* vol. 75, no. 13, pp. 2542-2545, 1995.

[4.33] P. Howe, E. C. Le. Ru, E. Clarke, B. Abbey, R. Murray, and T. S. Jones, "Competition between strain-induced and temperature-controlled nucleation of InAs/GaAs quantum dots," *J. Appl. Phys.*, vol. 95, no. 6, pp. 2998-3004, 2004.

[4.34] E. C. Le Ru, P. Howe, T. S. Jones, and R. Murray, "Strain-engineered InAs/GaAs quantum dots for long-wavelength emission," *Phys. Rev. B*, vol. 67, no. 16, pp.165303-165303-5, 2003.

[4.35] E. Clarke, P. Howe, M. Taylor, P. Spencer, E. Harbord, R. Murray, S. Kahkhodazadeh, D. W. McComb, B. J. Stevens, and R. A. Hogg, "Persistent template effect in InAs/GaAs quantum dot bilayers", *J. Appl. Phys.*, vol. 107, no. 11, pp. 113502-113502-6, 2010.

[4.36] E. Clarke, P. Spencer, E. Harbord, P. Howe, and R. Murray, "Growth, optical properties and device characterisation of InAs/GaAs quantum dot bilayers," *J. Phys.: Conf. Series*, vol. 107, pp. 012003-012003-10, 2008.

[4.37] O. G. Schmidt and K. Eberl, "Multiple layers of self-asssembled Ge/Si islands: Photoluminescence, strain fields, material interdiffusion, and island formation," *Phys. Rev. B*, vol. 61, pp. 13721-13729, 2000.

[4.38] M. O. Lipinski , H. Schuler , O. G. Schmidt , K. Eberl and N. Y. Jin-Phillipp, "Strain-induced material intermixing of InAs quantum dots in GaAs," *Appl. Phys. Lett.*, vol. 77, no. 12, pp. 1789-1791, 2000.

[4.39] I. Mukhametzhanov, R. Heitz, J. Zeng, P. Chen, and A. Madhukar, "Independent manipulation of density and size of stress-driven self-assembled quantum dots," *Appl. Phys. Lett.*, vol. 73, pp. 1841-1843, 1998.

[4.40] J. S. Wang, S. H. Yu, Y. R. Lin, H. H. Lin, C. S. Yang, T. T. Chen, Y. F. Chen, G. W. Shu, J. L. Shen, R. S. Hsiao, J. F. Chen, and J. Y. Chi, "Optical and Structural Properties of Vertically Stacked and Electronically Coupled Quantum Dots in InAs/GaAs Multilayer Structures," *Nanotechnology*, vol. 8, no.1 pp. 015401-015401-5, 2007.

[4.41] W. M. McGee, T. J. Krzyzewski, and T. S. Jones, "Atomic scale structure and morphology of (In, Ga) As-capped InAs quantum dots*," J. Appl. Phys.*, vol. 99, pp. 043505-043505-6, 2006.

[4.42] E. C. Le Ru, A. J. Bennett, C. Roberts, and R. Murry, "Strain and electronic interactions in InAs/GaAs quantum dot multilayers for 1300 nm emission," *J. Appl. Phys.*, vol. 91, no.3, pp. 1365-1369, 2002.

[4.43] R. Heitz, I. Mukhametzhanov, P. Chen, A. Madhukar, "Excitation relaxation in self-organized asymmetric quantum dot pairs," *Phys. Rev. B*, vol. 58, pp. R10151-10154, Oct. 1998.

[4.44] Z. Mi and P. Bhattacharya, "Molecular-beam epitaxial growth and characteristics of highly uniform InAs/GaAs quantum dot layers," *J. Appl. Phys.*, vol. 98, pp. 023510-023510-5, 2005.

[4.45] L. V. Asryan and R. A. Suris. "Inhomogeneous line broadening and the threshold current density of a semiconductor quantum dot laser," *Semicond. Sci. Technol.*, vol. 11, no. 4, pp. 554-567, 1996.

[4.46] L. V. Asryan and R. A. Suris, "Upper limit for the modulation bandwidth of a quantum dot laser," *Appl. Phys. Lett*., vol. 96, no. 22, pp. 221112-221112-3, 2010.

[4.47] P. Howe, E. C. Le Ru, E. Clarke, R. Murray, and T. S. Jones, "Quantification of segregation and strain effects in InAs/GaAs quantum dot growth," *J. Appl. Phys*., vol. 98, no. 11, pp. 113511-113511-5, 2005.

[4.48] P. Blood, G. M. Lewis, P. M. Smowton, H. D. Summers, J. D. Thomson and J. Lutti, "Characterization of Semiconductor Laser gain Media by the Segmented Contact Method," *IEEE J. Sel. Topics Quantum Electron*., vol. 9, no. 5, pp.1275-1282, 2003.

[4.49] H. C. Schneider, W. W. Chow, S. W. Koch, "Many-body effects in the gain spectra of highly excited quantum-dot lasers," *Phys. Rev. B*, vol. 64, no. 11, pp. 115315-115315-7, 2001.

[4.50] Y. C. Xin, Y. Li, A. Martinez, T. J. Rotter, H. Su, L. Zhang, A. L. Gray, S. Luong, K. Sun, Z. Zou, J. Zilko, P. M. Varangis, and L. F. Lester, "Optical gain and absorption of quantum dots measured using an alternative segmented contact method," *IEEE J. Quantum Electron*., vol. 42, no. 7, pp. 725-732, 2006.

[4.51] I. O'Driscoll, M. Hutchings, P. M. Smowton, P. Blood, "Many-body effects in InAs/GaAs quantum dot laser structures," *Appl. Phys. Lett*., vol. 97, pp.141102-141102-3, 2010.

[4.52] S. V. Nair and Y. Masumoto, "Multi-exciton states in semiconductor quantum dots". *Phys. Stat. Sol*. (a), vol. 178, pp. 303-306, 2000.

Chapter 5

O-band Excited State Quantum Dot Bilayer Lasers

5.1   Introduction

Semiconductor diode lasers incorporating self-assembled quantum dots on GaAs substrates accessing the International Telecommunication Union (ITU) O-band (1260 nm-1360 nm) have received considerable attention, to the point of their current commercialization [5.1, 5.2] with recent performance milestones reached including high-speed, temperature-insensitive [5.3] operation around room-temperature at 1300 nm through the use of p-type doping [5.4]. In contrast to quantum well (QW) lasers, the modulation dynamics of QD lasers are limited by damping due to comparatively low saturated gain and slow (few ps) carrier dynamics [5.5], and in order to achieve high modulation rates, low carrier scattering times (< 1ps) into the lasing state and high saturated modal gains are required. Possible routes to increase saturated gain include careful optimization of growth conditions to increase QD areal density [5.6] or to increase differential gain by increasing p-doping, but this has practical limits in terms of additional loss [5.7]. Tunnel injection from a QW into higher energy QD states has been shown to reduce the capture or carrier scattering time [5.4, 5.8]. However, these structures are problematic as it needs a QW close to lasing wavelength and it is unclear whether lasing from this QW is suppressed at higher current densities.

It has recently been demonstrated that operation using the excited state (ES) of the QDs exhibit much higher damping limited bandwidths as compared to ground state (GS) lasers [5.8-5.11]. This enhancement was attributed to higher saturated gain (double) and lower scattering time (half) compared to the ground state. However this is achieved at the expense of higher operating currents and shorter operating wavelengths that may be impractical for fiber-optic based optical communications applications.

Here I demonstrate that the technologies to realize long wavelength QD ground state emission can be applied to realize QD excited state emission spanning the O-band. In this chapter I report on the fabrication of QD bilayer (repeated briefly for the sake of convenience) [5.12, 5.13] materials where excited state lasing is demonstrated between 1260-1330 nm, spanning the ITU O-band. This is achieved by using QD material comprising of closely-stacked layers of QDs which are strain and electronically coupled, consisting of a seed layer which determines the areal density and an upper emission layer. The wavelength coverage is made possible by utilizing both GaAs and InGaAs capping of the emission layer. Measurement of multi-section lasers containing these QD bilayers allows the peak modal gain of the excited state as a function of current density to be deduced [5.14] as described in the last chapter, and this is comparable to commercially available 1300 nm QD laser samples operating in the GS. Lastly, I will discuss the effect of carrier transport time on modulation bandwidth and the advantage of an excited state QD laser, using a two state model after Ishida *et al.* [5.5].

_____

5.2   Experimental

In the last chapters the growth of bilayer has been described in detail. Here I repeat the growth details in brief for the sake of convenience and consistency. The samples were p-i-n edge-emitting laser structures grown on n^+ GaAs (100) substrates by molecular beam epitaxy. As before the active region for the structures was located in a 500 nm undoped GaAs layer sandwiched between 1500 nm $Al_{0.33}Ga_{0.67}As$ doped cladding layers, with a 400 nm p-type GaAs:Be contact layer completing the structure.

The active region consisted of five GaAs-capped or $In_{0.18}Ga_{0.82}As$ (4 nm) capped QD bilayers (see Fig. 5.1). These samples referred as the "GaAs-capped bilayer" or "InGaAs-capped bilayer" sample in the following. Each bilayer consists of two closely-spaced InAs/GaAs QD layers: a seed layer and an upper emission layer. Strain fields from the underlying QDs in the seed layer penetrate the thin GaAs spacer layer (10 nm between QD layers), providing preferential nucleation sites for QDs in the second layer. This leads to a high degree of vertical correlation between QDs in the two layers (as observed in the transmission electron microscopy (TEM) images in Fig. 5.1),[5.15] such that the seed layer acts as a template for growth in the second layer, fixing the QD density in this layer over a wide range of growth conditions. For these samples, the QD density in each layer was 2.7×10^{10} cm^{-2}.

Figure 5.2, shows normalized photoluminescence (PL) spectra from GaAs- and InGaAs-capped bilayer test samples at room temperature. Emission at 1340 nm (1420 nm) and 1260 nm (1330 nm) for the GaAs-capped (InGaAs-capped) samples is attributed to emission from the ensemble of ground states and excited states of
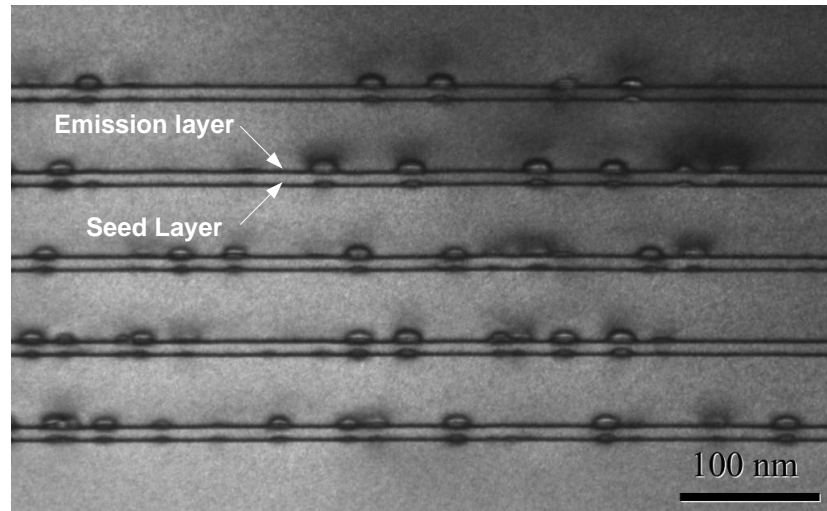
_____

Fig. 5.1. Dark field (002) cross-sectional TEM images obtained from a GaAs-capped QD bilayer. TEM measurements provided by Integrity Scientific (www.integrityscientific.com).
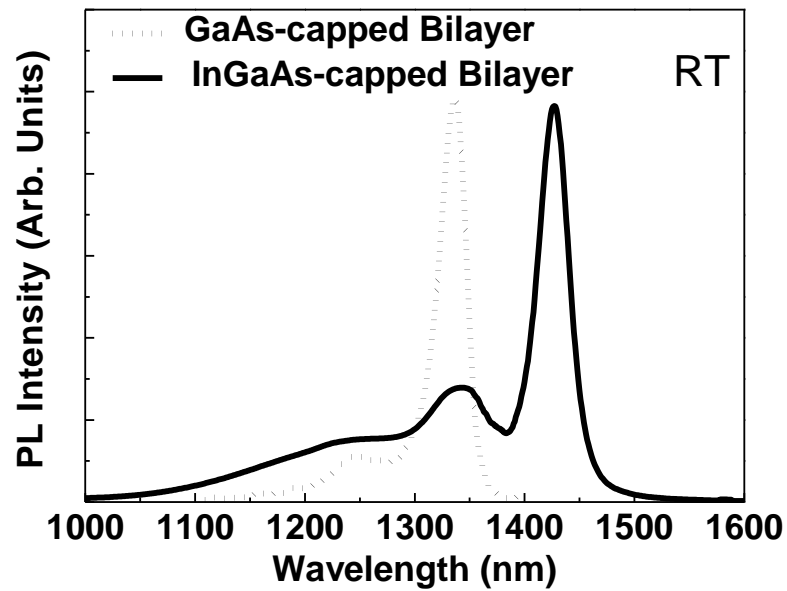

Fig. 5.2. Room temperature PL spectra obtained from GaAs and InGaAs capped QD bilayer test samples.

the QDs, respectively [5.13]. The linewidth of GS emission wavelength is only 15

meV at room temperature for both the samples, which is comparable to the lowest

PL linewidth reported for any QD ensemble [5.16]. This is attractive for device

applications, with low inhomogeneous broadening expected to benefits for the

peak gain, threshold current and modulation bandwidth of QD lasers [5.17].

Figure 5.3, is partly repeated here from the last chapter for the sake of convenience

and completeness, in terms of assignment of GS and ES and to compare with PL

results discussed above. Figure 5.3(a) shows edge-emission room temperature

electroluminescence (EL) spectra with increasing current density (70-350 A/cm^2),

obtained from a device fabricated from GaAs-capped bilayer sample where lasing is

inhibited (device length 1 mm). Figure 5.3(b) shows EL spectra obtained under

similar conditions from the InGaAs-capped bilayer sample. The saturation of long

wavelength features in both the samples confirms the assignment of ES emission at

1260 nm and 1330 nm for GaAs- and InGaAs-capped samples respectively. The

Figure 5.3(c) shows EL lasing spectra obtained from other devices fabricated from

the GaAs-capped bilayer and the InGaAs-capped bilayer sample, respectively, at

bias levels of 1.2 times the laser threshold current (J_{th}) for each device. Both

devices exhibit lasing in the ground state, at a wavelength of 1340 nm with J_{th} = 83

A/cm^2 for GaAs-capped bilayer (with a device length of 2 mm) and a wavelength of

1420 nm with J_{th} = 550 A/cm^2 for InGaAs-capped bilayer (with a device length of 8.7

mm). Again as explained earlier in last chapter, the increased device length

required to achieve GS lasing (and increased J_{th}) for the InGaAs-capped bilayer is a

result of increased optical losses due to an increase in the roughness of one of the

GaAs/AlGaAs interfaces in this sample, observed by TEM (Fig. 4.6 last chapter).
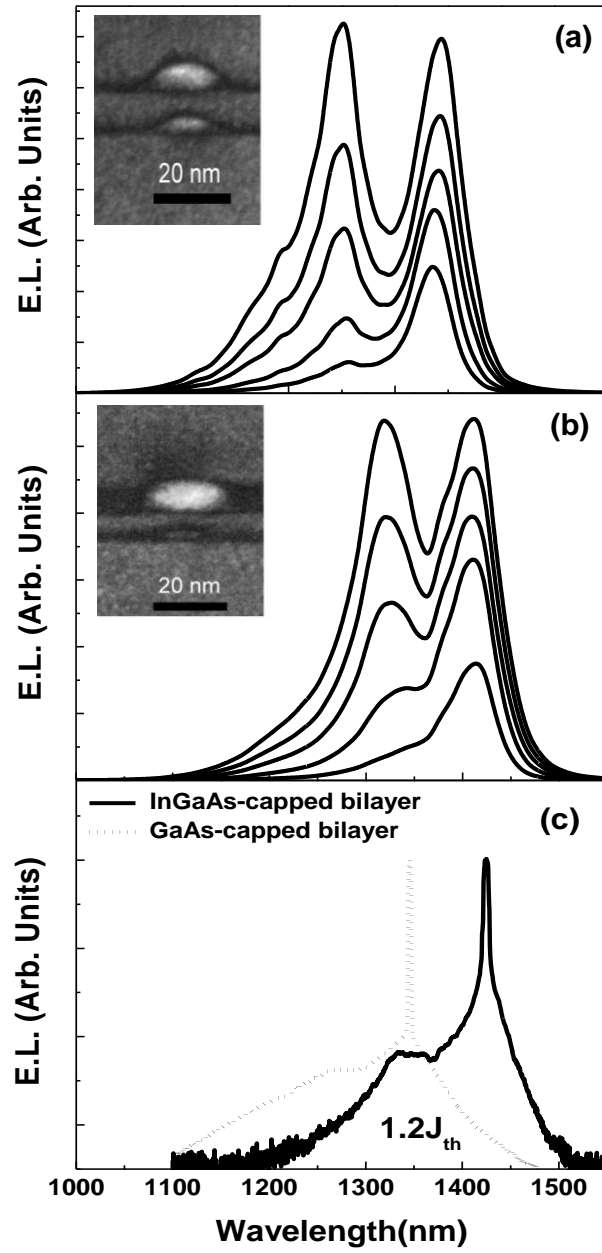
Fig. 5.3. (a) Room temperature EL spectra obtained over a range of current density (70-350 A/cm^2) for GaAs-capped bilayer, Inset: Dark field (002) cross-sectional TEM images and (b) InGaAs-capped bilayer samples, Inset: Dark field (002) cross-sectional TEM images (c) Lasing spectra at 1.2J$_{th}$ obtained from 2 mm GaAs-capped and 8.7 mm InGaAs-capped bilayer lasers. Inset: room temperature PL spectra obtained from individual GaAs-capped or InGaAs-capped QD bilayers.

_____

There is an extension of the GS and ES emission compared to GaAs-capped bilayer sample to 1420 nm and 1330 nm respectively, which is due to the preservation of the QD size and composition and also the strain reduction provided by the InGaAs capping layer. It is noted that there is the suppression of emission from the seed layer at ~1200 nm and a small peak at this wavelength is only observed at high bias for GaAs-capped bilayer sample indicating efficient electronic coupling between the QD layers in each bilayer (see inset of Fig. 5.3 and Fig. 5.1).

Figure 5.4(a) shows typical optical power-current characteristics of a 1 mm long ridge laser device fabricated from GaAs-capped bilayer sample, measuring the total output power from both as-cleaved facets using pulsed excitation with a pulse duration of 5 μs and a 1% duty cycle to minimize heating. The laser exhibits excited state lasing at 1260 nm with a threshold current density (J_{th}) of 650 Acm^{-2} and a slope efficiency of 0.25 W/A. The inset shows the lasing spectra at 1.2 times J_{th}. Figure 5.4(b) shows power-current characteristics of a 6 mm long ridge laser device fabricated from the InGaAs-capped bilayer sample, using the same measurement conditions as for GaAs-capped bilayer. The laser exhibits excited state lasing at 1330 nm, but with a higher J_{th} of 1400 Acm^{-2} and a reduced slope efficiency of 0.07 W/A. The lasing wavelengths for both the samples match the excited state EL peaks observed in Fig. 5.3 and PL peaks in Fig. 5.2, and are at a longer wavelength than the seed layer emission (1200 nm), indicating that lasing is occurring in the ES of the upper layer QDs. The increased device length required to achieve excited state lasing (and corresponding increase in J_{th}) and the decrease in slope efficiency for

_____

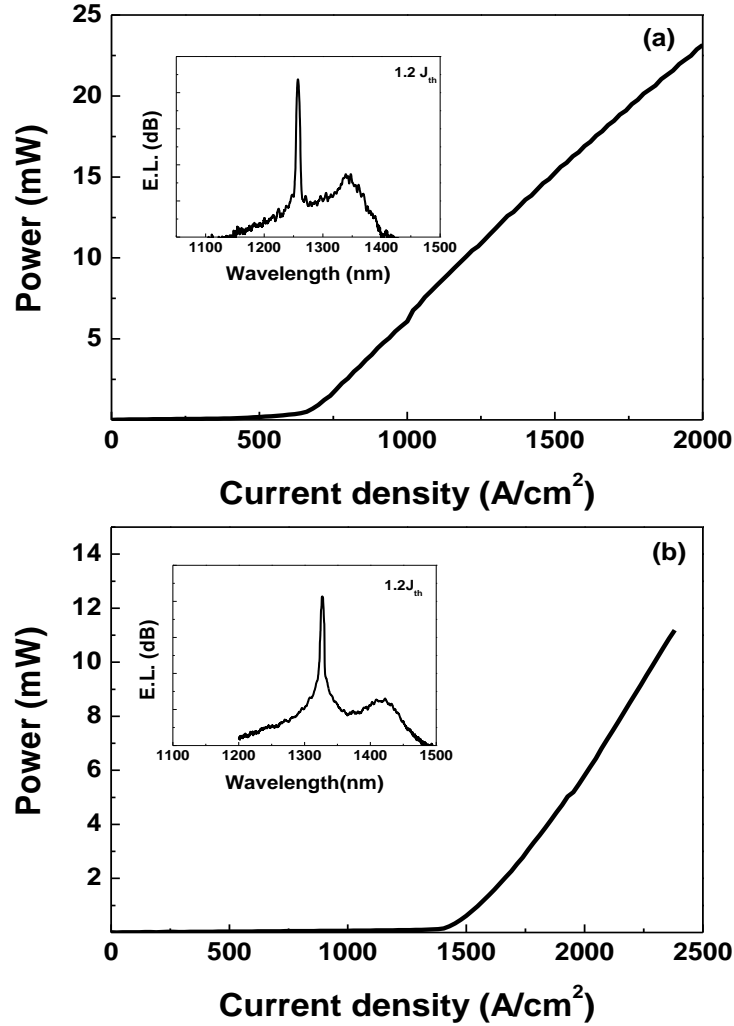InGaAs-capped bilayer laser is attributed to the increased optical losses in this sample.

Fig. 5.4 (a) Total optical power (from both as-cleaved facets) as a function of current density from a 1 mm-long broad area laser fabricated from GaAs-capped bilayer sample. Inset: room temperature lasing spectrum obtained at a current injection of 1.2 x threshold current density (J_{th}). (b) Total optical power as a function of current density from a 6 mm-long broad area laser fabricated from InGaAs-capped bilayer sample. Inset: room temperature lasing spectrum obtained at 1.2 x J_{th}.

Using multi-section devices [5.18], the gain spectrum may be determined as a function of current density [5.14]. Absorption measurements and analysis of gain spectra at long wavelengths indicate an internal loss of 3 ± 1 cm^{-1} for GaAs capped

_____

and 5±1 cm^{-1} for the InGaAs capped sample (last chapter Figs. 4.8 and 4.10). These

values for internal loss are combined with net modal gain values to plot the peak

modal gain per dot of the ES for both samples as a function of current density in
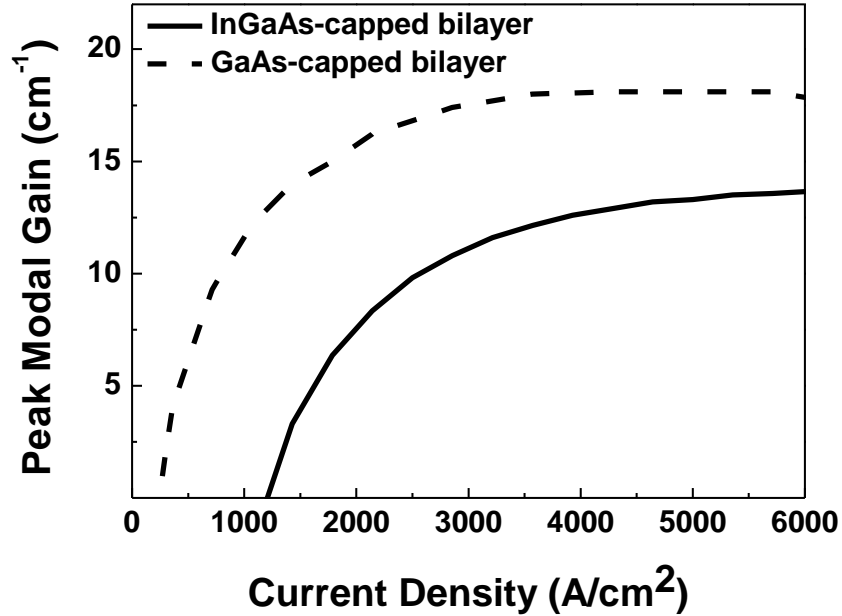
Fig. 5.5 [5.19].

Fig.5.5. Peak excited state modal gain for GaAs-capped and InGaAs-capped bilayer
structures obtained by multi-section gain measurements

This value is an important parameter in determining the damping limited

modulation bandwidth [5.5, 5.20]. The saturated modal gain for the GaAs- and

InGaAs-capped bilayer samples are determined to be 18 and 12 cm^{-1}, respectively.

The modal gain per QD of the GS and ES of the GaAs capped sample compares very

favorably with commercially-sourced QD laser samples operating at 1280 nm,

which have also been processed into multi-section devices. The commercially-

sourced material has four times the number of QDs (double dot density) in the

active region (twice the number of QD layers, each with double the QD density in

_____

each layer) but also has around double the inhomogeneous line-width, and exhibits

an ES modal gain of ~40 cm^{-1} at 1200 nm [5.9]. This represents only a ~2 times

increase in modal gain compared to the bilayer QD lasers considered here. This

difference is attributed to the smaller inhomogeneous linewidth for the bilayer QD

devices [5.21]. An increase in the areal QD density in the bilayers, achievable by

tuning the growth conditions of the seed layer, can be expected to further enhance

the ES saturated gain [5.22].

To understand the effect of saturated gain (GS and ES), scattering time and carrier

transport effect [5.23], on modulation bandwidth, a single model of the dynamics

occurring in the QD lasers is presented (Fig. 5.6) by a two state model after Ishida

et al. [5.5], which forms the basis of the rate equation which are solved to give the

k-factor limited modulation bandwidth.
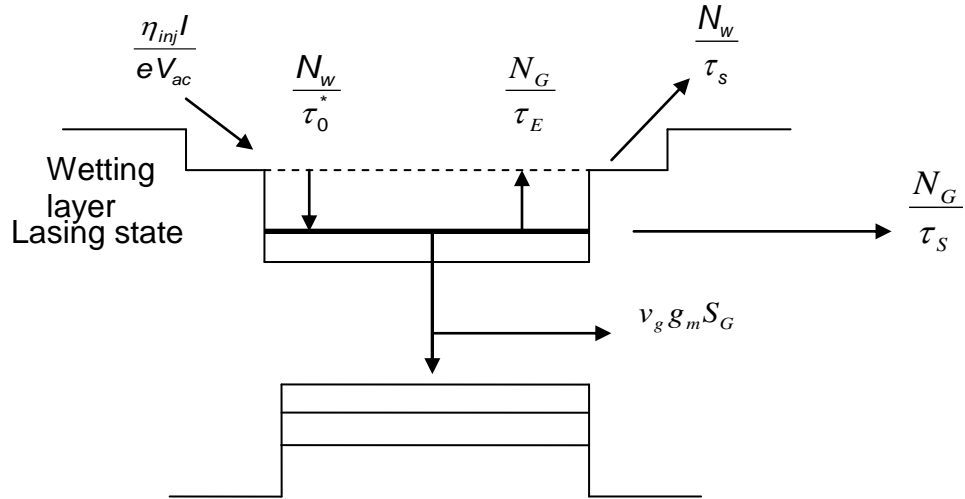

Fig. 5.6. Schematic of the model after Ishida *et al.* [5.5]

In this simplified model initially the electrical carriers are injected into the wetting

layer (reservoir), where the carrier may either; relax to lasing state (non-lasing

states are ignored), or be lost from the wetting layer to spontaneous emission. The carriers in lasing state can either; be lost via non-radiative or radiative recombination, be scatter from the lasing state to the wetting layer and be excited out of the wetting layer. By finding the steady state solution of the rate equation given by the model, it has been shown that the k-factor limited modulation bandwidth may be given by [5.5]:

$$f_{3dB\max} = \frac{\sqrt{2}}{2\pi\left[\left(\frac{1}{v_g\alpha_c}\right)+\left(\frac{\tau_0}{1-\frac{1}{2}\left(1+\frac{\alpha_c}{G_{\max}}\right)}\right)\right]} \tag{1}$$

As can be seen from equation 1, the maximum modulation is dependent on the group velocity in the waveguide (v_g), total cavity loss ($\alpha_{c=}$ α_{i+} α_m), maximum saturated modal gain of the lasing state ($G_{\max}$) and τ_0 (the scattering time from the reservoir into the lasing state). The values of saturated gain and internal loss are known from multi-section or length dependant measurements. The group velocity can be easily calculated from refractive index of GaAs of ~3.5. The scattering time τ_0, then becomes the only fitting parameter. The scattering time is assumed to be ~3ps for this model based on the previous work [5.5, 5.7] for conventional 1.3 μm QD laser materials. From these values k-factor limited bandwidth can be optimized by altering the mirror loss.

Figure 5.7, plots the K-factor limited bandwidth as a function of the cavity loss for a fixed $G_{\max}$ and increasing τ_0. It is clearly seen that as τ_0 decreases the k-factor limited bandwidth increases to peak and started to roll-off with increase in cavity loss.
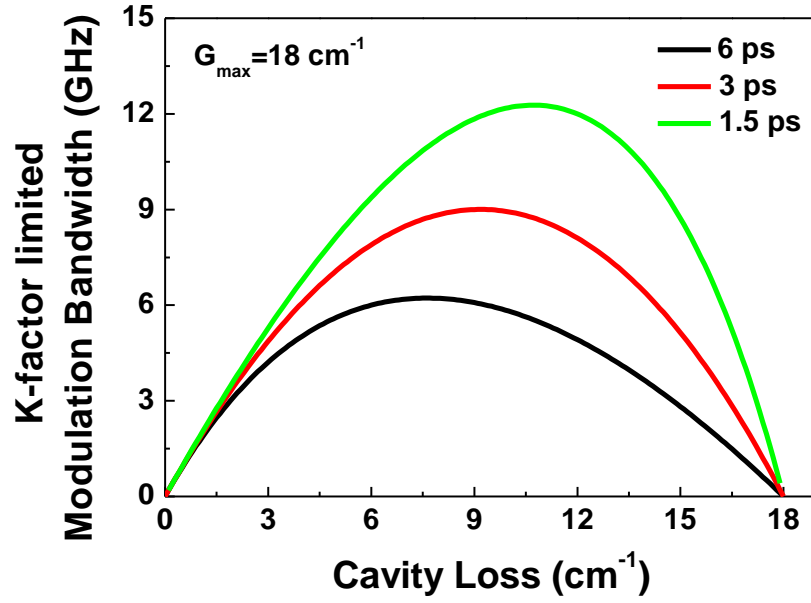
Fig. 5.7. k-factor limited bandwidth as a function of cavity loss for a fixed G_{max} (18 cm^{-1}) and increasing scattering time τ_0.

Fig. 5.8. K-factor limited band bandwidth as a function of cavity loss for fixed scattering time τ_0 (3 ps) and increasing G_{max}.

Figure 5.8, similarly plots the k-factor limited bandwidth as a function of cavity loss for fixed τ_0 and increasing G_{max}. It is clearly seen that as the maximum saturated gain increases the k-factor limited bandwidth increases and as before the cavity

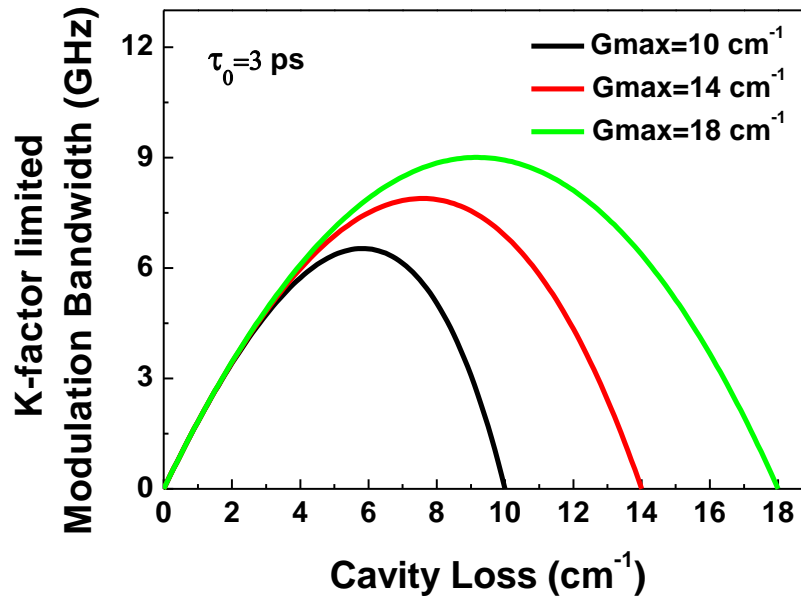loss at which it occurs moves to higher value. It can be concluded from the last two figures that for a laser of fixed dimensions and optimised cavity reflectivity the net effect of increasing the maximum modal gain or reducing the scattering time to the lasing state is to increase the k-factor limited bandwidth.

Figure 5.9 shows the calculated K-factor limited modulation bandwidth as a function of scattering time to the lasing state, and the saturated gain of the lasing state. A typical method to enhance the maximum modulation bandwidth is to include more QD layers within the active region.
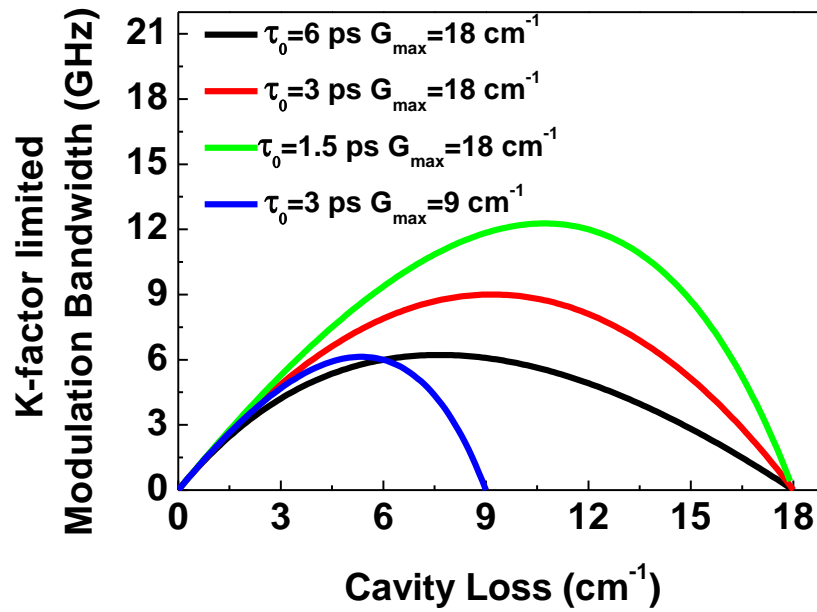

Fig. 5.9. K-factor limited modulation bandwidth as a function of cavity loss for fixed G_{max} of 9 and 18 cm^{-1}.

τ_0 (ps)	G_{max} (cm^{-1})	K_{max} (GHz)
1.5	18	12.3
3	18	9.0
3	9	6.2
6	18	6.2

Table. 5.1. Data extracted from Fig. 9

A calculated increase in maximum K-factor limited bandwidth is observed for $\tau_0 = 3$ ps and increasing G_{sat} from e.g. 9 cm^{-1} to 18 cm^{-1}. However, it has been shown that carrier transport effects become significant for large numbers of QD layers (i.e. thick active elements) [24]. The carrier transport time may be included as an effective increase in scattering time to the lasing state in the rate equation model [23] with carrier transport times rising from ~1 ps to ~4 ps for 5 and 10 QD layers respectively [24]. The impact of increased transport times on maximum modulation bandwidth is observed by comparing the curve for $G_{sat} = 18$ cm^{-1} and $\tau_0 = 6$ ps, with that for the same saturated gain, $G_{sat} = 18$ cm^{-1}, and the expected $\tau_0 = 3$ ps (also see Table.5.1). These cases illustrate the effect of doubling saturated gain at the expense of significant transport times, suggesting that essentially the same maximum modulation bandwidth would be obtained. Experimentally, a reduction in maximum modulation bandwidth has been observed for a 10 QD layer laser compared to a 5 QD layer laser due to this carrier transport effect [24]. The advantage of an excited state laser is that the net modal gain is increased without increasing the QD layer number. Indeed, the scattering time is expected to be reduced [9] due to the higher density of final scattering states, leading to an increase in the predicted K-factor limited bandwidth (see Fig. 5.9, $G_{sat} = 18$ cm^{-1}, $\tau_0 = 3$ ps, $G_{sat} = 18$ cm^{-1}, $\tau_0 = 1.5$ ps).

_____

5.3   Conclusions

In summary, excited state QD lasers spanning the O-band is made possible using either GaAs and InGaAs capped bilayer structures. Room-temperature lasing from either the GS or ES is observed, depending on cavity length, for a range of wavelengths from 1340-1420 nm from the GS or 1260-1330 nm for the ES. The saturated peak modal gain per QD from these devices is comparable to commercially available 1300 nm QD lasers operating in the GS, but the reduced number of QD layers required for ES lasing and in the increased degeneracy of states is expected to lead to an increase in the K-factor limited bandwidth for these devices.

5.4   Future Work

In the initial part of this chapter I have discussed the technologies to realize the excited state lasing covering the ITU O-band and presented results from the two state model after Ishida *et al.* [5.5]. Previous results have shown that p-doping is the key to increase differential gain and hence increased k-factor limited bandwidth [5.4, 5.7, 5.11]. As the use of bilayers is currently the only viable way except metamorphic buffer layer to achieve the GS lasing in excess of 1400 nm and achieve ES emission at the minimum in dispersion in single-mode fiber at 1310 nm. It would be interesting to fabricate p-doped and un-doped GaAs- and InGaAs-capped bilayer into ridge laser with coplanar RF contacts and to compare the k-factor limited modulation bandwidth of the GS and ES and to see what speed advantage the excited laser offers.

_____

Recently it has been shown that carrier transport effects become significant for large numbers of QD layers (i.e. thick active elements) [5.24]. It would be interesting to study the effect of carrier transport on the 3, 5, 7 bilayer QD stacking within the same/different core region. These results may present a different scenario for k-factor limited bandwidth in terms of differential gain, p-doping, maximum saturated gain (different core thickness), and relaxation time. On top of the above results InGaAs-capping may increase the confinement potential which will reduce the thermal excitation of the carrier out of the lasing state (increasing the k-factor limited bandwith).

In the previous chapter I have demonstrated the GS electroluminescence at 1515 nm, and second excited state around 1300 nm. This offers an exciting possibility of modulating second excited state lasers with increased gain. It would also be interesting to see whether to apply the above technologies to semiconductor optical amplifiers and correlate the scattering time with gain recovery time. Last not the least it would be interesting to subject the devices to large signal modulation for real world applications.

_____

References

[5.1]   D. L. Huffaker, G. Park, Z. Zou, O. B. Shchekin and D. G. Deppe, "1.3 μm room temperature GaAs-based quantum-dot laser," *Appl. Phys. Lett*., vol. 73, no. 18, pp. 2564-2566, 1998.

[5.2]   K. Mukai and M. Sugawara, "Suppression of temperature sensitivity of interband emission energy in 1.3-μm-region by an InGaAs overgrowth on self-assembled InGaAs/GaAs quantum dots," *Appl. Phys. Lett.*, vol. 74, no.26, pp. 3963-3965, 1999.

[5.3]   Y. Tanaka, M. Ishida, Y. Maeda, T. Akiyama, T. Yamamoto, H. Z. Song, M. Yamaguchi, Y. Nakata, K. Nishi, M. Sugawara and Y. Arakawa,"High-speed and temperature-insensitive operation in 1.3 μm InAs/GaAs high-density quantum dot lasers," *in Proceedings of optical fibre communication, IEEE*, San Diego, USA, 2009.

[5.4]   S. Fathpour, Z. Mi and P. Bhattacharya, "High-speed quantum dot lasers," *J. Phys.D:* Appl. Phys., vol. 38, no. 13, pp. 2103-2111, 2005.

[5.5]   M. Ishida, N. Hatori, T. Akiyama, K. Otsubo, Y. Nakata, H. Ebe, M. Sugawara and Y. Arakawa, "Photon lifetime dependence of modulation efficiency and K factor in 1.3 μm self-assembled InAs/GaAs quantum-dot lasers: Impact of capture time and maximum modal gain on modulation bandwidth," *Appl. Phys. Letts*., vol. 85, no. 18, pp. 4145-4147, 2004.

[5.6]   A. Salhi , G. Rainò , L. Fortunato , V. Tasco , G. Visimberga , L. Martiradonna , M. T. Todaro , M. D. Giorgi , R. Cingolani , A. Trampert , M. De Vittorio and A.

_____

Passaseo "Enhanced performances of quantum dot lasers operating at 1.3µm,"
IEEE J. Sel. Topics Quantum Electron., vol. 14, no. 4, p.1188-1196, 2008.

[5.7]   R. R. Alexander, D. T. D. Childs, H. Agarwal, K. M. Groom, H. Y. Liu, M. Hopkinson, R. A. Hogg, M. Ishida, T. Yamarnoto, M. Sugawara, Y. Arakawa, T. J. Badcock, R. J. Royce and D. J. Mowbray, "Systematic study of the effects of modulation p-doping on 1.3 µm quantum-dot lasers," *IEEE. Jour. Quant. Elect.*, vol. 43, no. 12, pp. 1129-1139, 2007.

[5.8]   O. Qasaimeh and H. Kanfour "High-Speed Characteristics of Tunneling Injection and Excited-State Emitting InAs/GaAs Quantum dot Lasers," *IEE Proc. Optoelectron.*, vol. 151, no.3, pp. 143-150, 2004.

[5.9]   B. J. Stevens, D. T. D. Childs, H. Shahid, and R. A. Hogg, "Direct modulation of excited state quantum dot lasers," *Appl. Phys. Lett.*, vol. 95, no. 6, pp. 061101 - 061101-3, 2009.

[5.10] P. Xu, T. Yang, H. Ji, Y. Cao, Y. Gu, Y. Liu, W. Ma, and Z. Wang, "Temperature-dependent modulation characteristics for 1.3 µm InAs/GaAs quantum dot lasers, " *J. Appl. Phys.*, vol. 107, no.1, 013102-013102-5, 2010.

[5.11] C. S. Lee, P. Bhattacharya, T. Frost, and W. Guo, "Characteristics of a high speed 1.22 µm tunnel injection p-doped quantum dot excited state laser," *Appl. Phys. Lett.*, vol. 98, no.1, pp.011103-011103-3, 2011.

[5.12] E.C. Le Ru, P. Howe, T.S. Jones, and Murray, "Strain-engineered InAs/GaAs quantum dots for long-wavelength emission," *Phys. Rev. B*, vol. 67, no. 16, pp. 165303-165307, 2003.

[5.13] E. Clarke, P. Howe, M. Taylor, P. Spencer, E. Harbord, R. Murray, S. Kahkhodazadeh, D. W. McComb, B. J. Stevens, and R. A. Hogg, "Persistent template effect in InAs/GaAs quantum dot bilayers," *J. Appl. Phys.*, vol. 107, no. 11, pp. 113502-113502-6, 2010.

[5.14] P. Blood, G. M. Lewis, P. M. Smowton, H. Summers, J. Thomson, and J. Lutti, "Characterization of semiconductor laser gain media by the segmented contact method," *IEEE J. Sel. Topics Quantum Electron.*, vol. 9, no. 5, pp. 1275–1282, 2003.

[5.15] Q. Xie, A. Madhukar, P. Chen, and N. P. Kobayashi, "Vertically self-organized InAs quantum box islands on GaAs(100)," *Phys. Rev. Lett.*, vol. 75, no. 13, pp. 2542-2545, Sept. 1995.

[5.16] Z. Mi and P. Bhattacharya, "Molecular-beam epitaxial growth and characteristics of highly uniform InAs/GaAs quantum dot layers," J. *Appl. Phys.*, vol. 98, no. 2, pp. 023510-023510-5, 2005.

[5.17] L. V. Asryan and R. A. Suris, "Upper limit for the modulation bandwidth of a quantum dot laser," *Appl. Phys. Lett.*, vol. 96, no. 22, pp. 221112-221112-3, May 2010.

[5.18] P. D. L. Judson, K. M. Groom, D. T. D. Childs, M. Hopkinson, and R.A. Hogg, "Multi-section quantum dot superluminescent diodes for spectral shape engineering," *IET Optoelectron.*, vol. 3, no. 2, pp.100-104, 2009.

[5.19] M. A. Majid, D. T. D. Childs, H. Shahid, S. Chen, K. Kennedy, R. J. Airey, R. A. Hogg, E. Clarke, P. Howe, P. Spencer and R. Murray, "Towards 1550 nm GaAs-

based Lasers Using InAs/GaAs Quantum Dot Bilayers," IEEE *J. Sel. Topics Quant. Electron.*, vol. 17, no. 5, pp. 1334-1342, 2011.

[5.20] M. Ishida, M. Sugawara, T. Yamamoto, N. Hatori, H. Ebe, Y. Nakata and Y Arakawa, "Theoretical study on high-speed modulation of Fabry-Perot and distributed-feedback quantum-dot lasers: K-factor-limited bandwidth and 10 Gbit/s eye diagrams," *J. Appl. Phys.*, vol. 101, no. 1, pp. 013108-013108-7, 2007.

[5.21] M. Sugawara, K. Mukai, Y. Nakata, H. Ishikawa and A. Sakamoto, "Effect of homogeneous broadening of optical gain on lasing spectra in self-assembled $In_xGa_{1-x}As$/GaAs quantum dot lasers," *Phys. Rev. B*, vol. 61, no. 11, pp. 7595-7603, 2000.

[5.22] C. Y. Ngo, S. F. Yoon, D. R. Lim, V. Wong, and S. J. Chua, "Optical properties of 1.3 μm InAs/GaAs bilayer quantum dots with high areal density," *Appl. Phys. Lett.*, vol. 95, no. 18, pp. 181913-181913-3, 2009.

[5.23] R. Nagarajan, T. Fukushima, M. Ishikawa, J. E. Bowers, R. S. Geels, and L. A. Coldren, "Transport limits in high-speed quantum-well lasers: Experiment and theory," *IEEE Photon. Technol. Lett.*, vol. 4, no. 2, pp.121 - 123, 1992.

[5.24] M. Ishida, Y. Tanaka, K. Takada, T. Yamamoto, H. Song, Y. Nakata, M. Yamaguchi, K. Nishi, M. Sugawara, and Y. Arakawa, "Effect of Carrier Transport on Modulation Bandwidth of 1.3 μm InAs/GaAs Self-Assembled Quantum-Dot Lasers," *in 22nd IEEE, International semiconductor laser conference*, 2010.

Chapter 6

Optimisation of Quantum Dot Deposition by Molecular Beam Epitaxy for High Spectral Bandwidth Sources for Optical Coherence Tomography Applications

6.1 Introduction

Optical coherence tomography (OCT) is a well establsihed low coherence interferrometric technique to image the near surface of biological specimens. A broadband light source is the crucial component of the OCT system [6.1] and the development of these light sources in the region of 950-1350 nm has great potential in ophthalmic [6.2] (800-1100 nm; zero-dispersion in eye) and tissue imaging (1100-1350 nm; minimum absorption and scattering in skin) [6.3, 6.4]. The bandwidth of the source dictates the axial resolution whilst lateral resolution depends on the numerical aperture of the focussing optics. The source power dictates the signal to noise ratio (SNR), and upto a point the depth of penetration of the infrared light depends on how scattering the specimen is [6.5]. The axial resolution is related to bandwidth of the optical source as [6.4]

$$\Delta z = 2\ln(2)\,\frac{\lambda^2}{\Delta\lambda}$$

Standard OCT resolution with 10-15 µm axial resolution has been extensively used for imaging the tissue microstructure in diverse medical specialities, such as ophthalmology, gastroenterology and cardiology [6.6, 6.7]. The median size of the skin cell is ~10-20 µm and to diagnose any aberrant tissue a resolution approaching

5 µm is required. Hence for high axial resolution the optical source bandwidth of ~150 nm being required at 1300 nm wavelength to achieve ~5 µm axial resolution. Hence, an optical source with minimum bandwidth of ~150 nm is desirable for high resolution OCT. In addition to broad spectral bandwidth, due to multiple scattering in skin tissue an operating wavelength of 1300 nm is important for possible penetration in medical applications [6.3, 6.4].

There are a myriad of choices for achieving broadband light sources such as super continumm sources [6.1], swept source lasers [6.8], thermal sources [6.9] and superluminescent diodes (SLEDs) [6.10, 6.11]. SLED is an ideal light source for lower cost and robust clinical applications, being easy to operate and much less expensive than continuum light sources, thus minimizing the over all cost of the OCT system. In addition, SLEDs outperform more complex sources in terms of power output (typical 10-20 mW ex-fibre) and relative intensity noise.

The device structure of a SLED is similar to a ridge waveguide laser diode (LD); the key difference is the inhibition of optical feedback (in our case this is achieved by ridge being tilted ~7° with respect to the facet, as shown in Fig. 6.1(a)), increasing the lasing threshold so as to suppress the onset of lasing. Superluminescence is obtained by internal amplification of the self generated spontaneous emission. So in a way the SLED combines the high brightness of a laser diode and the broad optical spectrum of light emitting diode (LED) (see Fig. 6.1(b)) which is highly desirable in biological imaging, in fibre optics gyroscopes and sensors, and in wavelength division multiplexing system testing [6.12, 6.13].

Traditionally quantum wells (QW) act as the light generation and amplifying medium and have been employed to realize a broad optical spectrum of the SLED, which relies on techniques such as multiplexed broadband super luminescent diodes [6.14], intermixed quantum wells [6.15, 6.16], SLEDs integrated with tapered optical amplifiers [6.17], and chirped multiple quantum wells [6.18, 6.19] or utilizing the transitions from the higher order states of the QW. It should be noted that in all the above techniques there is a trade-off between optical power and spectral width due to reduction in peak gain. Also commercial QW based SLEDS are limited to ~100 nm of bandwidth in the 1000-1550 nm range.
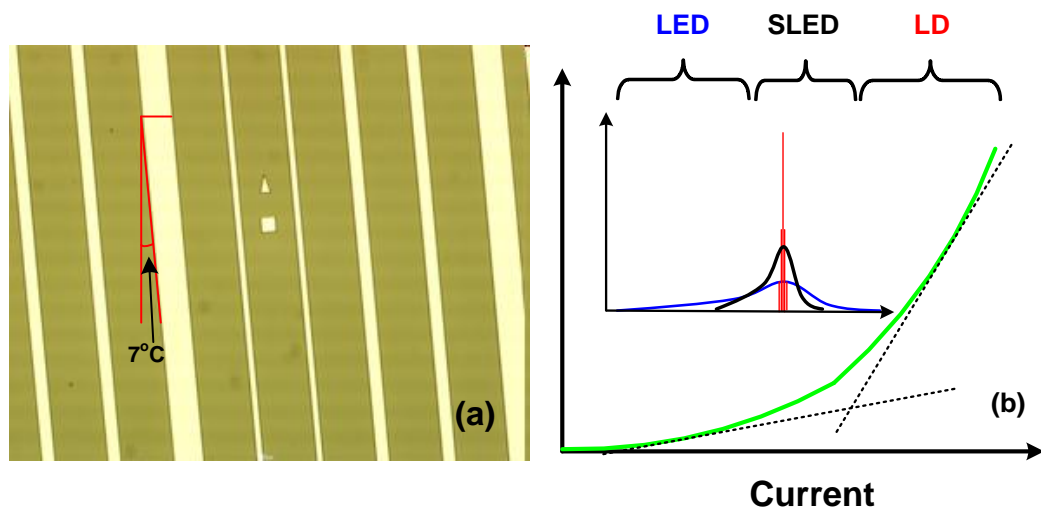

Fig. 6.1. (a) Broad area SLED with tilted facet (b) Generic schematic of an electroluminescence and L-I curve for LED, SLED, LD.

Recently, self assembled quantum dots (QD) have been proposed and demonstrated as the active element in SLEDs [6.20, 6.21]. QDs offer the advantage of inhomogenously broadened states, which may be saturated to incorporate both ground and excited states in the emission spectrum [6.20, 6.21]. In view of the above advantage, QD SLEDs are typically operated at the current density where the ground state and excited state power balances, providing the maximum spectral

bandwidth and minimum in coherence length, so maximizing OCT resolution. For QD SLEDs the device length, emission power, spectral shape and modulation bandwidth are all interlinked [6.22] and a spectral dip is usual [6.23]. The multi-contact device [6.24], lift this link and allows independent tuning of the emission power and spectral shape and hence depth and resolution in OCT are decoupled. A spectral dip, undesirable for OCT is typically reduced by varying the emission wavelength of individual 'laser QDs' in the multilayer stack [6.20, 6.25]. However this method reduces overall efficiency (reduced optical gain) of the device, as the first excited state of the short wavelength QDs overlap with highly absorbing second excited state of long wavelength QDs and also carriers in these QDs may not contribute to the output spectrum.

Figure 6.2, plots an idealized schematic showing how maximum 3dB bandwidth can be obtained by QD based SLED device. The total emission spectrum is made up of gaussian ground state and gaussian excited state emission. An ideal flat emission spectrum (maximising the 3 dB bandwidth) is obtained when the inhomogeneous linewidth of the excited and ground state (assume to be identical) equal the splitting between the ensemble peaks ($\Delta E_{split} = \Delta E_{inhom}$). This is the main aim of this chapter.

The majority of the history of active QD epitaxy development has been for QD lasers [6.26-6.33]. Size and compositional homogeneity is a problem with QDs grown by S-K growth mode. Typical size fluctuation is no better than ~ 10% [6.34] and compositional inhomogeneity harder to quantify resulting in a broad emission spectrum from the ensemble of QDs.
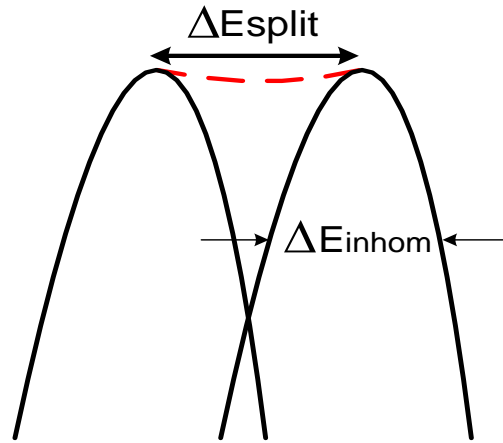
Fig. 6.2. An idealized schematic showing how maximum 3dB bandwidth can be obtained by QD based SLED device.

This inhomogeneity is a significant issue for QD laser, as those QDs outside the homogeneous line-width of the lasing energy do not merely fail to contribute to lasing, but are parasitic. Another challenging issue in using self assembled QDs for laser application is the strong gain saturation, which results from the relatively small number of states in the QD array. This results in the ground state being saturated at low-current densities, introducing emission from higher order states. This is again beneficial for SLEDs, where this increase in spectral bandwidth is desirable. Many groups have showed different approaches to circumvent this problem, for example increasing the quantum dot areal density and improving the size uniformity of the QDs [6.26-6.30]. Limited reports of low-threshold current densities, high characteristic temperature, wavelength stability under direct modulation and temperature insensitive operation are reported for these QD lasers [6.31-6.33]. In all the studies for QD laser epitaxy, high growth temperature and low growth rates are used to obtain a narrow ground state linewidth. As a result, the majority of existing epitaxial processes for active QD devices are not optimised

for broadband applications. However, high QD density and high integrated modal gain is advantageous.

To date there have been limited studies where QDs growth parameters optimized for broadband applications [6.20-6.24]. The previous studies on epitaxy for broadband application by our group suggest that growth temperature is the key parameters for high power broadband QD SLEDs [6.24, 6.35, 6.36].

Here I present a comparison of the growth conditions, photoluminescence (PL) measurements, atomic force microscopy (AFM) measurements and device characteristics affecting 1200-1300nm quantum dot-in-well structures with a view to their optimization for broadband applications. In particular we have varied QD deposition temperature, the amount of InAs deposited to form the QDs, the InAs QD growth rate and low-temperature (LT) GaAs spacer layer thickness. A systematic PL study is carried out on these samples which allows the spontaneous efficiency to be compared. Further AFM analysis on the dots allows the measurement of the dot density and uniformity which in turn suggests conditions which will produce an optimum gain spectrum shape.

6.2 Experimental

All the samples studied in this thesis were grown on Si-doped GaAs (100) substrates using a V90 H molecular beam epitaxy (MBE) system by Dr Maxime Hugues.

Two types of structures have been grown: the test samples (Fig. 6.4) for PL and AFM measurements and SLED structures (Fig. 6.3) to evaluate the device performances. The active layer sequence is the same for both structure and only

the cladding layers are different (Fig. 6.3 and Fig. 6.4). The growth procedure for SLED structure is as follows.

After oxide desorption at 600 °C, a 300 nm thick Si-doped GaAs buffer layer was grown at 580 °C, followed by a 2000 nm Si-doped (2×10^{18} cm^{-3}) Al$_{0.35}$Ga$_{0.65}$As layer and a 300 nm Si-doped (5×10^{17} cm^{-3}) Al$_{0.35}$Ga$_{0.65}$As layer, grown at 600 °C. The active region of the samples consists of InAs QDs grown within an InGaAs quantum wells (QW), a structure popularly known as the dot-in-well (DWELL). The active region consists of six-repeats of DWELL structure and 45 nm of undoped GaAs spacer layer (SPL). The QDs are formed by depositing 2.6 monolayers (MLs) of InAs deposited at a growth rate of 0.1 ML/s grown on 1nm of In$_{0.15}$Ga$_{0.85}$As strained buffer layer and capped by 6 nm of In$_{0.15}$Ga$_{0.85}$As strain reducing layer (complete DWELL structure) and 5 nm (LT GaAs spacer layer grown at same temperature as QDs) of GaAs before increasing the temperature to 580 °C for the remaining 40 nm of GaAs. The temperature was then reduced for the growth of the next DWELL. This high-growth–temperature GaAs spacer layer (HGTSL) is found to reduce the defect density and improves the laser performance [6.37]. After the active region was deposited, an upper cladding layer made up of 500 nm of a Be-doped (2×10^{17} cm^{-3}) Al$_{0.35}$Ga$_{0.65}$As, a 1250 nm Be-doped (2×10^{18} cm^{-3}) Al$_{0.35}$Ga$_{0.65}$As grown at 600 ^{o}C and a 300 nm highly doped GaAs contact layer, grown at 580 ^{o}C.

To allow PL studies to be consistent with electrical characteristics of the SLED, test samples with the same DWELL were grown. QDs have also been deposited on the sample surface (see Fig. 6.4) to evaluate the QD size, density and distribution variation from AFM measurements. Special care has been taken by ramping down
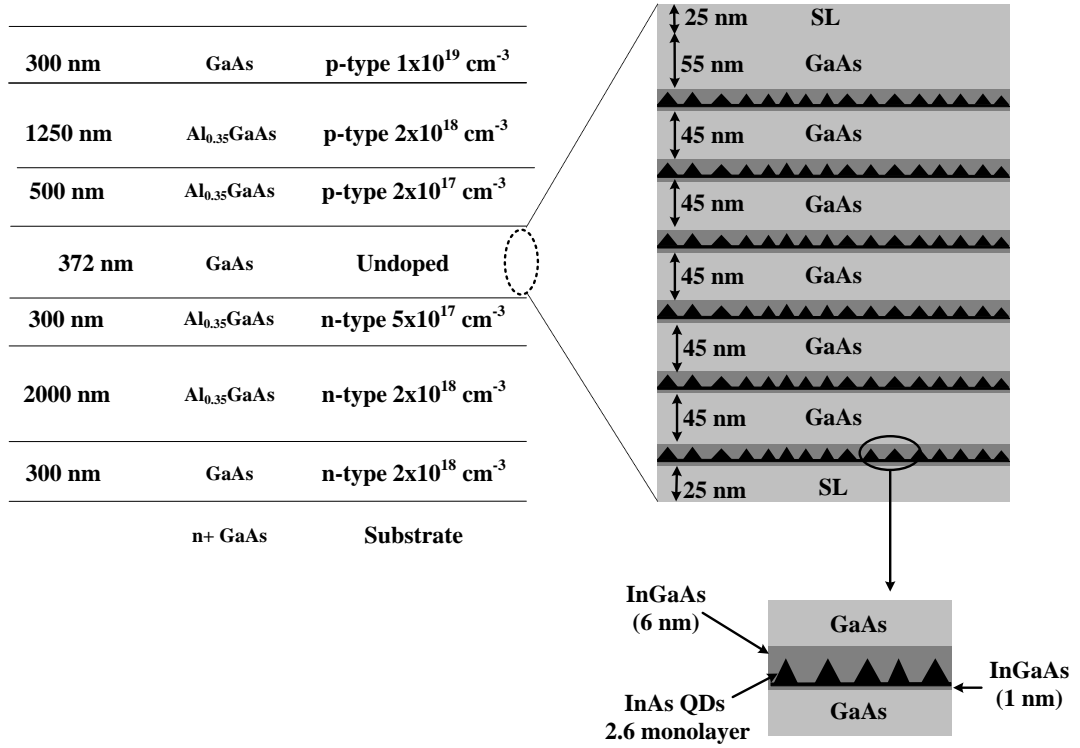
300 nm	GaAs	p-type 1×10^{19} cm^{-3}
1250 nm	Al$_{0.35}$GaAs	p-type 2×10^{18} cm^{-3}
500 nm	Al$_{0.35}$GaAs	p-type 2×10^{17} cm^{-3}
372 nm	GaAs	Undoped
300 nm	Al$_{0.35}$GaAs	n-type 5×10^{17} cm^{-3}
2000 nm	Al$_{0.35}$GaAs	n-type 2×10^{18} cm^{-3}
300 nm	GaAs	n-type 2×10^{18} cm^{-3}
	n+ GaAs	Substrate

25 nm SL
55 nm GaAs
45 nm GaAs
45 nm GaAs
45 nm GaAs
45 nm GaAs
45 nm GaAs
25 nm SL

InGaAs (6 nm)
GaAs
InGaAs (1 nm)
InAs QDs 2.6 monolayer
GaAs

Fig. 6.3. Schematic of the cross-section of a 6 layered DWELL InAs/GaAs QD SLED.

InAs – QDs
InGaAs – 1nm
GaAs – 100nm
AlGaAs (30%) – 100nm
GaAs – 100nm
GaAs – 15nm
LT-GaAs – 5nm
InGaAs – 6nm
InAs – QDs
InGaAs – 1nm
GaAs – 25nm
GaAs – 100nm
AlGaAs (30%) – 100nm
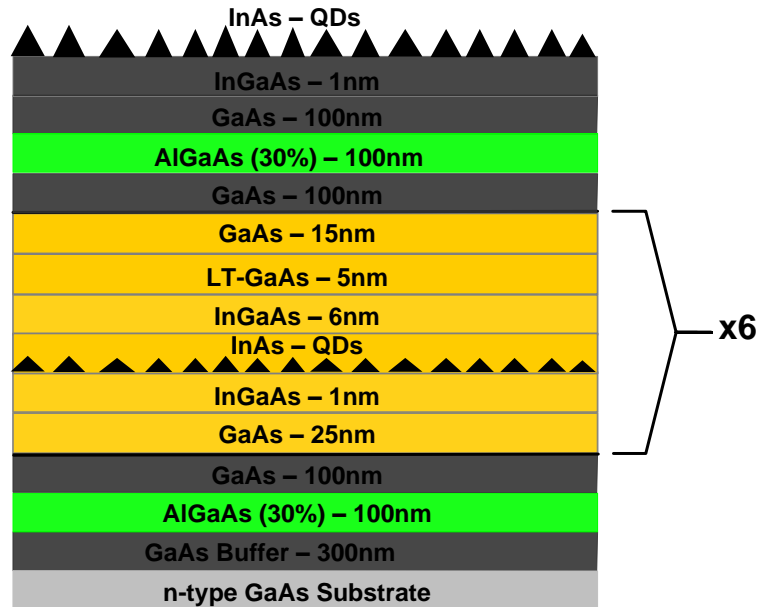GaAs Buffer – 300nm
n-type GaAs Substrate

x6

Fig. 6.4. Test structure for AFM and PL.

the growth temperature as quickly as possible at the end of the growth in order to avoid/reduce the ripening processes. Note that AFM does not give the "real" dimension since the QD size are affected by the capping procedure. However this technique gives a good qualitative indication of the initial size distribution of the dot and of their density. Details of the sample number, DWELL growth temperature for photoluminescence, atomic force microscopy and SLED structure will be discussed in the next sections.

6.3 Optimising the Growth of 1.3µm InAs/GaAs DWELL Structures

To improve the properties of multilayer QD structures for broadband applications, a comprehensive study of the growth process relevant to the fabrication of 1.3 µm InAs/ GaAs DWELL SLED structures was carried out. This involved a close collaboration with the MBE growers in the EPSRC National Centre for III-V Technology at the University of Sheffield. The following sections details the optimization in terms of the QD DWELL growth temperature, and the InAs deposition amount at a constant InAs deposition rate of 0.1 monolayer/sec (ML/s) . The choice of 0.1 ML/s is in contrast to the slow growth (≤ 0.05 ML/s) rate used for QD lasers. It is shown that growth temperature and deposition amount are key to produce high quality broadband SLEDs.

6.3.1 Effects of InAs/GaAs QD Growth Temperature

In the introduction it has been discussed that the majority of the previous work on epitaxy of QDs, was focussed on QD lasers. There has so far been no systematic study for optimization of QDs for broadband application, especially in terms of the PL, AFM and opto-electronic characterization.

Sample number	QD growth temperature (°C)	InAs growth rate ML/s	InAs (ML)
Vn1683	525	0.1	2.6
Vn1692	515	0.1	2.6
Vn1690	500	0.1	2.6
Vn1693	470	0.1	2.6
Vn1694	485	0.1	2.6
Vn1686	460	0.1	2.6

Table.6.1. Samples for PL and AFM studies.

Keeping this in mind, we began our growth campaign with eight test structures but due to close QD DWELL growth temperature range and similar PL and AFM results for some of the samples, I concentrated my studies on six test structures as shown in table 6.1, where the QD DWELL growth temperature was varied, with a constant InAs QD deposition amount (2.6 ML) and growth rate (0.1 ML/sec).

6.3.1.1 Structural and Optical Comparison

Before studying the properties of the SLED, a comparison of the structural and optical properties of the DWELL test structures will be presented. Room-temperature photoluminescence were carried out at a relatively low excitation power (~8 mW) using the 632 nm line of a HeNe laser. Room-temperature PL spectra for different DWELL growth temperatures (T_g) are shown in Fig. 6.5. The PL intensity decreases by a factor ~10 as the QD growth temperature is decreased from 515 °C to 470 °C. The PL intensity at 460 °C is ~ 8 times lower than that at 470 °C. The decrease in PL intensity indicates an increase in the non-raditaive centre density with decreasing T_g. Their origins could be defective dots or/and larger Ga vacancy and As antisite densities induced by the lower growth temperature of the cap layer. For these samples, the emission wavelength is in the range of 1225-1290 nm. The redshift of the emission wavelength is attributed to the increase in size or indium contents in QDs [6.38]. The PL intensity for QD grown at 525 °C is ~half of that at 515 °C or 500 °C and a blueshift of ~40 nm is observed. The origin of the PL intensity reduction is not clear but could be tentatively attributed to a lower QD density as we will see later. For the sample grown at 525 °C, the bluehshift could be attributed to at least 3 processes: In/Ga intermixing [6.27, 6.39], In segregation, and certainly the more significant the In desorption (re-evaporation).
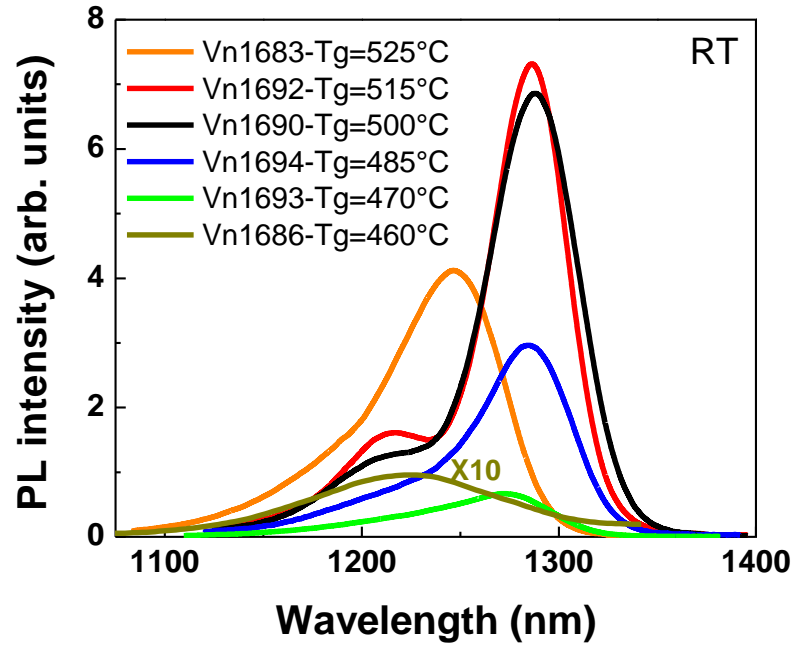
Fig. 6.5. Room temperature PL from DWELL grown at 525 °C, 515 °C, 500 °C, 485 °C, 470 °C, 460 °C.
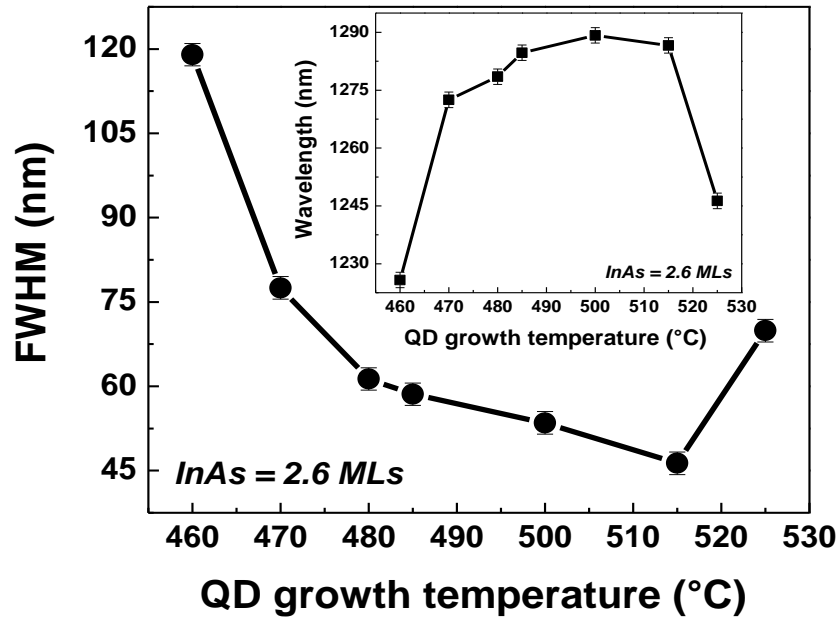

Fig. 6.6. Room temperature FWHM of PL obtained from DWELL grown at different temperature. Inset: PL peak emission wavelength versus the QD growth temperature.

Figure 6.6, shows the variation of the full width at half maximum (FWHM) and peak emission wavelength (inset) for these samples. One more QD growth temperatures (Tg = 480 °C) are included in Fig. 6.6, which are not shown in Fig. 6.5, as the PL for 480 °C is comparable to that for 485 °C. It is evident from the figure that the FWHM increased by a factor of ~3, as the QD growth temperature is deceased from 515 °C to 460 °C. The Tg of 460 °C and 470 °C are interesting due PL spectrum bandwidth of ~120 and 75 nm, showing potential for OCT application. The peak emission wavelength for Tg= 515 °C to 470 °C (Inset Fig. 6.6) occurs in the range of 1275-1290 nm. In this temperature range, the intermixing and segregation slightly decrease with the temperature while the In desorption is completely avoided (the In desorption appears around 520 °C. This is an interesting QD growth temperature range for QD SLED devices for OCT of skin tissue.
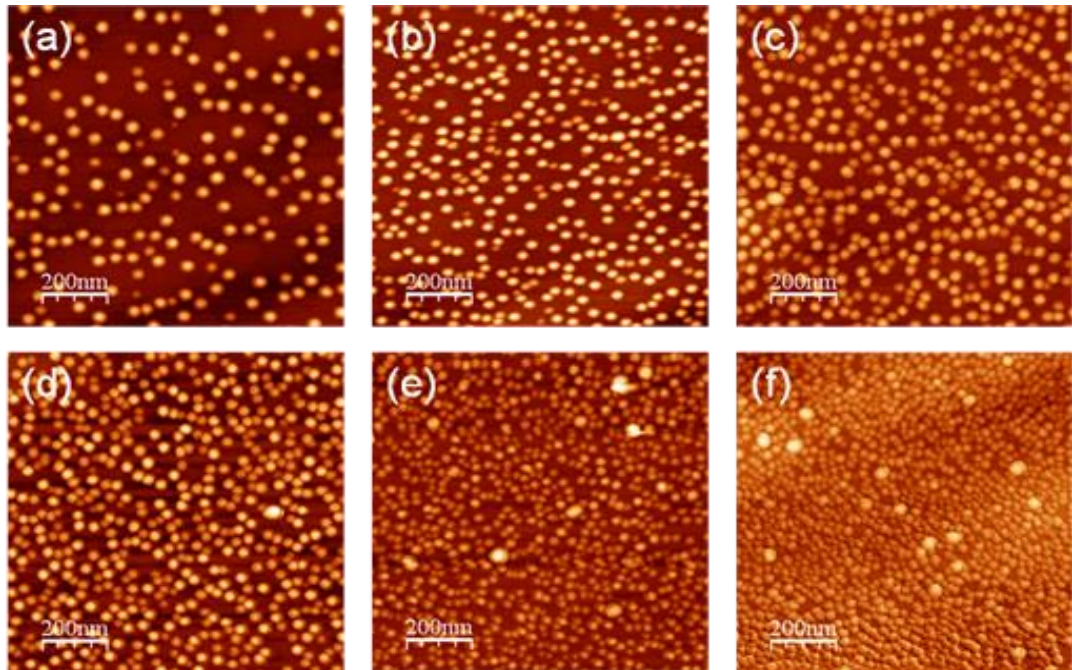

Fig. 6.7. Plan view 1 X 1 μm^2 AFM images obtained from InAs/GaAs QD DWELL grown at (a) 515 °C, (b) 500 °C, (c) 490°C, (d) 485 °C, (e) 470 °C, and (f) 460 °C. (Courtesy Dr Maxime Hugues)
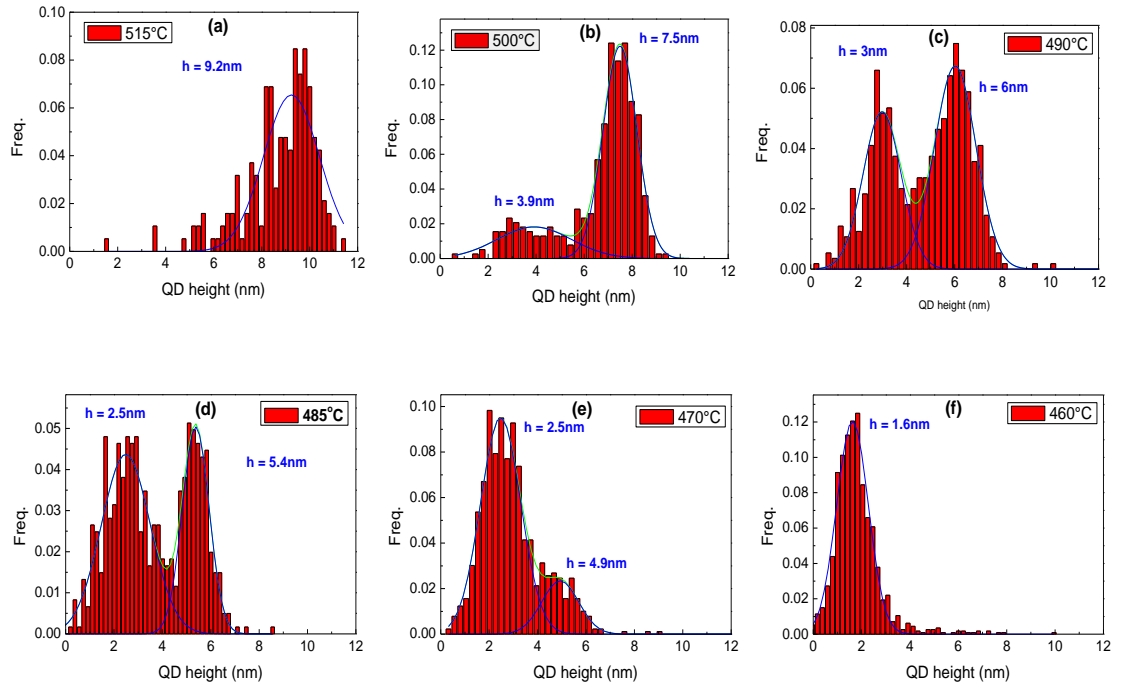
Fig.6.8. QD height as a function of frequency of occurrence, obtained from AFM scans of Fig. 6.7. (Courtesy Dr Maxime Hugues)

Figure 6.7, shows 1 X 1 μm^2 AFM images of the surface dots grown at: 515 °C, 500 °C, 490 °C, 485 °C, 470 °C and 460 °C respectively. These figures show an increase in the QD areal density, increased coalesced island (the large islands correspond to coalesced dots) density as growth temperature decreases from 515 °C to 460 °C [6.38, 6.40, 6.41]. With an increase in QD areal density an increase in PL intensity is expected, but the greater defect density due to increased coalesced islands (coalesced island leads to dislocation creation acting as non-radiative centres) may overwhelm this effect.

Figure 6.8, plots a histogram of the QD height from the AFM samples. For each graph the sum of frequency equals 1 (100%). These figures show an increase in average island height (six fold increase) as the growth temperature is increased from 460 °C to 515 °C [6.38, 6.42]. Height increase induces an emission redshift,

which is inline with the PL results shown in see Fig. 6.5. Interestingly, a bimodal distribution of dot height is noted for fig. 6.7(c-e), becomes significant due to shorter indium diffusion lengths on the surface [6.42]. These results are in good agreement with the observed broadening of the FWHM i.e inhomogeneous broadening of QDs due to large dot height variation with a decrease in growth temperature from 515 ^{o}C to 460 ^{o}C. In conclusion, the QDs grown at lower temperature exhibit shorter wavelength (smaller dots), larger inhomogeneous broadening (stronger size variation influence) and lower peak intensity (coalesced dot) than the ones grown at "normal" temperature (i.e. 500-510 °C for laser).

Figure 6.9, plots the QD areal density obtained from the AFM of Fig. 6.7. The QD areal density is observed to increase by a factor of ~7 times with the decrease in QD growth temperature from 515 ^{o}C to 460 ^{o}C. This evolution has already been reported several times [6.38] and it has been attributed to the decrease of the In adatom diffusion length. Figure 6.10, plots the density of coalesced QD island obtained from 5 X 5 μm^2 AFM images. The coalesced island density increased by a factor of ~20 as the QD growth temperature is decreased from 515 ^{o}C to 460 ^{o}C. Though the increase in dot density is highly desirable, a significant increase in coalesced island density is expected to be detrimental for efficient device operation. As the QD density increases, coalescence of the QDs results in additional non-radiative defects, evidenced by a strong reduction in PL intensity (see Fig. 6.5). Note that In intermixing or segregation processes change the dot size/composition but do not affect their density [6.43].
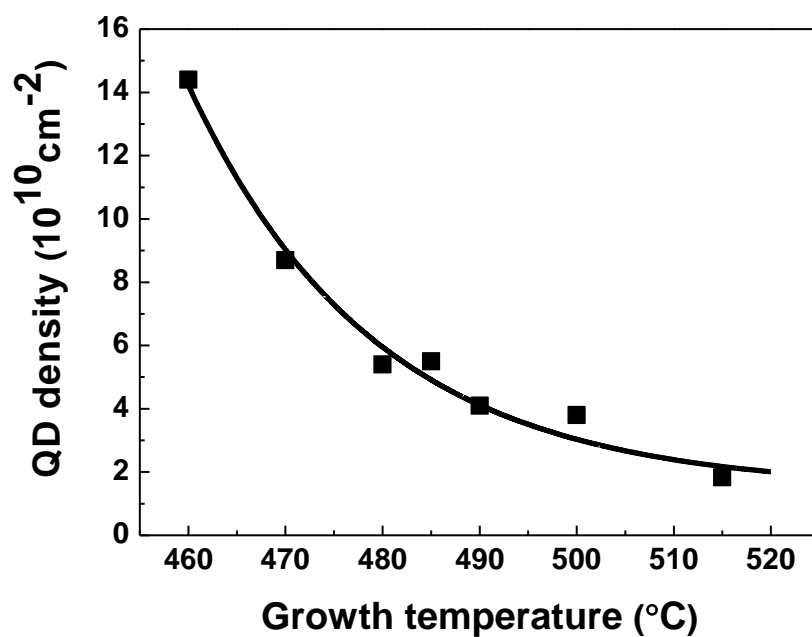
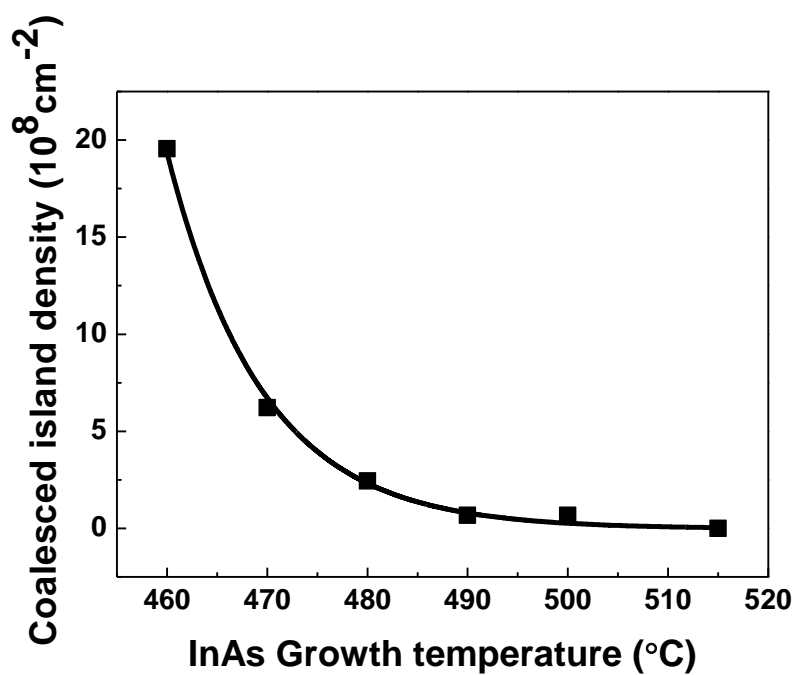**Fig. 6.9.** QD areal density plotted as a function of QD InAs/GaAs DWELL growth temperature.

Fig. 6.10. Coalesced island density plotted as a function of QD InAs/GaAs DWELL growth temperature.

6.3.1.2   Electrical and Optical Comparison

Based on PL and AFM studies, four growth temperatures, shown in table 6.2, were

selected for studying the opto-electronic characteristics of the SLED and to

compare these results with the PL and AFM studies presented earlier. The samples

are processed into broad area SLEDs (see Fig. 6.1(a)) in the same manner as

described in chapter 2. The only difference being that the SLED ridges were tilted

by 7° from the normal to the as-cleaved facet. All the devices were mounted on

ceramic tiles and directly pin-probed. All measurements were carried out at a tile

temperature of 300 K. Characteristics were measured in the pulsed regime (5 µs

pulsed duration, 1% duty cycle) to minimize the thermal effects. For all the

analyses in the following paragraphs, 6 mm long device and 50 µm wide ridge

width was used.

Sample number	QD growth temperature (°C)	Growth rate ML/s	InAs (ML)
Vn1696	500	0.1	2.6
Vn1697	470	0.1	2.6
Vn1699	485	0.1	2.6
Vn1701	515	0.1	2.6

Table. 6.2. SLED Structure.

Figure 6.11, shows the power–current density (L-I) response measured from one

facet of the SLEDs at different DWELL growth temperatures. This figure shows

limited superluminescence for QD growth temperature of 470 ^{o}C and 485 ^{o}C

suggesting limited gain. However superluminescent behavior is evidenced by the

super linear increase in optical power with increasing current density for QD

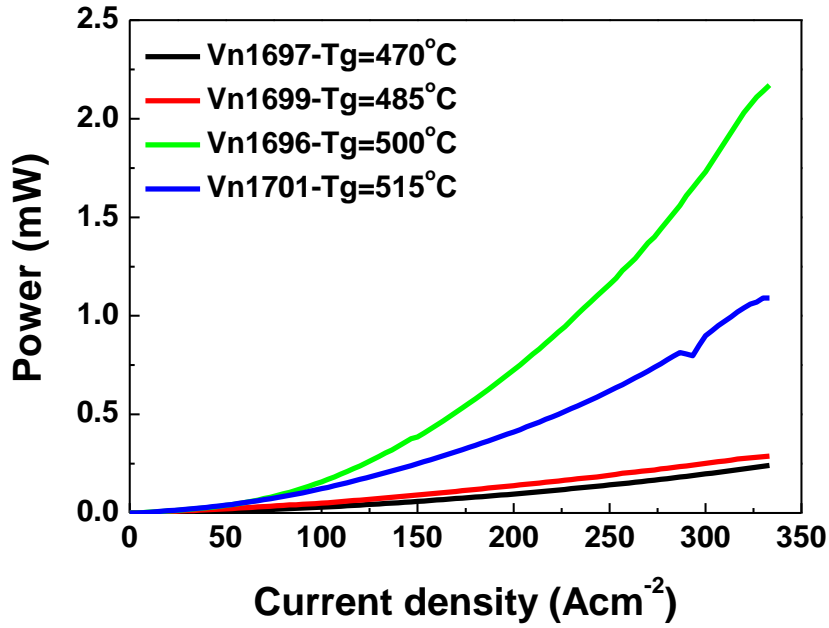growth temperature of 500 ^{o}C and 515 ^{o}C. A tenfold increase in optical power is

Fig. 6.11. Power-current characteristics of the SLEDs for different DWELL growth temperatures.

noted at current density of 330 A/cm^2, for QDs grown at 500 ^{o}C as compared to 470 ^{o}C, whilst the areal density is half (see Fig. 6.9). This result would have been surprising if one would only consider the QD areal density. However, we must recall the coalesced island density which increased by a factor of ~12 for QDs grown at 470 ^{o}C as compared to QDs grown at 500 ^{o}C. This is suggestive that a comprehensive study of QD density versus growth temperature is meaningless without accounting for coalesced island density.

Figure 6.12, shows the power-current characteristics at low current density by re-plotting the data in Fig. 6.11. The figure depicts a clear trend of the increase in spontaneous emission efficiency (SE) with an increase in the QD growth temperature. The decrease in SE even though there is an increase in QD areal

density with the decrease in QD growth temperature is attributed to the increase in coalesced island density.
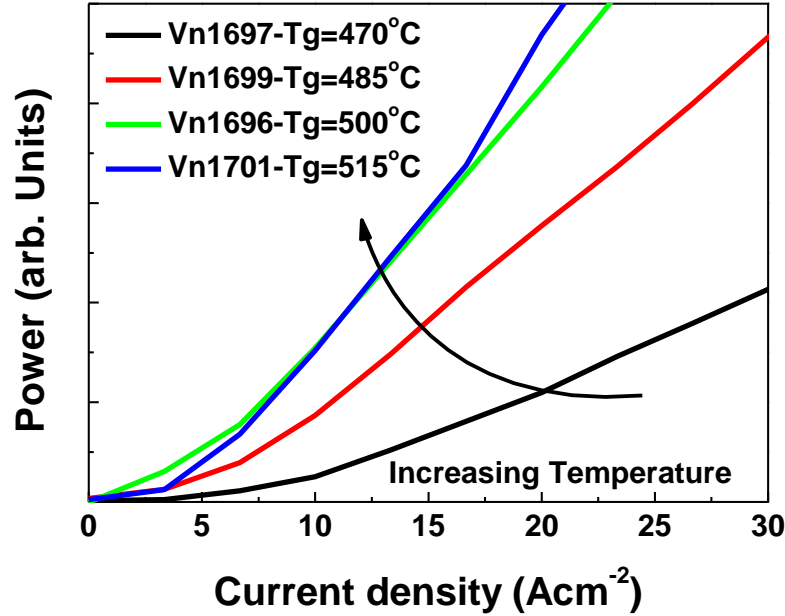

Fig. 6.12. Exploded view of the Fig. 10 at low current density.

Figure 6.13, plots the electroluminescence spectra (EL) as a function of increasing current density for different QD SLED, grown at (a) 515 °C, (b) 500 °C, (c) 485 °C, (d) 470 °C. The ground state FWHM as a function of growth temperature is plotted in Fig. 6.14. This trend of increasing ground state FWHM is in good agreement with the PL FWHM plotted in Fig. 6.6. Previous studies on laser diode epitaxy [6.27-6.30] have shown that, at high QD growth temperatures the QDs tends to be more uniform in size, but also bigger (less sensitive to size fluctuations), which reduces the linewidth. On the other hand, reducing the QD growth temperature decreases the indium adatom mobility, thus favoring the formation of a large density of small dots.
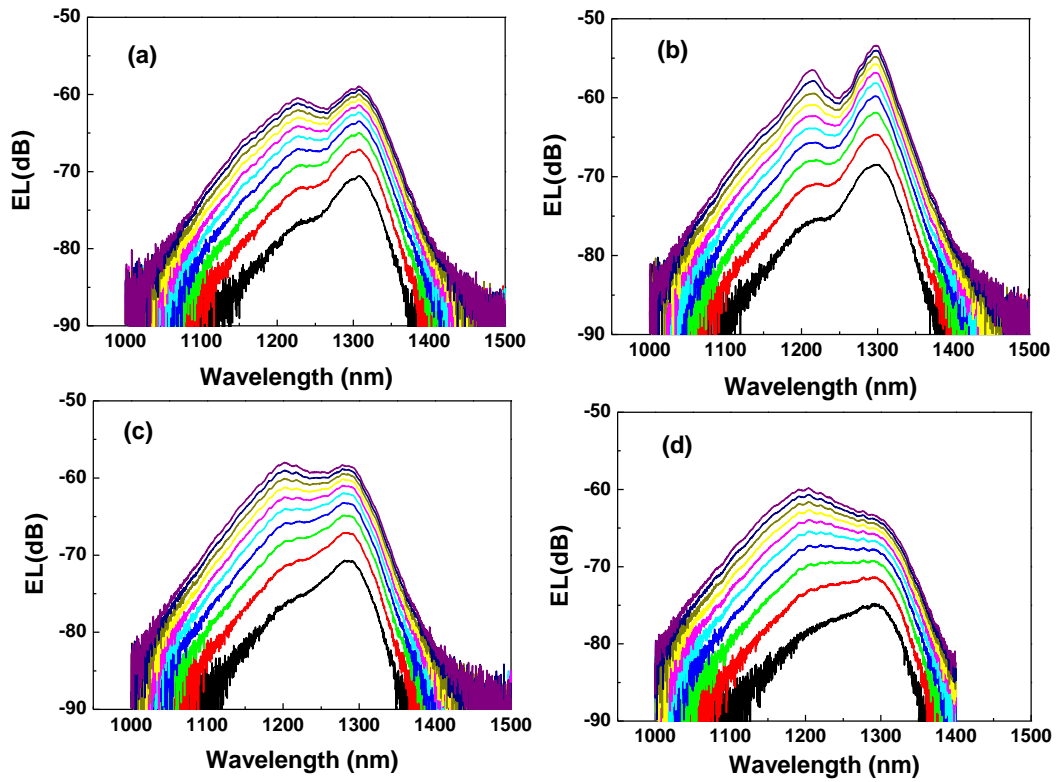
Fig. 6.13. EL spectrum as a function of increasing current density (33-330 A/cm^2) for DWELL SLED grown at (a) 515 °C, (b) 500 °C, (c) 485 °C, (d) 470 °C, with a constant InAs coverage of 2.6 ML.

Thus, the size fluctuations will have a strong impact on their electronic properties resulting in a broad emission spectrum (the balance of ground and excited state increase the spectral bandwidth, as shown in Figs 6.13. (c) and (d)). The reduction in spectral dip with decreasing growth temperatures is noted which is due to the increase in the linewidth of the QD ground state and excited state ensemble.

Figure 6.15, shows the integrated PL intensity and electroluminescence (EL) efficiency, as a function of QD growth temperature. The EL efficiency and integrated PL efficiency are calculated from Figs. 6.5 and 6.11 respectively. This figure shows that the EL efficiency of the SLED devices has good correlation with the integrated PL efficiency of the test structures. These results again re-emphasise
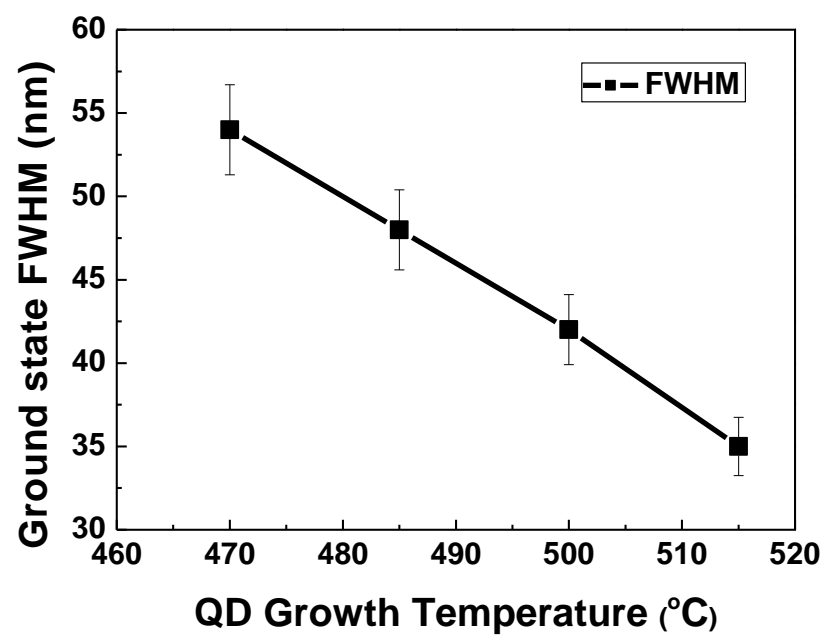
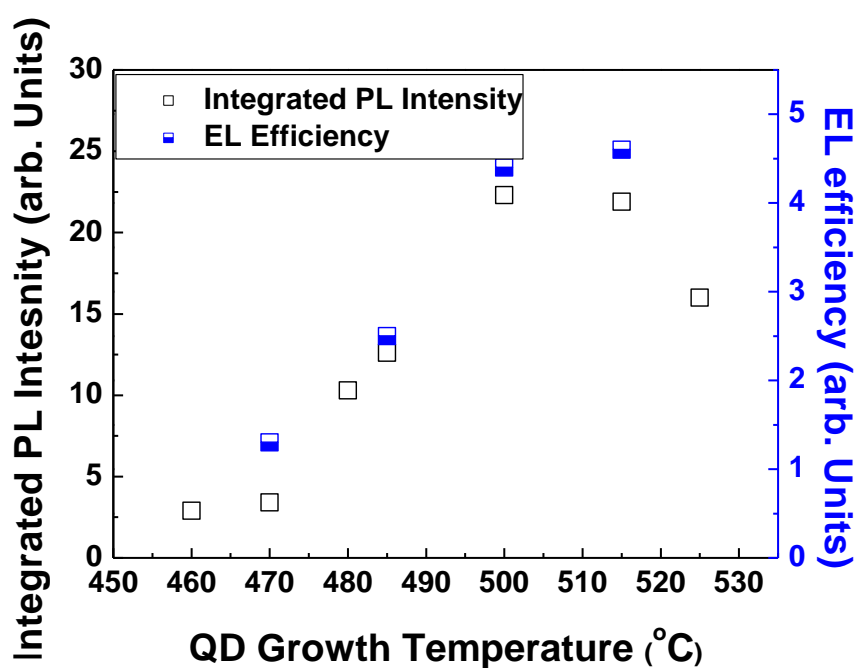**Fig. 6.14.** Ground state FWHM as a function of QD growth temperature.

Fig. 6.15. Integrated PL intensity and EL efficiency plotted as a function of QD growth temperature.
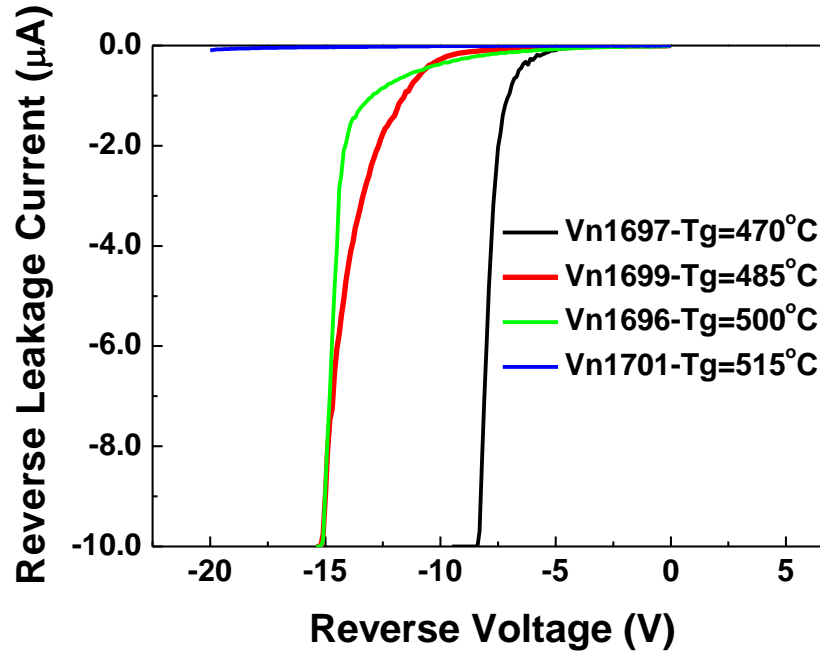
Fig. 6.16. Reverse leakage current as a function of the reverse bias voltage for different QD DWELL growth temperatures.

that for optimisation studies a good agreement of optical, structural and electrical studies is essential. In this case PL, AFM and electrical characteristics are key in selecting particular QD growth temperature.

Defects within active media have previously been shown to result in a leakage current observed in the reverse bias current-voltage (I-V) characteristics [discussed in detail in chapter 3]. SLEDs of 6 mm long device and 50 μm ridge were electrically characterized at room temperature using a Hewlett-Packard 4155A semiconductor parameter analyzer. Figure 6.16, shows the reverse leakage current plotted as a function of reverse bias. A sharp and high breakdown voltage is noted as the DWELL growth temperature increased from 470 °C to 515 °C. The breakdown voltage of the sample grown at 515 °C is a factor of ~3 higher and leakage current a factor ~10 less as compared to the sample grown at 470 °C. The low breakdown voltage, high leakage current is indicative of the higher defect densities (for QDs

grown at low-temperatures), which is consistent with the PL, AFM and other
electrical characteristics, discussed above.

In terms of small spectral dip (inhomogeneous linewidth is equal to 75 nm which is
close to splitting between the states), high dot density (8×10^{10} cm^{-2}) if one wants
to benefit from the broad emission of the QD grown at low-temperature (i.e. 470
°C) one must further optimise the growth condition/InAs deposition, in order to
improve the PL efficiency and the electrical performances.

6.3.2 Effects of InAs QD Deposition Amount

To determine if the quality of the QDs grown at 470 °C can be improved, 5 test
samples with different InAs amount have been grown (see table 6.3). For this
study, the InAs growth rate was kept constant at 0.1 ML/s.

Sample number	QD growth temperature (°C)	Growth rate ML/s	InAs (ML)
Vn1695	470	0.1	2.0
Vn1764	470	0.1	2.1
Vn1698	470	0.1	2.2
Vn1762	470	0.1	2.3
Vn1693	470	0.1	2.6

Table. 6.3. Samples for PL and AFM measurements.

6.3.2.1   Structural and Optical Comparison

Figure 6.16, shows the room-temperature PL emission for test samples with InAs
amount ranging from 2.0 to 2.6 ML. For 2.0 and 2.1 ML a single well resolved peak
emission can be observed, with a peak wavelength of ~ 1185 nm and 1200 nm
respectively. As the amount of InAs deposited is increased to 2.2 ML, an unresolved
doublet can be observed with a dominant emission at ~1240 nm and a broad
shoulder at ~1270 nm. The broad emission persists for further InAs deposition of

2.3 ML with a dominant peak at 1260 nm and shoulder at ~1230 nm. The broad

shoulders and dominant peak for samples with 2.2, 2.3 ML are approximately 23

meV apart (~30 nm), which rules out excited state transitions (separation between

the ground state and the first excited state is generally 60-90 meV), suggesting that

the form of PL is due to two subsets of QDs (dots with different size emit at

different wavelength), a bimodal behaviour. As the amount of InAs deposited is

further increased to 2.6 ML a single well resolved peak was observed at ~1275 nm,

suggesting that the uniformity of the QD ensemble improves (suitable for a laser

structure). A significant increase in the PL intensity can be observed with

decreasing InAs deposition from 2.6 to 2.0 ML, indicating increased coalesced
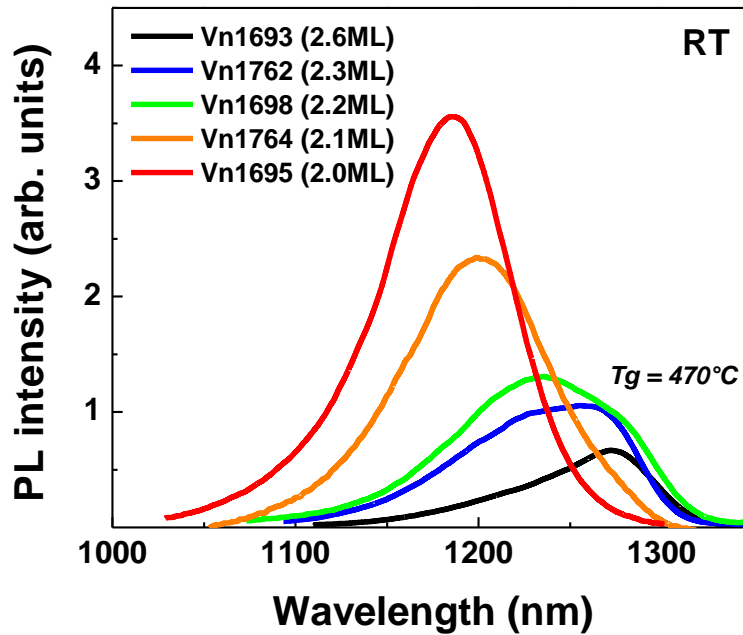
island (non-radiative centers) density.

Fig. 6.17. Room temperature PL obtained from DWELL grown at 470 °C for various InAs coverages.

Figure 6.18, plots the effect of InAs deposition on the peak PL emission. The peak PL emission increases ~90 nm (~1185-1275 nm) with increase in the InAs deposition. As the InAs deposition is increased from 2.0 to 2.1 ML a wavelength increase of ~10 nm is observed, suggesting the dot size and indium composition are similar. As the amount of InAs was further increased to 2.2 ML (0.1 ML more) a significant increase in the wavelength (~40 nm) can be observed, suggesting bigger and more indium rich dots. For 2.3 to 2.6 ML InAs deposition, a ~20 nm of redshift in wavelength was observed, suggesting similar dots or most additional material (indium) migrating to coalesced dot [6.38].
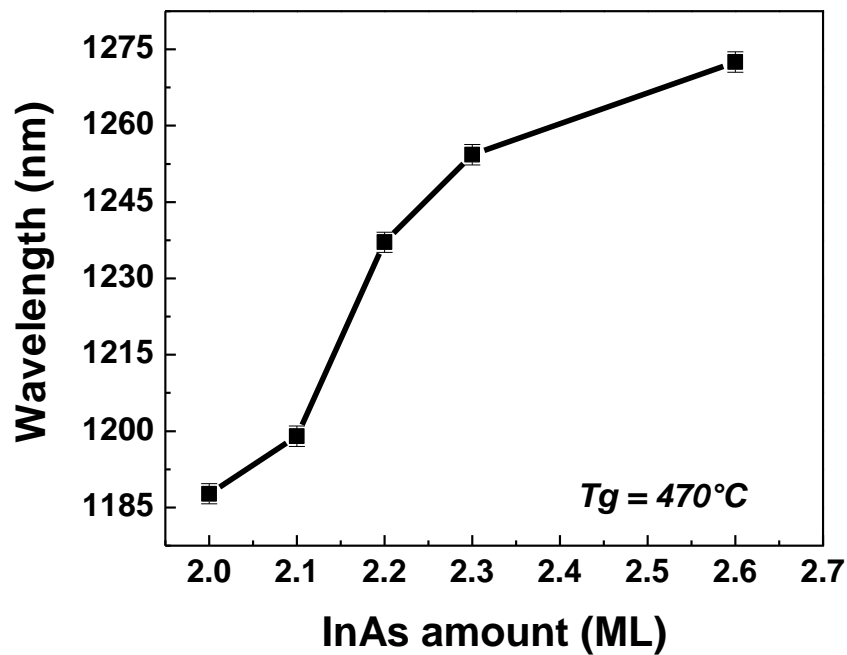

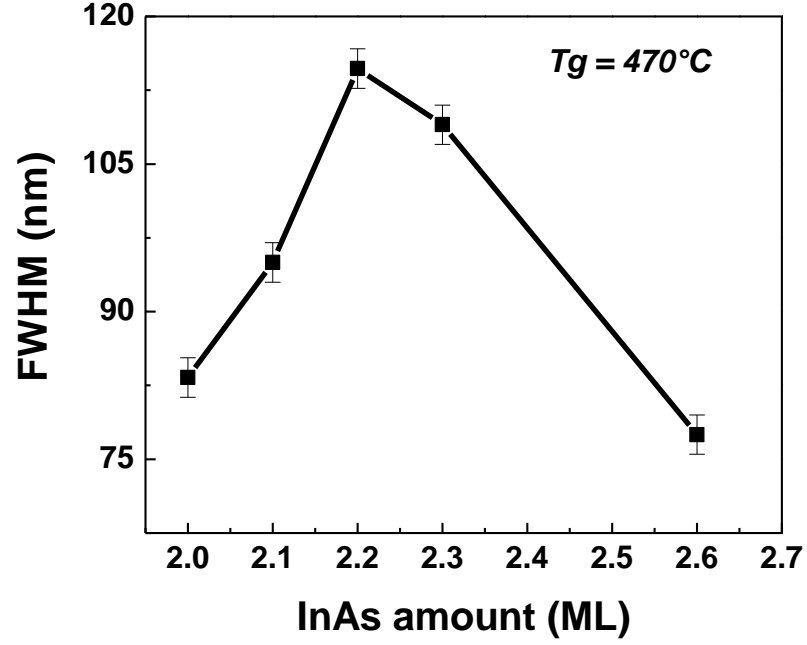**Fig. 6.18.** Effect of InAs deposition on the peak PL emission.

Fig. 6.19. Effect of InAs deposition on the FWHM of PL emission.
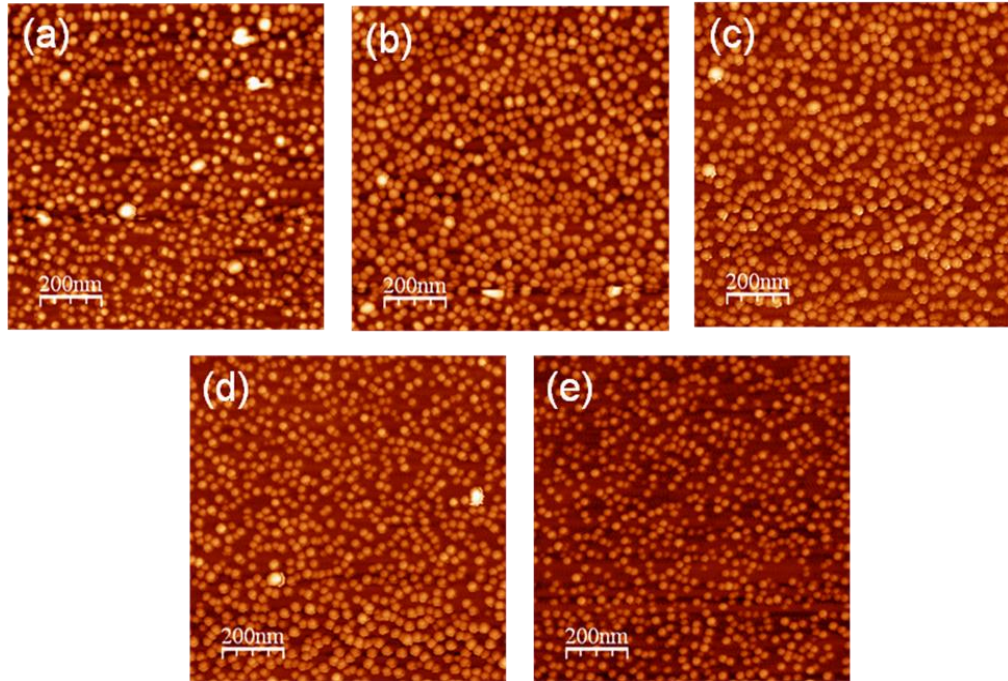

Fig. 6.20. Plan view 1 X 1 μm^2 AFM images obtained from InAs/GaAs DWELL grown at 470 ^{o}C with InAs coverage of (a) 2.6 ML, (b) 2.3 ML, (c) 2.2 ML, (d) 2.1 ML, and (e) 2.0 ML (courtesy Dr Maxime Hugues).

Figure 6.19, plots the effect of the InAs deposition on the FWHM. As the amount of InAs deposited increased from 2.0 to 2.2 ML FWHM is increased from 80 to 115 nm suggesting a uniform to bimodal QD distribution. The FWHM is approximately the same for a further 0.1 ML of InAs (2.3 ML). A further increase of InAs deposition from 2.3 to 2.6 ML the FWHM significantly decreased from 110 to 75 nm, suggesting a shift from bimodal to single modal distribution of QDs. A decrease in PL intensity is also noted as InAs coverage is increased from 2.0 - 2.6 ML.

To further understand the effect of InAs deposition, AFM was performed on the test structure, as discussed earlier. Figure 6.20, shows 1 X 1 μm^2 AFM images for the range of InAs deposition (2.6 to 2.0 ML). The DWELL growth temperature and rate were kept constants at 470 ^{o}C and 0.1 ML/s, respectively. As the amount of InAs deposition increases, larger islands will form, which may incorporate material at the expense of smaller islands [6.27, 6.38]. An increase in average island size can be seen as the deposition amount is increased from 2.0 to 2.6 ML. Increasing the InAs deposition amount results in larger QDs, exhibiting a narrower FWHM (Fig. 6.19). These results suggest that the optical and structural properties of InAs/GaAs QD DWELL structures are improved by decreasing the InAs deposition from 2.6 to 2.0 MLs. It is also interesting to note that although the samples with 2.6, 2.0, 2.1 ML InAs coverage are not suitable for use in QD SLEDs, they may be a promising candidate for QD lasers, due to their narrow PL FWHM.

Figure 6.21, shows the QD dot density plotted as a function of InAs coverage. The QD density varies in the range of (7.5-8.5)±5 X 10^{10} dots/cm^2, as expected nominally constant dot density for a range of InAs coverage.

Figure 6.22, shows the coalesced island density obtained from 5 X 5 μm^2 AFM images, plotted as a function of the InAs deposition amount. This figure shows a significant increase in coalesced island density with an increase in InAs coverage from 2.0 to 2.6 ML. A factor of ~ 7 increases in the coalesced island density is noted for 2.6 ML QD InAs coverage as compared to 2.0 ML. The coalesced island density increases linearly until 2.3 ML, and as the InAs coverage is further increased an exponential increase in the coalesced island density is noted.
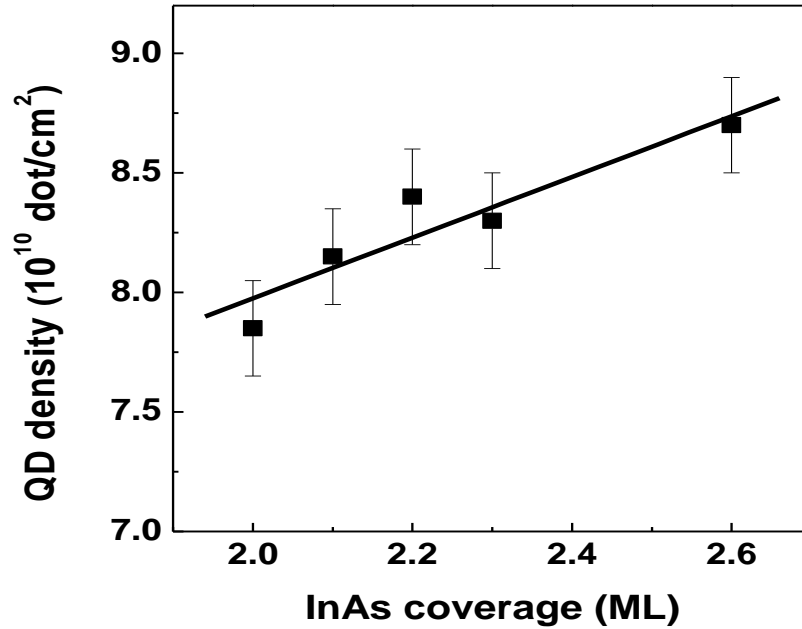
Fig. 6.21. QD areal density as a function of QD InAs coverage.

Frigeri *et al.* [6.44] have also observed the onset of these irregular islands in single layer InAs/GaAs QD growth after 2.4 ML of InAs deposition. Experimental evidence of large incoherent islands in high coverage InAs/GaAs QDs are reported in [6.45, 6.46], suggested a value of about 3 ML, as the critical coverage for strain relaxation leading to significant carrier depletion in the QDs.
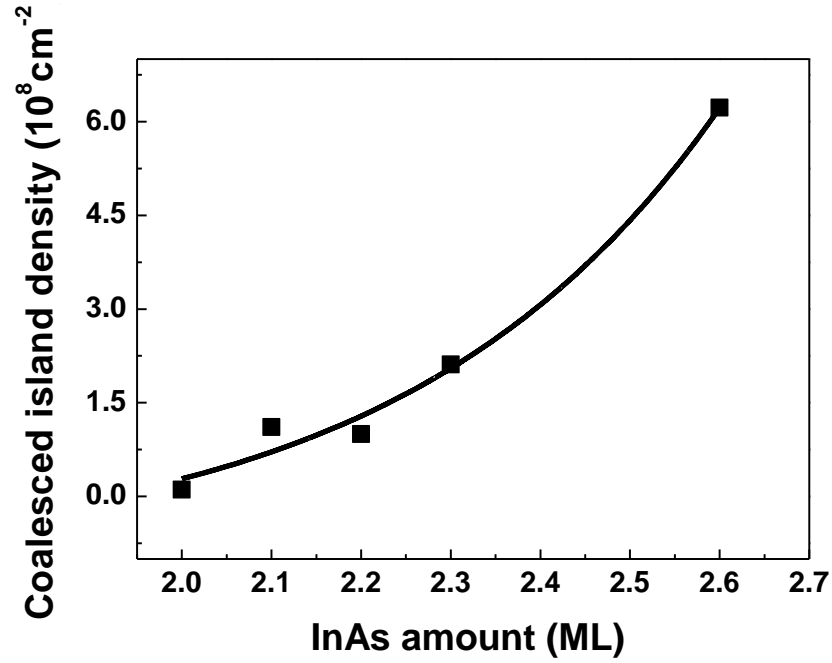
Fig. 6.22. Coalesced island density as a function of InAs coverage.

These irregular islands act as a strain-free sink for surface adatoms during growth and as the InAs coverage is increased the additional deposited material migrates away from normal coherent islands and accumulates in the large islands [6.47]. Though the research quoted above is for the optimisation of QDs for laser devices, it offers a critical value of the InAs coverage beyond which ripened coherent islands forms defects. Thus in our case, 2.2-2.3 ML is the optimum InAs coverage beyond which larger irregular islands forms, in addition to the stable ensemble of coherent islands.

The results of this section demonstrate that the DWELL structure described previously (grown at QD growth temperature of 470 ^{o}C and InAs coverage of 2.6 ML) was grown at sufficiently high QD InAs deposition, possibly explaining low output power at maximum 3dB bandwidth.

6.3.2.2 Electrical and Optical Comparison

Based on PL and AFM studies, growth temperature of 470 ^{o}C and InAs deposition amount of 2.2 ML (largest FWHM) was selected for studying the electrical characteristics of the SLED and to compare with the SLED grown at same temperature but with an InAs deposition amount of 2.6 ML presented earlier (Fig. 6.11). Again for the comparison of SLED performance, a 6 mm long device and 50 µm wide ridge widths were selected. All measurements are done in the pulsed regime (5us pulsed duration and 1% duty cycle) at a tile temperature of 300 K.

The power-current characteristics of the DWELL SLEDs are shown in Fig. 6.23. Superluminescent behaviour is evidenced for QD SLED grown using 2.2 ML of InAs SLED with increasing current density as compared to 2.6 ML InAs SLED. As compared to 2.6 ML SLED, the power of 2.2 ML device was higher by a factor 2 at 50 A/cm^2, a factor 10 at 250 A/cm^2 and a factor of ~ 24 at 333 A/cm^2. In the current density range of 250-330 A/cm^2, the slope efficiency of the 2.2 ML SLED was a factor of ~ 40 higher than the one at 2.6 ML device.

The QD areal density for both devices was roughly the same: ~8.5 X 10^{10} cm^{-2} (see Figs. 6.9 & 6.21). On the other hand, the coalesced island densities for 2.2 and 2.6 ML were ~1 X 10^8 cm^{-2} and ~7 X 10^8 cm^{-2}, respectively (see Figs. 6.10 &6. 22). As expected the QD density was the same for both the devices but a factor of ~7 increase in the coalesced island density for 2.6 ML devices as compared to 2.2 ML SLED. The increase in coalesced island density induces a higher non–radiative centre density, which contributes to the lower amplified spontaneous efficiency at low-current densities observed for the sample with 2.6 ML of InAs (see inset Fig. 6.23).
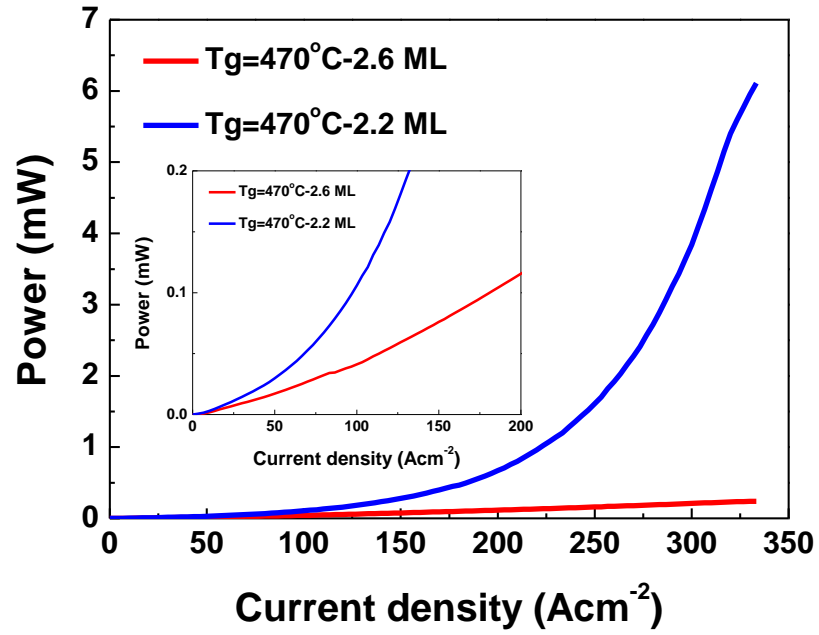
Fig. 6.23. Power-current characteristics of the DWELL SLEDs for different InAs deposition amount. Inset exploded view.
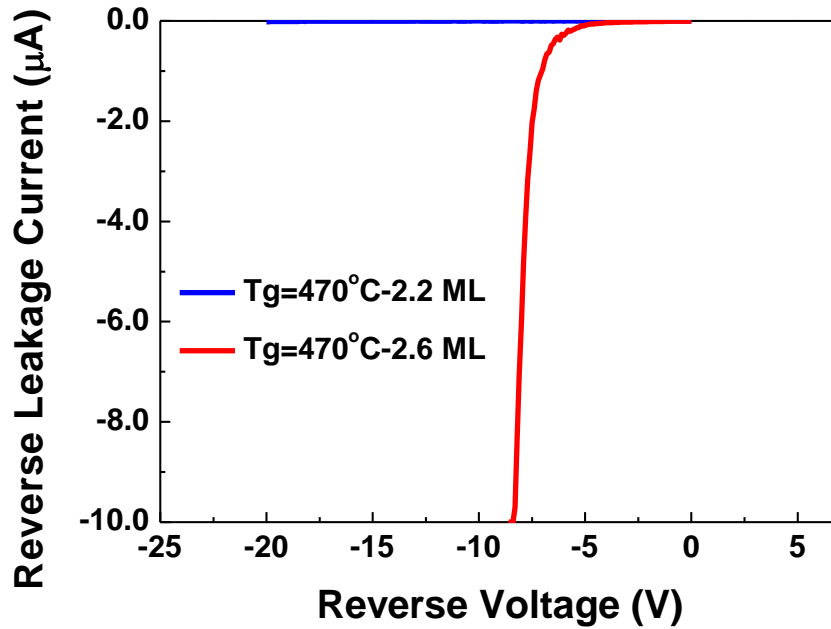

Fig. 6.24. Reverse leakage current as a function of the reverse bias voltage for constant QD growth temperature and InAs deposition of 2.2 and 2.6 ML.

These results clearly highlight the negative impact of the coalesced islands on the SLED performance.

In previous discussions, its been shown that defects with in the active medium result in a leakage current observed in the reverse I-V characteristics (see Fig. 6.16). Figure 6.24 shows the reverse leakage current for the 2 SLEDs discussed above. No breakdown voltage was noted for 2.2 ML InAs SLED; where as a soft breakdown is evident for 2.6 ML InAs SLED. The decrease in breakdown voltage is indicative of higher defect density, which is consistent with AFM and electrical characterisation results discussed above.

Figure 6.25, plots the electroluminescence spectra as a function of increasing current density for the 2.2 ML InAs SLED. The EL spectra has a broad spectrum in line with the PL emission of Fig. 6.14. The 3dB bandwidth, where the ground and excited state of QD balances is ~ 160 nm. As a comparison (see Figure 6.12 (d)) the 3dB bandwidth for 2.6 ML InAs deposited SLED was ~130 nm. As can be seen with a decrease in InAs amount from 2.6 to 2.2 ML, 3dB bandwidth increased by ~30 nm. Interestingly we have noted that for a range of current densities from 100- 170 A/cm^2 the spectral modulation range from 1-3dB (which is with in the range of the requirement for OCT to avoid ghost images) and the spectral bandwidth varies with in 160±5-155 ±5 nm. The power was ~0.4 mW (see Fig. 6.23) at 170 A/cm^2 which is a factor of ~4 more than the power for 2.6 ML InAs SLED. It is to be noted that higher power can be achieved with longer or tapered devices [6.11]. As expected from the PL and AFM measurements, the SLED output power and the bandwidth increase as the InAs amount is decreased.

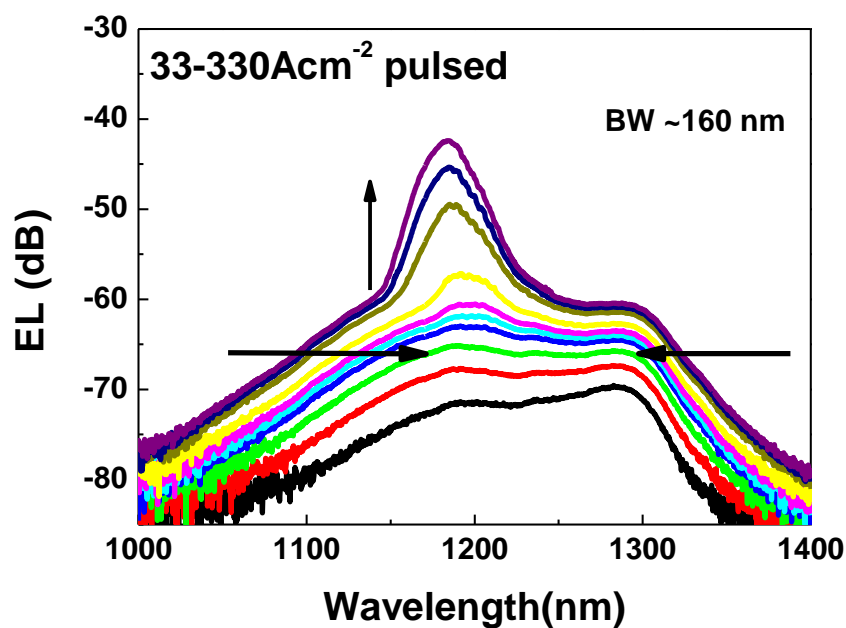**Fig. 6.25.** EL spectrum as a function of increasing current density (33-330 A/cm^2) for a 6 mm long and 50 µm wide SLED with 2.2 ML InAs coverage.
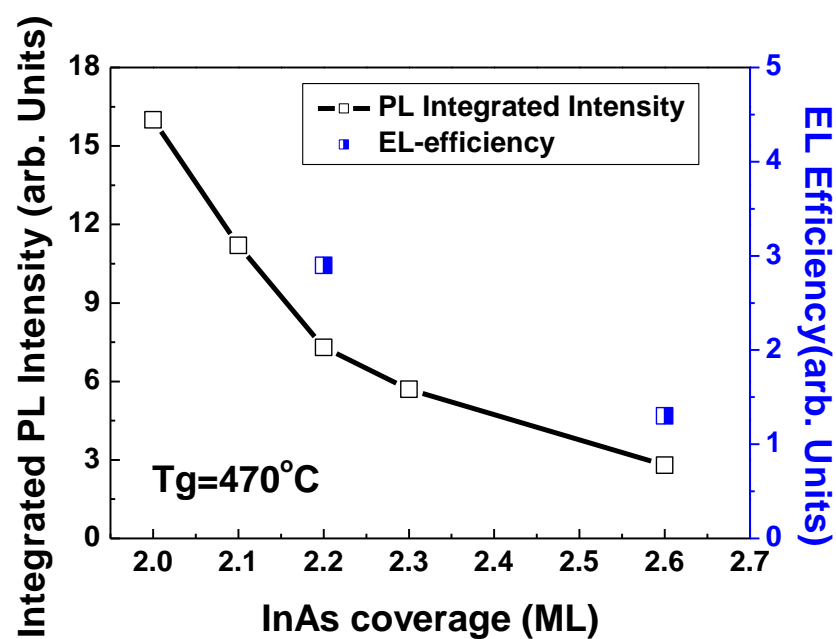

Fig. 6.26. Integrated PL intensity and EL efficiency plotted as a function of InAs coverage.

Figure 6.26, shows the integrated PL intensity and EL efficiency, as a function of InAs amount. For 2.2 ML InAs the integrated PL intensity and EL efficiency are around a factor 2 higher as compared to 2.6 ML sample. Significantly, the EL efficiency of the SLED has a good correlation with the integrated PL efficiency of the test structures.

In conclusion of last two sections: PL and EL efficiency are in good agreement, indicating that PL is a good tool for SLED characterisation. The dot density increase is in good agreement with the literature. Bimodal distribution of dots agrees with PL. Optimal InAs coverage of 2.2 ML and 470 ^{o}C to get high quality device with 160 nm 3dB bandwidth. Further optimisation from this point is possible by varying other parameters.

6.3.3 Effects of Deposition Rate and Low-Temperature (LT) GaAs Spacer Thickness

Previously, Liu *et al.* [6.48] have reported that growth temperature of the GaAs spacer layer has pronounced effect on both optical and structural properties of the InAs/ GaAs QDs. He observed dislocations in the second and subsequent layers of QDs, as a result of roughness in the underlying spacer layer, due to low temperature growth of the spacer layer, in his case 510 ^{o}C. However, as discussed earlier (growth section), Liu observed that by increasing the temperature to 580 ^{o}C for the final 35 mm (HGTSL) of the 50 nm GaAs spacer layer a much smoother surface is achieved, allowing the fabrication of essential identical and defect free QD layers [6.37]. The HGSTL demonstrated to eliminate surface roughness and hence suppress the formation of defects [6.37, 6.48]. In another study for 'laser

dots' Liu, have shown a significant improvement in device performance (reduced reverse leakage, increase spontaneous emission, reduced threshold current density and increase in external differential efficiency), when the LT GaAs spacer layer thickness is reduced from 15 to 2 nm [6.49]. Further work on Liu's method was carried on by Ray *et al.,* from our group, who also noted improved performance of laser and SLED by engineering the LT GaAs spacer layer thickness [6.21]. Ray noted a 4 fold increase in CW power for SLED at a given drive current when LT GaAs spacer layer thickness is reduced from 15 to 2 nm. In both studies improvement of device performance is attributed to selective elimination of very low density of dislocated dots and smaller number of defects in the thinner LT GaAs spacer layer. The only disadvantage for this QD growth process is the blue-shift (~40 nm) of peak emission wavelength (for 2nm LT GaAs spacer) due to the out diffusion of indium ('indium flushing' - a reduction in the amount of indium in the dots) from the QDs.

Another parameter of interest is the deposition rate or growth rate. Previously researcher have shown that high growth rate results in short emission wavelength and inferior optical properties despite a high QD density [6.50]; a low growth rate results in a long emission wavelength but a low QD density, and thereby a low gain [6.38, 6.39, 6.51].

In this section, the optimised parameters discussed in previous section in terms of InAs deposition rate, deposition amount and low-temperature (LT) GaAs spacer layer thickness are explored further. Particularly the InAs deposition rate is varied from 0.1M L/s to 0.2 ML/s, and the LT GaAs spacer thickness from 5 nm to 2.5 nm, further more opto-electronic characteristics of SLED is explored by reducing the

InAs deposition from 2.2 to 2.0 ML. Table 6.4, shows the samples used for optical

and electrical characterisations.

Sample	Growth temperature (^{o}C)	InAs amount (ML)	Growth rate (ML/sec)	LT GaAs (nm)
Vn1778	470	2.0	0.1	5
Vn1779	470	2.2	0.1	2.5
Vn1781	470	2.2	0.2	5
Vn1698	470	2.2	0.1	5

Table. 6.4. Samples for optical and electrical characterisation.

6.3.3.1   Comparison of Optical and Electrical Characteristics

Figure 6.27, shows the room temperature normalised PL for different InAs

coverage, deposition rate and LT GaAs spacer layer thickness.

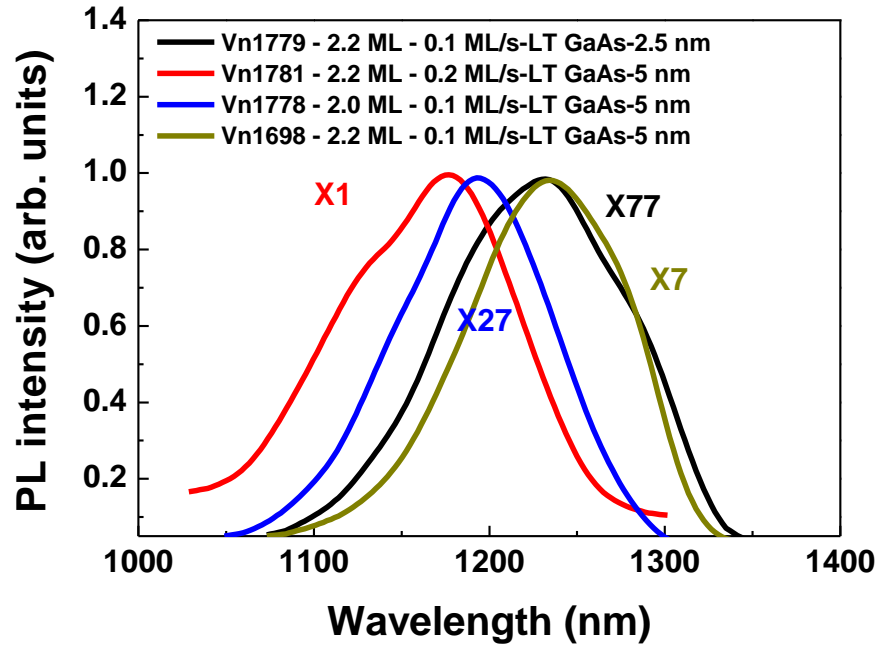**Fig. 6.27.** Room temperature PL obtained from InAs/GaAs QD grown at 470 °C for different InAs coverage, deposition rate and LT GaAs spacer layer thickness.

The figure clearly shows that the PL intensity decreases by a factor of ~ 7 and the

peak emission wavelength decreases from to 1235 to 1180 nm as the growth rate

increased is from 0.1 to 0.2 ML/s for previously optimized sample (Vn1698). An

increase in FWHM from 115 to 125 nm is also noted and is attributed to increased

QD inhomogeneity [6.52]. The decrease in PL intensity is attributed to an increase

in non-radiative centres probably due to increased coalesced islands density

despite an expected increase in dot density [6.52].

The redshift of the emission wavelength for 0.1 ML/s as compared to 0.2 ML/s, is

attributed to the increases in size or indium content in QDs [6.28]. The second

significant result is the increase in PL intensity by a factor of ~ 27 for 2.0 ML InAs

deposition and 0.1 ML/s deposition rate, as compared to 2.2 ML InAs deposition

and 0.2 ML/s deposition rate. The third significant result is the increase in PL

intensity by a factor of ~ 11 as the LT GaAs spacer layer thickness is reduced from 5

nm to 2.5 nm, for 2.2 ML QD InAs deposition amount, 0.1 ML/s growth rate and at

470 ^{o}C QD growth temperature. This is attributed to the defect healing of the large

dislocated dots (coalesced island) [6.21, 6.49]. Also, the peak emission wavelength

is not affected significantly by reducing the LT GaAs spacer layer thickness, which is

in contrast to a ~40 nm blueshift observed by Liu and Ray. The blueshift in

emission is attributed to out of diffusion of indium in the dots and small QD height

(noted from TEM) for 2 nm sample [6.21, 6.49]. In their study LT GaAs spacer

layers thickness was decreased from 15 to 2 nm, where as for my study it

decreased from 5 to 2.5 nm, which means the defective density in my case was

already healed for 5 nm LT GaAs spacer layer thickness and a very small big

coalesced islands are healed selectively when thickness reduced to 2.5 nm with out

disturbing the over all dot distribution (and hence no blueshift in peak emission).

These results are significant for 'laser dots', for optical telecoms applications where

peak emission wavelength is most important.

Last but not the least, is the increase of PL intensity by a factor of ~77 for 2.5 nm

LT GaAs sample (Vn1779) as compared to 0.2 ML/s growth rate sample (Vn1781).

These results clearly demonstrate that our choice of QD growth rate of 0.1 ML/s,
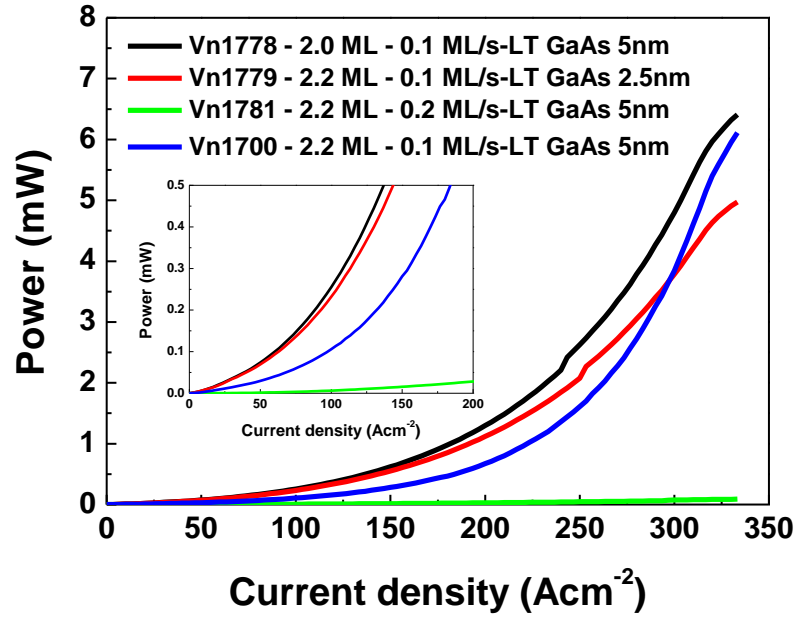
discussed in earlier section was optimum.

Fig. 6.28. Power-current characteristics of the DWELL SLED for different InAs coverage, deposition rate and LT GaAs spacer layer thickness. Inset exploded view.

Power-current characteristics of the DWELL SLEDs at different InAs coverage,

deposition rate and LT GaAs spacer layer thickness is shown in Fig. 6.28. Super

luminescence behaviour (i.e. super linear increase in power with increasing current

density) is evidenced for all the samples except for the QDs grown at growth rate of

0.2 ML/s. These results are in good agreement with the PL data discussed in

previous sections. The SE (inset Fig. 6.28) for sample grown with deposition amount

of 2.0 ML, 5 nm LT GaAs spacer layer thickness (Vn1778) is similar to the sample

grown with deposition amount of 2.2 ML, 2.5 nm LT GaAs spacer layer thickness

(Vn1779). And these two samples are a factor of ~2 better in power than the Vn1700 sample (2.2 ML InAs coverage, growth rate of 0.1 ML/s and 5 nm LT GaAs spacer layer thickness). These results suggests that the defect density (~10^8/cm^2) of the previous optimised sample (Vn1700) with 2.2 ML InAs coverage and 5 nm LT GaAs spacer layer thickness is partially cured by decreasing the LT GaAs spacer layer thickness [6.21, 6.49], bringing it close to low-defect (see Fig. 6.22) 2.0 ML InAs coverage sample.

It is also noted that to obtain the same output power for the previously optimised device (Vn1700) as compared to 2.0 ML InAs (Vn1778) or the device with 2.5 nm LT- GaAs (Vn1779), an additional current density of 50 A/cm^2 is required, which is significant when the device is operated in the continuous mode, where the rollover with self heating becomes prominent. The sample with a growth rate of 0.2 ML/s will not be considered further due to low output power.

Figure 6.29, shows the electroluminescence spectra as a function of increasing current density for sample with 2.0 ML InAs coverage, 5 nm LT GaAs spacer layer thickness and the sample with 2.2 ML InAs coverage, 2.5 nm LT GaAs spacer layer thickness. It is evident from Fig. 6.29(a) & (b) that the maximum bandwidth was ~ 90 nm for sample with 2.0 ML InAs coverage and ~ 155 nm for sample with 2.5 nm LT GaAs spacer layer thickness.

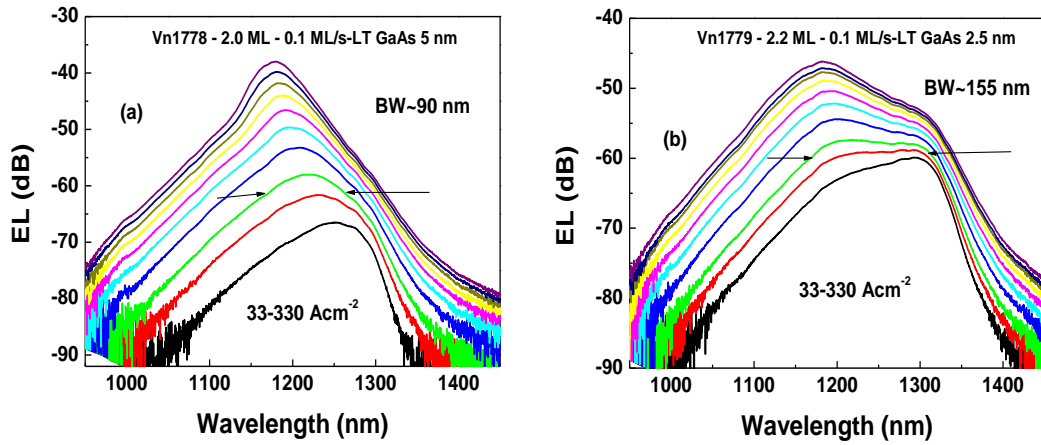**Fig. 6 29.** EL spectrum as a function of increasing current density (33-330 A/cm^2) for a 6 mm long and 50 µm wide SLED (a) InAs coverage 2.0 ML and LT GaAs spacer layer thickness 5 nm (b) InAs coverage 2.2 ML and LT GaAs spacer layer thickness 2.5 nm, grown at growth rate of 0.1 ML/s

These results are consistent with the PL linewidth of Fig. 6.19. For sample with LT GaAs spacer layer thickness of 2.5 nm, we noted less than 3dB spectral modulation and the spectral bandwidth varies with in 155 ± 5 to 150 ± 5 nm for a range of current densities from 100-170 A/cm^2. Interestingly the maximum bandwidth was approximately same for the previously optimised sample with 2.2 ML InAs coverage and 5 nm LT GaAs spacer layer thickness (see Fig. 6.25). Hence, reducing the LT GaAs spacer layer from 5 nm to 2.5 nm increased the output optical power by a factor of ~2 (100-170 A/cm^2), preserved the peak emission wavelength and bandwidth. These results suggest that LT GaAs spacer layer thickness along with HGSTL growth step is crucial in suppressing the defect formation.

6.4 Conclusions

In this chapter a systematic study of the key MBE parameters affecting 1200-1300nm quantum DWELL structures with a view to optimisation for broadband

_____

applications. It has been reported that for broadband applications the QD growth temperature, InAs deposition thickness, deposition rate and LT GaAs spacer layer thickness are crucial. We have shown the effect of reducing QD growth temperature is to increase the QD areal density and size inhomogeneity. However, as the QD density increases, coalescence of the QDs is observed by AFM studies and is expected to results in additional non-radiative defects, evidenced by a strong reduction in PL efficiency. Finally I have described that in order to benefit from the broad size distribution and high density of low temperature growth the amount of InAs deposited to form the QDs has to be reduced. A maximum 3dB bandwidth of ~160±5 nm and output power ~0.2 mW is obtained from broad area (6mm long and 50 um wide) superluminescent diode fabricated from a sample grown with deposition temperature of 470 $^{\circ}$C, InAs deposition amount of 2.2 ML , low temperature GaAs spacer layer thickness of 5 nm and growth rate of 0.1 ML/s. A further optimisation of the SLED device by reduction of the LT GaAs spacer layer thickness from 5 nm to 2.5 nm (defect healing) improved the output power by a factor of ~2, with no significant change in peak emission wavelength, but with ~5 nm reduction in bandwidth.

6.5   Future Work

It would be interesting to compare the results obtained in this study with a TEM study of the samples, which may present a visual display of defect densities, and height variation of normal and coalesced dot especially for the case of 5 nm and 2.5 nm LT GaAs spacer layer sample.

It would be interesting to fabricate a single mode fibre device (3 μm wide and 10 mm long) with the optimised sample and measure the resolution of skin images by OCT and demonstrate enhanced image quality.

It would also be very interesting to fabricate the multi-section device, where independently control of power and spectral bandwidth relative to the ground state (GS) and the excited state (ES) of the QD is possible. This method may provide 3 dB bandwidth of more than 200 nm with a practical output power for OCT.

It would be interesting to fabricate the 5 nm and 2.5 nm (as no blueshift observed) samples with laser dots and measure and compare the length dependent parameters, for optical communication applications.

Lastly it would be very interesting to grow the bilayer seed layer (high density) by decreasing the InAs deposition from 2.4 ML (chapter 3) to 2.0 ML at a deposition rate of 0.1 ML/s. One would expect a density increase from 3 to $\sim 8 \times 10^{10} cm^{-2}$, which would enhance the gain and modulation speed of the bilayer devices.

References

[6.1] A. Unterhuber, B. Povazay, A. Aguirre, Y. Chen, F. X. Kärtner, J. G.Fujimoto, and W. Drexler, "Broad Bandwidth Laser and Nonlinear Optical Light Sources for OCT," *in Optical Coherence Tomography*, Springer Berlin Heidelberg, pp. 301-358, 2008.

[6.2] W. Drexler and J. G. Fujimoto, "State-of-the-art retinal optical coherence tomography," *Progr. Retin. Eye Res.*, vol. 27, no. 1, pp. 45–88, 2008.

[6.3] J. Welzel, E. Lankenau, G. Huttmann, and R. Birngruber, "OCT in dermatology," *in Optical Coherence Tomography,* Springer Berlin Heidelberg, pp. 1103–1122, 2008.

[6.4] W. Drexler, "Ultrahigh-resolution optical coherence tomography," *J. Biomed. Opt.*, vol. 9, no. 1, pp. 47-74, 2004.

[6.5] R. K. Wang, "Signal degradation by coherence tomography multiple scattering in optical of dense tissue: A Monte Carlo study towards optical clearing of biotissues," *Phys. Med. Biol.*, vol. 47, no.13, pp. 2281–2299, 2002.

[6.6] D. Koozekanani , K. L. Boyer , and C. Roberts, "Tracking the optic nerve head in OCT video using dual eigen spaces and an adaptive vascular distribution model," *IEEE Trans. on Med. Imag.*, vol. 22, no. 12, pp. 1519-1536, 2003.

[6.7] G. Zuccaro, N. Gladkova , J. Vargo, F. Feldchtein, E. Zagaynova, D. Conwell, G. Falk, J. Goldblum, J. Dumot, J. Ponsky, G. Gelikonov, B. Davros, E. Donchenko, and J. Richter, "Optical coherence tomography of the esophagus and proximal stomach in health and disease," *American Journal of Gastroenterology*, vol. 96, no. 9, pp. 2633-2639, 2001.

[6.8] S. H. Yun and B. E. Bouma, "Wavelength swept lasers," *in Optical Coherence Tomography*. Springer Berlin Heidelberg, pp. 359–377, 2008.

[6.9] L. Vabre, A. Dubois, and A. C. Boccara, "Thermal-light full-field optical coherence tomography," *Opt. Lett.*, vol. 27, no. 7, pp. 530–532, 2002.

[6.10] V. R. Shidlovski, "Superluminescent diode light sources for OCT," *in Optical Coherence Tomography.*, Springer Berlin Heidelberg, pp. 281–299, 2008.

[6.11] Z.Y. Zhang, R.A. Hogg, X.Q. Lv, and Z.G. Wang, "Self-assembled quantum dot superluminescent light emitting diodes," *Adv. Opt. Photon.*, vol. 2, no. 2, pp. 201-228, 2010.

[6.12] M. C. Amann and J. Boeck, "High efficiency superluminescent diodes for optical-fibre transmission," *Electron. Lett.*, vol. 15, no. 2, pp. 41–42 1979.

[6.13] G. A. Alphonse, D. B. Gilbert, M. G. Harvey, and M. Ettenberg, "High power superluminescent diodes," *IEEE J. Quant. Electron.*, vol. 24, no. 12, pp. 2454–2457, 1988.

[6.14] T. H. Ko, D. C. Adler, J. G. Fujimoto, D. Mamedov, V. Prokhorov, V. Shidlovski, and S. Yakubovich, "Ultrahigh resolution optical coherence tomography imaging with a broadband superluminescent diode light source," *Optics Express*, vol. 12, no. 10, pp. 2112-2119, 2004.

[6.15] S. D. McDougal, O. P.Kowalski, J. H. Marsh, and J. S. Aitchison, "Broad optical bandwidth InGaAs-InAlGaAs light-emitting diodes fabricated using a laser annealing process," *IEEE Photon. Technol. Lett.*, vol. 11, no. 12, p. 1557, 1999.

[6.16] T. K. Ong, M. Yin, Z. Yu, Y. C. Chan, and Y. L. Lam, "High performance quantum well intermixed superluminescent diodes," *Measurement Science & Technology*, vol. 15, no. 8, pp. 1591-1595, 2004.

[6.17] G. T. Du, C. D. Xu, Y. Liu, Y. S. Zhao, and H. S. Wang, "High-power integrated superluminescent light source," *IEEE J. of Quant. Electron.*, vol. 39, no. 1, pp. 149-153, 2003.

[6.18] C. F. Lin, B. L. Lee, and P. C. Lin, "Broad-band superluminescent diodes fabricated on a substrate with asymmetric dual quantum wells," *IEEE Photon. Technol. Lett.*, vol. 8, no. 11, pp. 1456-1458, 1996.

[6.19] H. S. Gingrich, D. R. Chumney, S. Z. Sun, S. D. Hersee, L. F. Lester, and S. R. J.Brueck, "Broadly tunable external cavity laser diodes with staggered thickness multiple quantum wells," *IEEE Photon. Tech. Lett.*, vol. 9, no. 2, pp. 155-157, 1997.

[6.20] L. H. Li, M. Rossetti, A. Fiore, L. Occhi, and C. Velez, "Wide emission spectrum from superluminescent diodes with chirped quantum dot multilayers," *Electron. Lett.*, vol. 41, no. 1, pp. 41–43, 2005.

[6.21] S. K. Ray, T. L. Choi, K. M. Groom, H. Y. Liu, M. Hopkinson, and R. A. Hogg, "High-power 1.3-µm quantum-dot superluminescent light emitting diode grown by molecular beam epitaxy," *IEEE Photon. Technol. Lett.*, vol. 19, no. 2, pp. 109–111, 2007.

[6.22] S. K. Ray, T. L. Choi, K. M. Groom, B. Stevens, H. Liu, M. Hopkinson, and R. A. Hogg, "High-power and broad-band quantum dot superluminescent diodes

centred at 1250 nm for optical coherence tomography," *IEEE J. Sel. Topic Quantum Electron.*, vol. 13, no. 5, pp. 1267–1272, 2007.

[6.23] L. H. Li, M. Rossetti, and A. Fiore, "Chirped multiple InAs quantum dot structure for wide spectrum device applications," *J. Crystal Growth*, vol. 278, pp. 680–684, 2005.

[6.24] P. D. L. Judson, K. M. Groom, D. T. D. Childs, M. Hopkinson, and R. A. Hogg, "Multi-section quantum dot superluminescent diodes for spectral shape engineering," *IET Optoelectron.*, vol. 3, no. 2, pp. 100–104, 2009.

[6.25] S. K. Ray, K. M. Groom, H. Y. Liu, M. Hopkinson, and R. A. Hogg, "Broad-band superluminescent light emitting diodes incorporating quantum dots in compositionally modulated quantum wells," *Jpn. J. Appl. Phys.*, vol. 45, pp. 2542–2545, 2006.

[6.26] A. R. Kovsh, A. E. Zhukov, D. A. livshits , A. Yu Egorov, V. M. Ustinov, M. V. Maximov, Yu. G. Musikhin, N.N. Ledentsov, P. S. Kop'ev. Zh .I. Alferov, D. Bimberg, "3.5 W CW operation of quantum dot laser," *Electron. Lett.*, vol. 35, no. 14, pp. 1161-1163, 1999.

[6.27] H. Y. Liu, M. Hopkinson, C. N. Harrison, M. J. Steer, R. Firth, I. R. Seller, D. J. Mowbray and M. S. Skolnick, "Optimizing the growth of 1.3 μm InAs/InGaAs dots-in-a-well structure," *J. Appl. Phys.*, vol. 93, no. 5, p. 2931-2936, 2003.

[6.28] P. B. Joyce, T. J. Krzyzewski, G. R. Bell, T. S. Jones, E. C. Le Ru, and R. Murray, "Optimizing the growth of 1.3 μm InAs/GaAs quantum dots," *Phys. Rev. B.*, vol. 64, no. 23, p. 235317, 2001.

[6.29] Q. Xie, A. Madhukar, P. Chen, and N.P. Kobayashi, "Vertically self organised InAs quantum box islands on GaAs (100)," *Phys. Rev. Lett.*, vol. 75, no. 13, pp. 2542-2545, 1995.

[6.30] K. Mukai, Y. Nakata, H. Shoji, M. Sugawara, K. Ohtsubo, N. Yokoyama, and H. Ishikawa, "Lasing with low threshold current and high output power from columnar-shaped InAs/GaAs quantum dots," *Electron. Lett.*, vol. 34, no.16, pp. 1588-1590, 1998.

[6.31] O. B. Shchekin and D. G. Deppe, "1.3 μm InAs quantum dot laser with T_o =161 K from 0 to 80 °C," *Appl. Phys. Lett.*, vol. 80, no. 18, pp. 3277–3279, 2002.

[6.32] X. Huang, A. Stintz, C. P. Hains, G. T. Liu, J. Cheng, and K. J. Malloy, "Very low threshold current density room temperature continuous-wave lasing from a single-layer InAs quantum-dot laser," *IEEE Photon. Technol. Lett.*, vol. 12, no. 3, pp. 227–229, 2000.

[6.33] K. Otsubo, N. Hatori, M. Ishida, S. Okumura, T. Akiyama, Y. Nakata, H. Ebe, M. Sugawara, and Y. Arakawa, "Temperature-insensitive eye-opening under 10-Gb/ s modulation of 1.3-μm p-doped quantum-dot lasers without current adjustments," *Jpn. J. Appl. Phys.*, vol. 43, pp. L1124–L1126, 2004.

[6.34] Y. Ebiko, S. Muto, D. Suzuki, S. Itoh, K. Shiramine, T. Haga, Y. Nakata, and N. Yokoyama, "Island size scaling in InAs/GaAs self-assembled quantum dots," *Phys. Rev. Lett.*, vol. 80, no. 12, pp. 2650–2653, 1998.

[6.35] P. D. L. Greenwood , D. T. D. Childs , K. M. Groom , B. J. Stevens , M. Hopkinson and R. A. Hogg "Tuning superluminescent diode characteristics for

optical coherence tomography systems by utilising a multi-contact device incorporating wavelength modulated quantum dots," *IEEE J. Sel. Topics Quantum Electron.*, vol. 15, no. 3, pp. 757-763 , 2009.

[6.36] P. D. L. Greenwood , D. T. D. Childs , K. Kennedy , K. M. Groom , M. Hugues , M. Hopkinson , R. A. Hogg , N. Krstaji , L. E. Smith , S. J. Matcher , M. Bonesi , S. MacNeil and R. Smallwood   "Quantum dot superluminescent diodes for optical coherence tomography: Characterization," *IEEE J. Sel. Topics Quantum Electron.*, vol. 16, no. 4 , pp.1015-1022, 2010.

[6.37] H. Y. Liu, I. R. Sellers, T. J. Badcock, D. J. Mowbray, M. S. Skolnick, K. M. Groom, M. Gutierrez, M. Hopkinson, J.S. Ng, J. P. R. David, and R. Beanland, "Improved performance of 1.3 µm multilayer InAs/GaAs quantum-dot lasers using a high-growth-temperature GaAs spacer layer," *Appl. Phys. Lett.,* vol. 85, no. 5, pp. 704–706, 2004.

[6.38] E. Clarke, P. Howe, M. Taylor, P. Spencer, E. Harbord, R. Murray, S. Kahkhodazadeh, D. W. McComb, B. J. Stevens, and R. A. Hogg, "Persistent template effect in InAs/GaAs quantum dot bilayers", *J. Appl. Phys.*, vol. 107, no. 11, pp. 113502-113502-6, 2010.

[6.39] E. C. Le Ru,   P. Howe, T. S. Jones, and Murray, R.: "Strain-engineered InAs/GaAs quantum dots for long-wavelength emission, " *Phys. Rev. B,* vol. 67, no. 16, pp. 165303-165307, 2003.

[6.40] A. Madhukar, Q. Xie, P. Chen, and A. Konkar, "Nature of strained InAs three-dimensional island formation and distribution on GaAs (100)," *Appl. Phys. Lett.*, vol. 64, no. 20, pp. 2727-2729, 1994.

[6.41] J. Tersoff, "Enhanced Nucleation and Enrichment of Strained-Alloy Quantum Dots," *Phys. Rev. Lett.*, vol. 81, no. 15, p. 3183, 1998.

[6.42] G. S. Solomon, J. A. Trezza, and J. S. Harris, Jr., "Substrate temperature and monolayer coverage effects on epitaxial ordering of InAs and InGaAs islands on GaAs," *Appl. Phys. Lett.,* vol. 66, no.8 pp. 991-993, 1995.

[6.43] M. O. Lipinski, H. Schuler, O. G. Schmidt, K. Eberl, and N. Y. Jin-Phillipp, "Strain-induced material intermixing of InAs quantum dots in GaAs" *Appl. Phys. Lett.*, vol. 77, no. 12, pp. 1789-1791, 2000.

[6.44] P. Frigeri, L. Nasi, M. Prezioso, L. Seravalli, G. Trevisi, E. Gombia, R.Mosca, F. Germini, C. Bocchi, and S. Franchi, "Effects of the quantum dot ripening in high-coverage InAs/GaAs nanostructures," *J. Appl. Phys.*, vol. 102, no. 8, pp.083506-083506-8, 2007.

[6.45] J. S. Wang, J. F. Chen, J. L. Huang, P. Y. Wang, and X. J. Guo, "Carrier distribution and relaxation-induced defects of InAs/GaAs quantum dots, " *Appl. Phys. Lett.*, Vol. 77, no. 19, pp.3027-3039, 2000.

[6.46] S. W. Lin, C. Balocco, M. Missou, A. R. Peaker, and M. Song, "Coexistence of deep levels with optically active InAs quantum dots,"*Phys. Rev.B*, vol. 72, no. 16, pp. 165302-165308, 2005.

[6.47] D. Leonard, K. Pond, and P. M. Petroff, "Critical layer thickness for self-assembled InAs islands on GaAs," *Phys. Rev. B,* vol. 50, no. 16, pp.11687-11692, 1994.

[6.48] H. Y. Liu, I. R. Sellers, M. Gutierrez, K. M. Groom, W. M. Soong, M. Hopkinson, J. P. R. David, R. Beanland, T. J. Badcock, D. J. Mowbray, M. S. Skolnick, , "Influences of the spacer layer growth temperature on multilayer InAs/GaAs quantum dot structures," *J. Appl. Phys.* , vol. 96, no.4, pp.1988-1992, 2004.

[6.49] H. Y. Liu, S. L. Liew, T. Badcock, D. J. Mowbray,M. S. Skolnick, S. K. Ray, K. M. Groom, F. Hasbullah, C. Y. Jin, M. Hopkinson, and R. A. Hogg, "P-doped 1.3 μm InAs/GaAs quantum-dot laser with low room temperature threshold current density and high different efficiency*," Appl. Phys. Lett*., vol. 89, no. 7, pp. 07113-07113-3, 2006.

[6.50] I. Mukhametzhanov, R. Heitz, J. Zeng, P. Chen, and A. Madhukar, "Independent manipulation of density and size of stress-driven self-assembled quantum dots," *Appl. Phys. Lett.,* vol. 73, no. 13, pp. 1841-1843, 1998.

[6.51] B. Alloing, C. Zinoni, V. Zwiller, L. H. Li, C. Monat, M. Gobet, G. Buchs, A. Fiore, E. Pelucchi, E. Kapon, "Growth and characterization of single quantum dots emitting at 1300 nm," *Appl. Phys. Lett*., vol. 86, no. 10, pp. 101908-101908-3, 2005.

[6.52] H. T. Dobbs, D. D. Vvedensky, and A. Zangwill, "Mean-Field Theory of Quantum Dot Formation," *Phys. Rev. Lett*., vol. 79, pp. 897-900, no. 5, 1997.

Chapter 7

Conclusions and Future Work

In this thesis I have presented and discussed results concerned with InAs/GaAs quantum dot bilayer lasers and DWELL superluminescent light emitters.

In chapter 3, I have shown a method of extending the emission wavelength of QDs on GaAs by using a bilayer growth technique. The GaAs capped bilayer laser demonstrates twice the modal gain for ground and excited states as compared to an InGaAs capped 'single' layer QD laser operating at similar wavelength (~1350 nm).

In fourth chapter I presented further optimisation of bilayer and have shown room temperature emission wavelength of the QDs, up to 1400 nm for GaAs capped QDs and up to 1515 nm when an InGaAs cap is applied to the upper QD layer, with extremely low inhomogeneous broadening. Further I have shown that when these QDs are incorporated into laser structures, ground state lasing up to 1420 nm is achieved and ground state electroluminescence (EL) at 1515 nm with a narrow EL linewidth of 23 meV. The EL emission at 1515 nm, is the first time ever achieved without using metamorphic buffer layers. Further analysis of gain and absorption on multi-section devices under high bias conditions have shown, the peaks in the gain spectra are asymmetrically broadened towards longer wavelengths, such that net positive modal gain beyond 1500 nm can be achieved.

It would be interesting to apply high reflection coating to laser device to see if it can lase 1515 nm. Also it would be interesting to study the gain, absorption, lasing

_____

mode packet width and modulation dynamics of p-doped GaAs- and InGaAs capped bilayers.

In fifth chapter I have presented a method of using excited state QD lasers spanning the O-band via GaAs and InGaAs capped bilayer structures. Room temperature lasing from either the GS or ES is observed, depending on cavity length, for a range of wavelengths of 1340-1420 nm for the GS or 1260-1330 nm for the ES. By a two state simple model the affect of scattering time, carrier transport time and peak gain on k-factor limited modulation bandwidth is demonstrated.

It would be interesting to fabricate p-doped and un-doped GaAs- and InGaAs capped bilayer into ridge laser with coplanar contacts and compare the k-factor limited bandwidth of the GS and ES. Also it would be interesting to study the carrier transport effects of these devices.

In the last chapter I presented systematic study of the key MBE parameters affecting 1200-DWELL structures with a view to optimisation for broadband applications I have shown a maximum 3 dB bandwidth of ~160±5 nm and output power ~0.2 mW for broad area (6 mm long and 50 µm wide) superluminescent diode fabricated from a sample grown with deposition temperature of 470 ^{o}C, InAs deposition amount of 2.2 ML, low temperature GaAs spacer layer thickness of 5 nm and growth rate of 0.1 ML/s. A further optimisation of the SLED device by reduction of the LT GaAs spacer layer thickness from 5 nm to 2.5 nm (defect healing) improved the output power by a factor of ~2, with no significant change in peak emission wavelength, but with ~5 nm reduction in bandwidth.

_____

It would be interesting to fabricate the multi-section devices, where the independent control of power and spectral bandwidth may provide more than 200 nm of spectral bandwidth. Also, it would be interesting to apply this optimization study to bilayer laser epitaxy, which may provide the dot densities in the range of 8-10 X 10^{10} cm^{-2}.